CASCADED MULTILEVEL INVERTER AND ITS FACTS APPLICATIONS

By

Yang Liu

A DISSERTATION

Submitted to
Michigan State University
in partial fulfillment of the requirements
for the degree of

Electrical Engineering—Doctor of Philosophy

2016

ABSTRACT

CASCADED MULTILEVEL INVERTER AND ITS FACTS APPLICATIONS

By

Yang Liu

The conventional unified power flow controller (UPFC) that consists of two back-to-back multipulse inverters requires bulky and complicated zigzag transformers for isolation and reaching high voltage/high power. However, the zigzag transformers are usually very expensive, lossy, bulky and prone to failure. Moreover, they are slow (up to minutes to steady state after energizing) in dynamic response due to magnetizing current, and are thus not suited for fast-changing power flow control of intermittent and sporadic wind and solar power application.

A completely transformer-less UPFC based on an innovative configuration of two cascaded multilevel inverters (CMIs) has been recently invented. The unique configuration and control of the two CMIs as a power flow controller make it possible to independently control active and reactive power over a transmission line. The new UPFC represents a technological breakthrough and offers several enabling advantages that the traditional technology cannot provide, such as being completely transformer-less, light weight, high efficiency, high reliability, low cost, and possessing a fast dynamic response.

This dissertation reveals detailed modeling, control and analysis of the innovative structure of transformer-less UPFC: 1) UPFC power flow control, such as voltage regulation, line impedance compensation, phase shifting or simultaneous control of voltage, impedance, and phase angle, thus achieving independently control both the active and reactive power flow in the line; 2) dc capacitor voltage balance control for H-bridges of both series and shunt CMIs; 3) modulation of the CMI for low total harmonic distortion (THD) of output voltage and low

switching loss; 4) fast system dynamic response. The UPFC functionality with proposed control method is verified at 4,160 V.

Furthermore, applications of transformer-less UPFC to solve real-world problems are analyzed and experimental verified based on 13.8-kV/ 2-MVA setup. One demonstration is to use transformer-less UPFC for interconnecting two synchronous grids with large phase difference. The proposed transformer-less UPFC can realize grid interconnection control, independent active and reactive power control, dc-link voltage balance control, etc. Furthermore, 1-pu equipment can effectively compensate system with phase difference as large as 30°. Another example is to install the transformer-less UPFC into a congested grid to release the transmission grid congestion. The transformer-less UPFC is able to control bidirectional power flow and make parallel operation possible for two different feeders. Both detailed theoretical analysis and functionality test with proposed control strategy are addressed in the dissertation.

The innovative transformer-less UPFC has enormous technological and economic impacts on controlling the routing of energy over the existing power grid. The enabling technology of modularity, scalability makes it easy installation anywhere in the existing grid. Furthermore, the transformer-less UPFC helps maximize/ optimize energy transmission over the existing grids to minimize the need for new transmission lines. As a result, this will increase the transfer capability of the grid, combined with the controllability and speed of operation of the devices, thus will enable increased penetration of renewables and demand response programs. Finally, it will reduce transmission congestion and increase dynamic rating of transmission assets.

Dedicated to my Father and Mother:
Yongshan Liu and Nan Yang

ACKNOWLEDGEMENTS

First of all, I would like to give my heartfelt thanks to my dear advisor, Dr. Fang Z. Peng. Thank you very much for having me as one of your students. I really appreciate everything that you have done for me, your clear directions, your precious advice, and all your patient help during the past years. I would not be able to achieve what I become today and finish this work without you. I am so grateful and honorable of being your student.

Meanwhile, I am also very thankful to my committee members, Dr. Bingsen Wang, Dr. Joydeep Mitra, and Dr. Guoming Zhu. Thank you for giving me all the impressive lectures from which I built up my knowledge base and insightful suggestions for my dissertation.

Many thanks go to my colleagues in PEMD lab and my dear friends, for valuable discussions, suggestions and selfless help, as well as priceless friendship. Special thanks go to Dr. Shuitao Yang for teaching me so many things during the cooperation on UPFC project and treating me like a family member in daily life. The way you build hardware, innovative thinking of solving problems and research attitude has great influence on me. Many thanks go to Dr. Xi Lu, Dr. Niannian Cai, Dr. Yantao Song, Dr. Baoming Ge, Dr. Shuai Jiang, Dr. Shao (Sam) Zhang, Dr. Maosong Zhang, Dr. Dong Cao, Dr. Qin Lei, Dr. Wei Qian, Mr. Xianhao Yu, Mr. Sisheng Liang, Mr. Xiaorui Wang, Mr. Hulong Zeng, Mr. Runruo Chen, Mr. Yaodong Yu, Ms. Yunting Liu, Mr. Deepak Gunasekaran, Mr. Ujjwal Karki, Mr. Nomar Santini, Mr. Allan Taylor, and many of those I did not list here. All of you are great treasures for my whole life.

Thanks to Manqi Li, thank you for being with me and your love means everything to me.

Finally, thanks from my deep heart go to my parents. Thank you for raising me up and providing me everything. The love that I got from you is beyond expression.

TABLE OF CONTENTS

LIST OF TABLES

LIST OF FIGURES

CHAPTER 1 Introduction

1.1. Background

The mesh ac grid network presents more benefits than the radial system because of its higher reliability, especially under contingency conditions. However, due to lack of control devices (hardware limitation), the complicated meshed ac network has to be over-built with lots of excessive capability, still calling for new lines or all infrastructure, all because of lack of control devices. Unfortunately, excessive capacity and new lines do not increase total loadability proportionally. Even worse, sometimes switching off certain lines would be better off. In light of this, some technologies based on power electronics devices have been put in use and more breakthrough technologies are called for. The family of Flexible AC Transmission System (FACTS) has been adopted in generation, transmission and distribution systems. These power flow control solutions include, but not limited to, series reactor, phase shifting transformer, static synchronous compensator (STATCOM), static series synchronous compensator (SSSC), unified power flow controller (UPFC) and so forth. In general, FACTS has the principal role to enhance controllability and power transfer capability in ac systems. It involves conversion and/or switching power electronics in the range of a few tens to a few hundred megawatts.

The problems with today's FACTS devices or some other high-voltage high-power devices are they require bulky and complicated zigzag transformer in order to meet the grid requirements. However, these zigzag transformers are usually very expensive, bulky, lossy and prone to failure. Moreover, they are very slow (up to minutes to steady state after energizing) in dynamic response due to magnetizing current, and thus are not suited for fast-changing power flow control of intermittent and sporadic wind and solar power system. Therefore, it would be interesting to develop some technologies that can be used in transmission level and distribution level to eliminate transformers which utilize power electronics based device and provide higher efficiency, less cost and faster dynamic response.

Utilization of multilevel inverters is becoming more and more popular in recent years for high power applications [1-3]. Various topologies and modulation strategies have been investigated for utility and drive applications [4-7]. The commercially available Isolated Gate Bipolar Transistor (IGBT) are rated at 1200, 1700 Volts and100 Amperes, 200 Amperes or even higher. Multilevel inverter structure makes these market-available devices an enabling technology for power system and drive application possible.

1.2. Flexible AC Transmission Systems

The purpose of the transmission network is to pool power plants and load centers in order to minimize the total power generation capacity and fuel cost. The attractive part for transmission or generation planners is that FACTS technology opens up new opportunity for controlling power and enhancing the usable capacity of present, as well as possible updated lines [8-10]. By providing added flexibility, FACTS controllers can enable a line to carry power closer to its thermal limit rating [11]. Figure 1-1 shows a diagram for a typical two-bus power system.

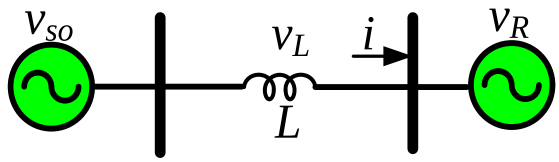

Figure 1-1 Diagram for two-bus power system.

The original active and reactive power P_0 and Q_0 with the uncompensated system is

$$\begin{cases} P_0 = \dfrac{V_{s0}V_R}{X_L}\cdot \sin\delta_0 \\ Q_0 = \dfrac{V_{s0}V_R\cos\delta_0 - V_R^2}{X_L} \end{cases} \quad (1.1).$$

From this expression, there are three basic variables that can be used to control the active and reactive power flow along a transmission line, which are: (1). Voltage (V_{s0} and V_R are sending and receiving end, separately); (2). Angle (δ_0) and (3). Impedance (X_L).

From the topological perspective, the FACTS controllers can be divided into three large categories [11]:

1. Series controllers: the series controllers inject voltage in series with the transmission line and as long as the voltage is in quadrature with the line current, it only supplies or consumes variable reactive power, thus makes possible to use capacitor for dc link. Figure 1-2 (a) shows a typical connection of series controllers with the transmission line;
2. Shunt controllers: the shunt controllers inject current into the system at the point of connection. Similarly, as long as the injected current is in quadrature with the line voltage, it only supplies or consumes variable reactive power into system. Figure 1-2 (b) shows a typical configuration of shunt controllers with transmission line;
3. Combined series-shunt controllers: the combined series and shunt controllers inject current into the system with the shunt part and voltage with the series part. Usually, a

common dc link is connected in between series and shunt part. Figure 1-2 (c) shows a typical configuration of combined series-shunt controllers with transmission line.

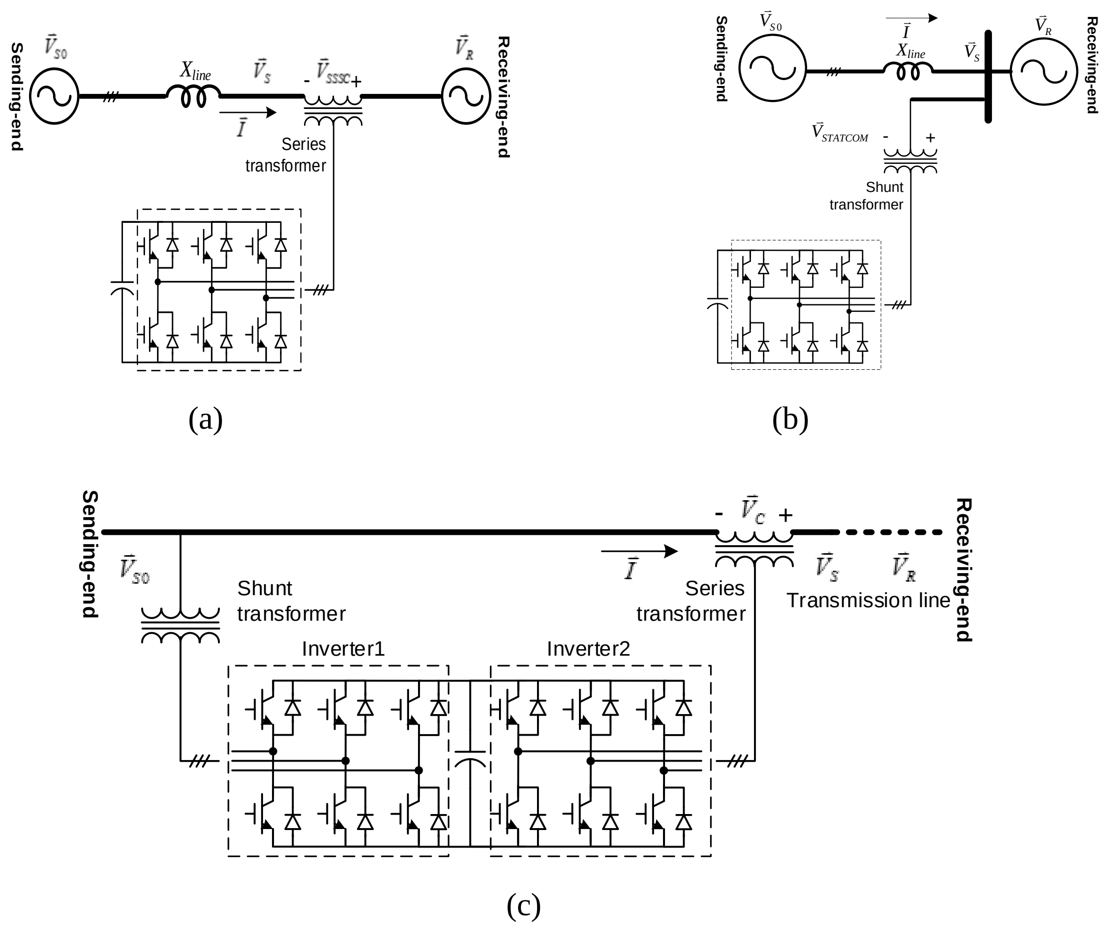

Figure 1-2 (a). Series controller; (b) shunt controller; (c). combined series and shunt controllers.

1.3. Custom Power

The technology of the application of power electronics to power distribution for the benefit of a customer or group of customers is called custom power (CP) [12]. Since through this technology, the utilities can supply value-added power to these specific customers. In broader definition, CP can also be viewed as a member of FACTS controllers. Furthermore, their topologies are similar to their FACTS controllers counterpart.

The compensating devices of CP are used for active filtering, load balancing, power factor correction and voltage regulation. The family of compensating devices has the following members [12]:

1. Distributed STATCOM (DSTATCOM): shunt connected device that can perform load compensation at load bus terminals or voltage compensation to a distributed bus. Figure 1-3 (a) shows a typical configuration of DSTATCOM with distribution level system;
2. Dynamic Voltage Restorer (DVR): series connected device, the main purpose of which is to protect sensitive load from sag/swell, interruptions in the supply side. Figure 1-3 (b) shows a typical configuration of DVR with distribution level system;
3. Unified Power Quality Controller (UPQC): This is a very versatile device that can inject current in shunt and voltage in series simultaneously in a dual control mode. Figure 1-3 (c) shows a typical configuration of UPQC with distribution level system.

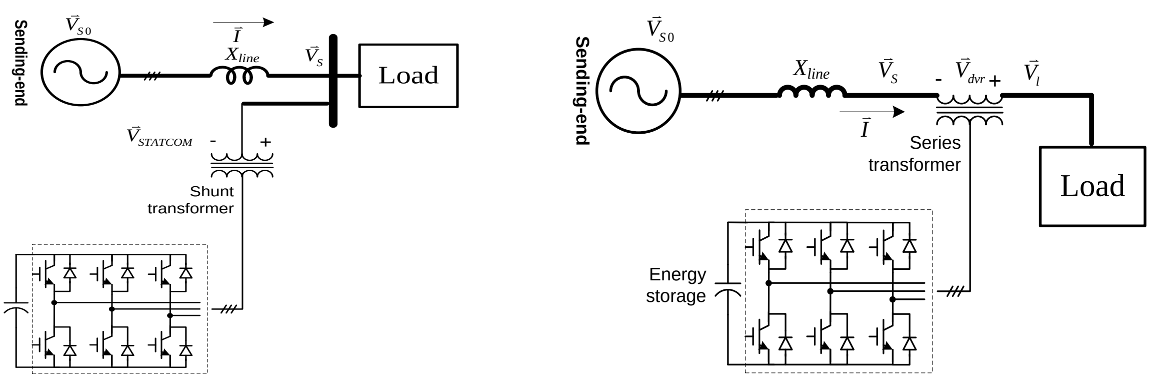

(a). (b)

Figure 1-3 Circuit configuration for Circuit configuration for (a) DSTATCOM; (b) DVR (c). UPQC.

Figure 1-3 (cont'd)

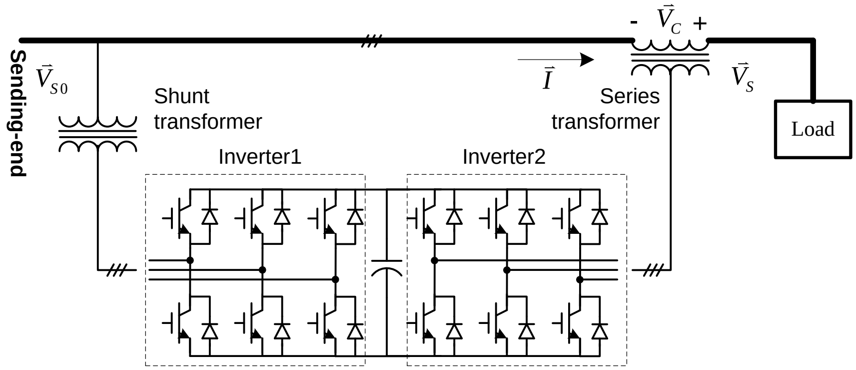

(c)

1.4. Multilevel Inverters

The first multilevel inverter was introduced in 1981 by Dr. Nabae [13]. Researchers have been working on developing different kinds of topologies for multilevel inverters, but the most frequently used topologies for multilevel inverter applications include three major types, cascaded multilevel inverter (CMI) , diode clamped inverter (DCI), and flying capacitor inverter (FCI) [1]. Their topological configurations are shown in Figure 1-4 (a), (b) and (c).

The benefits of using multilevel based inverter structure are:

1. Very low voltage shoot *dv/dt* and low distortion in the output voltage waveform;
2. Low distortion in input current waveform;
3. Enable utilization of commercial low voltage devices in medium/high voltage applications;
4. Low switching frequency thus low switching losses;
5. Low common mode voltage.

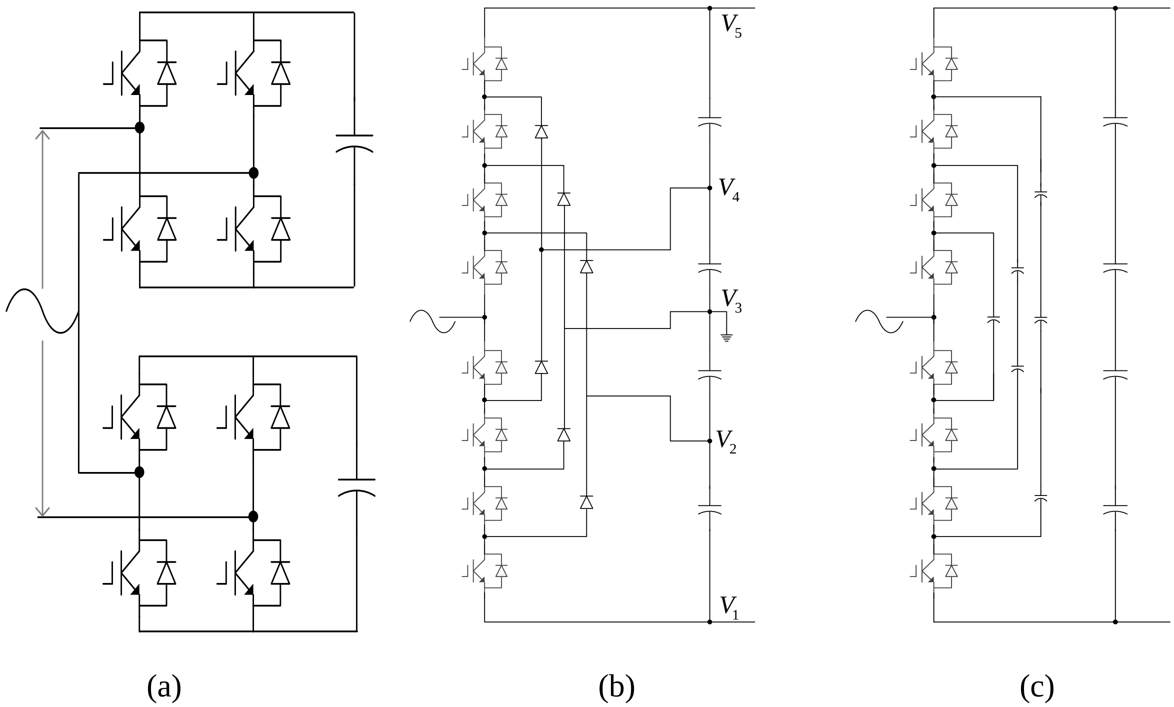

Figure 1-4 Single phase 5-level (a). cascaded multilevel inverter; (b). diode clamped inverter; (c). flying capacitor inverter.

Although the benefits shared by the multilevel structure, there exist different merits and demerits of different topologies [14]. Among which, the diode clamped inverter has bunch of clamping diodes. These clamping diodes not only raise costs but also cause packaging problems and exhibit parasitic inductances. Its counterpart, flying capacitor inverter requires large capacitance, and complicated to control. Also, it needs high switching frequency to balance each capacitor voltage. Comparatively, cascaded multilevel inverter is most suitable for modular design and is able to generate multistep staircase voltage waveform approaching a pure sinusoidal output voltage by increasing the number of levels. Furthermore, it needs no extra voltage balance circuits for dc link. Moreover, because of its modular structure, the packaging and layout is much easier. This makes it most suitable for high-voltage/high-power application.

1.5. Modulation Strategy for Cascaded Multilevel Inverter

Generally, two broad categories for multilevel inverter modulation are used, one is based on fundamental frequency modulation (FFM) [14-17] and the other is based on pulse width modulation (PWM) strategies [18-28]. For the PWM strategies, several approached have been investigated, proposed and documented in the literature including carrier-based PWM (CB-PWM) [20-22], multilevel space vector modulation (SVM) [23-25], and selective harmonics elimination PWM (SHE-PWM) [26-28]. These PWM based methods can be viewed as the extension of modulation strategy of traditional inverter in a multilevel inverter.

1.5.1 Fundamental Frequency Modulation (FFM)

In FFM, each device only switches once per line cycle and generates a multistep staircase voltage waveform approaching a pure sinusoidal output voltage by increasing the number of levels. Figure 1-5 shows an example of 11-level cascaded multilevel inverter with FFM. Detailed discussion regarding the FFM and its implementation will be shown in later chapter.

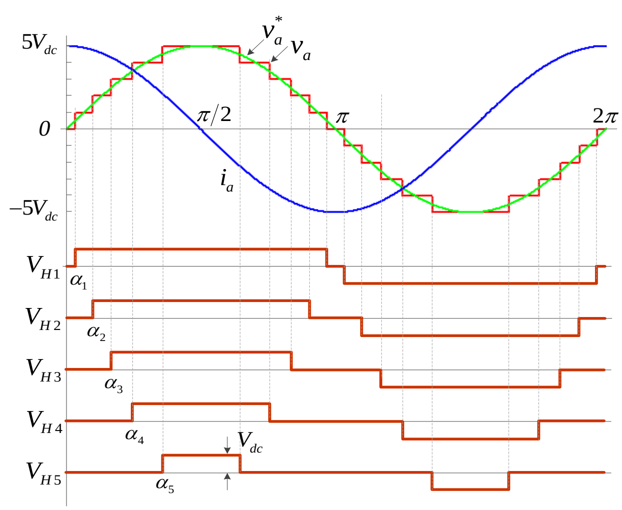

Figure 1-5 Operation principle of FFM.

1.5.2 Carried-based PWM (CB-PWM)

Take seven-level CMI based inverter for an example. Figure 1-6 shows phase shifted CB-PWM strategy. For an m-level inverter, the number of carriers is (m-1). The phase shift is $360^{\circ}/(m-1)$. With this SPWM strategy, the dominant lower order harmonics are pushed to around $(m-1)*f_{sw}$, where f_{sw} is the switching frequency of semiconductor devices. Or paraphrase, the equivalent switching frequency of the inverter is $(m-1)*f_{sw}$. Figure 1-7 shows another method addressed as level shifted CB-PWM, the number of carriers is also (m-1).

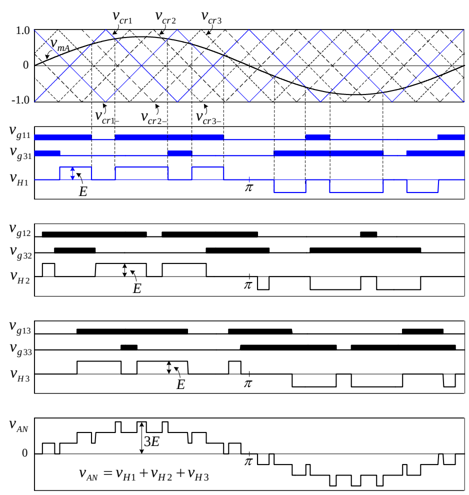

Figure 1-6 Carried based phase shifted PWM for multilevel inverter [29].

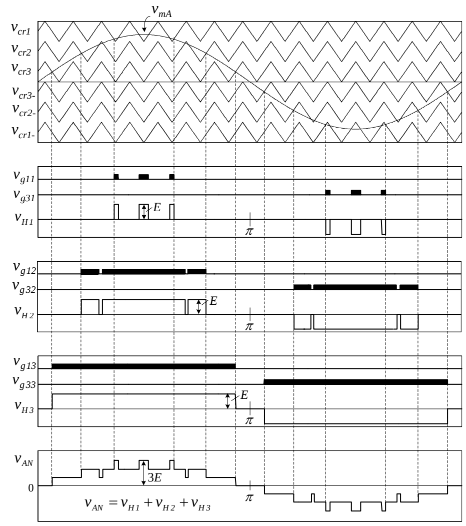

Figure 1-7 Carrier based level shifted PWM for multilevel inverter [29].

1.5.3 Multilevel Space Vector PWM (SVM)

The basic principle for SVM modulation is for a given length and position in space, V_{ref} can be approximated by three nearby stationary vectors, and based on these chosen vectors, switching states are selected and gate signals are generated. Note that the switching sequence is not unique, but two general requirements need to be satisfied:

1. The transition from one switching state to the next involves only two switches in the same inverter leg, one being turned on and the other turned off;

2. The transition for V_{ref} moving from one sector to the next requires no or minimum number of switches.

The method used in traditional two-level inverter can be easily extended to use in multilevel inverters. The adjacent three vectors can synthesize a desired voltage vector by computing the duty cycles (T_j, T_{j+1}, T_{j+2}) for each vector.

$$V^* = \frac{(T_j V_j + T_{j+1} V_{j+1} + T_{j+2} V_{j+2})}{T} \quad (1.2).$$

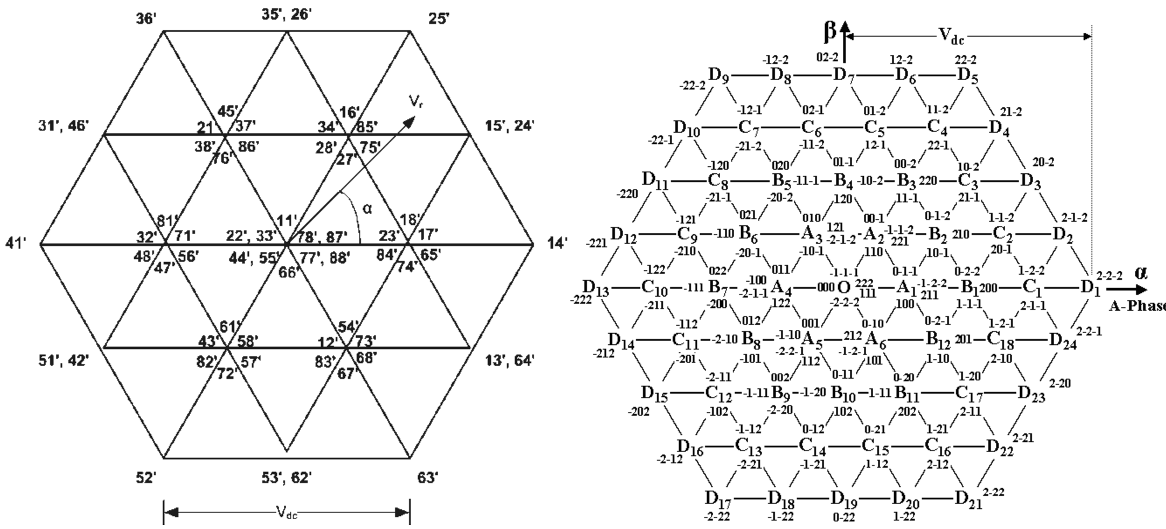

Figure 1-8 Space vector diagram for three-level and five-level inverters [29].

1.5.4 Selective Harmonic Elimination PWM (SHE-PWM)

In order to achieve a wide range of modulation indexes with minimum THD for the synthesized waveforms, SHE-PWM has been introduced. SHE-PWM is utilized to get rid of low-order harmonic components in the waveform. The selective harmonic elimination (SHE) PWM was first introduced in 1973 for two-level high-power inverter [30]. As shown in Figure 1-9, since not all the switching are independent from each other, it is possible to eliminate some unexpected harmonic components. Furthermore, the amount of eliminated lower order harmonics is determined by the number of switching angles instead of voltage levels. However, the equations for solving these switching angles are also non-linear, thus it is time-consuming for on-line calculation.

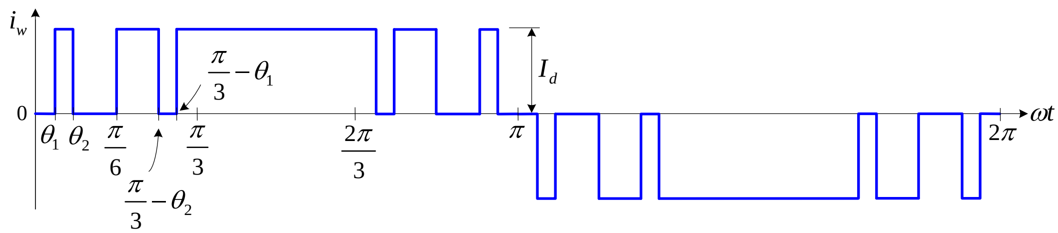

Figure 1-9 Example of switching angle for an inverter [29].

1.6. Multilevel Inverter in FACTS Application

The aforementioned FACTS controllers, no matter in distribution level or transmission level, have to reply on the bulky and complicated zigzag transformers for isolation and output voltage waveform requirement. The problems with the zigzag transformers are: 1) very expensive (30-40% of total system cost); 2) lossy (50% of the total power losses); 3) bulky (40% of system real estate area and 90% of the system weight); and 4) prone to failure [31].

The enabling technologies of multilevel inverter, especially the cascaded multilevel inverter has made it possible to use multilevel structure in FACTS application. The CMI-based STATCOMs (up to ±200 Mvar) have been installed in Europe and Asia [15, 32, 33]. Moreover, it has also been demonstrated that CMI-based SSSC can be directly coupled to the transmission line without coupling transformer [34]. However, the CMI could not be directly used in the conventional UPFC, because the conventional UPFC requires two inverters connected back-to-back to deal with active power exchange. To address this problem, a UPFC with two face-to-face connected CMIs was developed in [16] to eliminate the zigzag transformers that are needed in the conventional multi-pulse inverter-based UPFC. However, it still required an isolation transformer. The circuit diagram is shown in Figure 1-10.

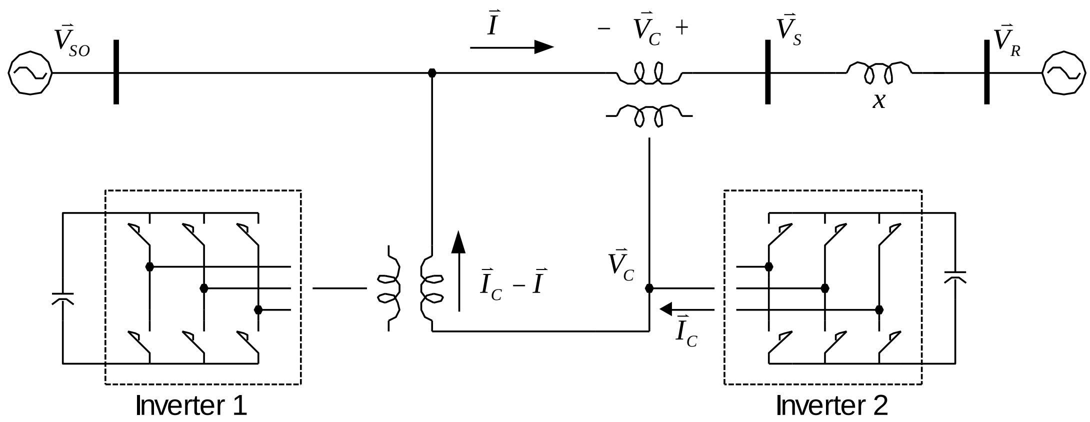

Figure 1-10. Circuit configuration of UPFC proposed in [16].

To eliminate the transformer completely, a new transformer-less UPFC based on an innovative configuration of two CMIs has been proposed in [35]. The system configuration is shown in Figure 1-11. As shown in Figure 1-11 (a), the transformer-less UPFC consists of two CMIs, one is series CMI, which is directly connected in series with the transmission line; while the other is shunt CMI, which is connected in parallel to the sending end after series CMI. Each CMI is composed of a series of cascaded H-bridge modules as shown in Figure 1-11 (b). The transformer-less UPFC has significant advantages over the traditional UPFC such as highly modular structure, light weight, high efficiency, high reliability, low cost, and a fast dynamic response.

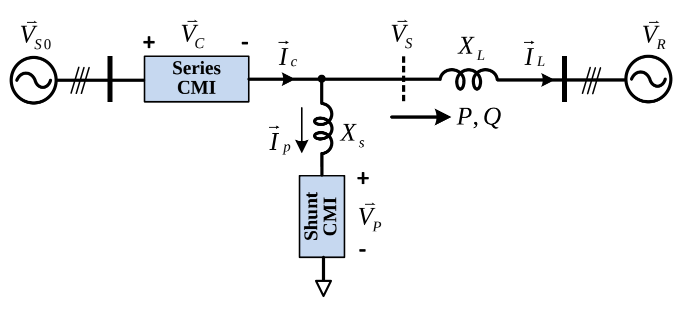

(a)

Figure 1-11 New transformer-less UFPC, (a) System configuration of transformer-less UPFC; b) One phase of the cascaded multilevel inverter.

Figure 1-11 (cont'd)

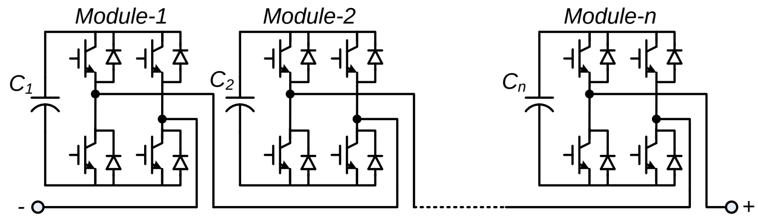

(b)

1.7. Outline of the Dissertation

This dissertation will present detailed modeling, modulation strategy, control and application examples of the proposed transformer-less UPFC. The feasible applications of cascaded multilevel inverter (CMI) in FACTS application are well addressed.

Chapter 2 first talks about an extended application of CMI based STATCOM with the virtual inertia control and its comparison with some existing methods.

Chapter 3 introduces the totally transformer-less unified power flow controller (UPFC) configuration for the transmission level system application. Modeling, control and experimental results with the proposed novel topology are included.

Chapter 4 demonstrates an application of transformer-less UPFC for interconnecting two synchronous grids with large phase difference. The circuit configuration is same as mentioned in previous chapter but at a higher voltage and higher power rating.

Chapter 5 presents another application example of transformer-less UPFC in a highly congested grid. The UPFC is able to control bidirectional power flow and make parallel operation possible for two different feeders.

Chapter 6 proposes an extended study of transformer-less UPFC. Another topology with CMI based UPFC is introduced and compared with the already beneficial structure of transformer-less UPFC. Their converter rating, implementation and analytical results are presented.

Chapter 7 summarizes the content and the contribution of this work. Some recommendations for future work are also presented.

CHAPTER 2 Virtual Inertia Control of CMI Based STATCOM

This chapter shows a comparison between synchronous condenser (SC) and STATCOM in terms of inertia frequency response (IFR) with synchronous generator (SG). It has long been argued that, as a rotating-mass-based reactive power compensation device, SC will contribute to the total inertia of the network from its stored kinetic energy. Whereas, its counterpart, the voltage source converter (VSC) based STATCOM, will only supply reactive power and maintain voltage balance. However, the energy stored in the dc-link capacitor of the STATCOM, especially the cascaded inverter based STATCOM whose dc-link capacitance is relatively large, if properly controlled, can also contribute to the IFR. A Matlab/Simulink model of SG equipped with SC and STATCOM is presented in this chapter. It is demonstrated that STATCOM can provide competitive or even better IFR during disturbance condition. Both theoretical and simulated results are provided.

2.1 Introduction

Synchronous generator (SG) has been in service in US power system from long back. The operation and control of a SG is mature in practice and it helps to maintain the power system reliability and stability. However, with the advancement of modern power system and increasing types of load, the requirement for the transient stability has become more rigid. Various reactive compensation devices have been called for to support power system stability. These devices can be roughly classified into three major categories: synchronous condenser (SC), static Var compensator (SVC), and static synchronous compensators (STATCOM).

A synchronous condenser, by its nature, is a synchronous generator operating without a prime mover. It supports network voltage by providing reactive power compensation and additional short circuit power capacity. Furthermore, it can also support system frequency stability by increasing network inertia.

STATCOM, arising from the family of FACTS device, has been utilized widely in recent years. A STATCOM is a controlled reactive power source, which typically includes a voltage source converter (VSC) and a DC link capacitor connected in shunt through coupling transformer, capable of generating and/or absorbing reactive power. Alternatively, cascaded multilevel inverter (CMI) based STATCOM eliminates the bulky transformers and will respond much faster. It is well suited for Var compensation/generation applications [31].

Since there is no mechanical part in VSC based STATCOM, it has long been admitted that STATCOM makes no contribution to the frequency stability of the SG during load disturbance. However, STATCOM can be properly controlled to make virtual inertia response. The stored energy in dc-link capacitor can be utilized by varying the dc-link voltage during disturbance condition. This proposed methodology focuses on short-term oscillations and incorporates no long-term power regulation, thus it needs no mass storage device. Moreover, since SC and SG are synchronized with the transmission network, the largest allowable frequency deviation is limited and locked by the system. In some scenario, the STATCOM will demonstrate even better performance in terms of inertia frequency support than SC. This is very attractive in power system applications since bidirectional VSCs can work in generative and motoring modes similar to SMs.

The rest of the chapter is organized as follows. Section 2.2 shows the frequency response of a SG and wind turbine. Section 2.3 describes operation principle of SC and its integration with SG. Section 2.4 addresses nominal operation of the CMI-based STATCOM and modified virtual inertia control (VIC). Simulation results and discussions are presented in Section 2.5. Conclusion and future work are included in Section 2.6.

2.2 Frequency Response of Generator

2.2.1 Frequency Response of Synchronous Generator

The transient frequency response of the synchronous generator, according to its time frame range, can be roughly divided as inertial frequency response (IFR), primary frequency response (PFR) and secondary frequency response (SFR) [36].

In the first few milliseconds or seconds following the loss of a large power generator or the increase of load command, the grid frequency starts to drop. These initial frequency dynamics are regulated by the inertial response of the generators that still remain online. The synchronous generators release their stored kinetic energy into the grid, reducing the initial rate of change of frequency (ROCOF) and allowing governor to catch up and contribute to frequency stabilization [37]. It is the first step and the natural response of a SG under load disturbance.

The step following the IFR is the Primary Frequency Response (PFR). PFR can be understood as the instantaneous proportional increase or decrease in real power output in response to system frequency deviations. This response is in the direction that stabilizes frequency. It is attained due to governor action to instantly act relative to the frequency deviation. This usually takes place within seconds to tens of seconds.

Finally, it is the secondary frequency response (SFR). SFR is executed by automatic generation controller (AGC) and often referred to as load frequency controller (LFC). The AGC utilizes reserves to restore the frequency closer to scheduled frequency. Generally, the SFR can take place from seconds to minutes. These three steps happen sequentially so that frequency is recovered back to 60 Hz [38]. Figure 2-1 shows a diagram of governor power frequency control. The analysis of this chapter is focused on the inertial frequency response.

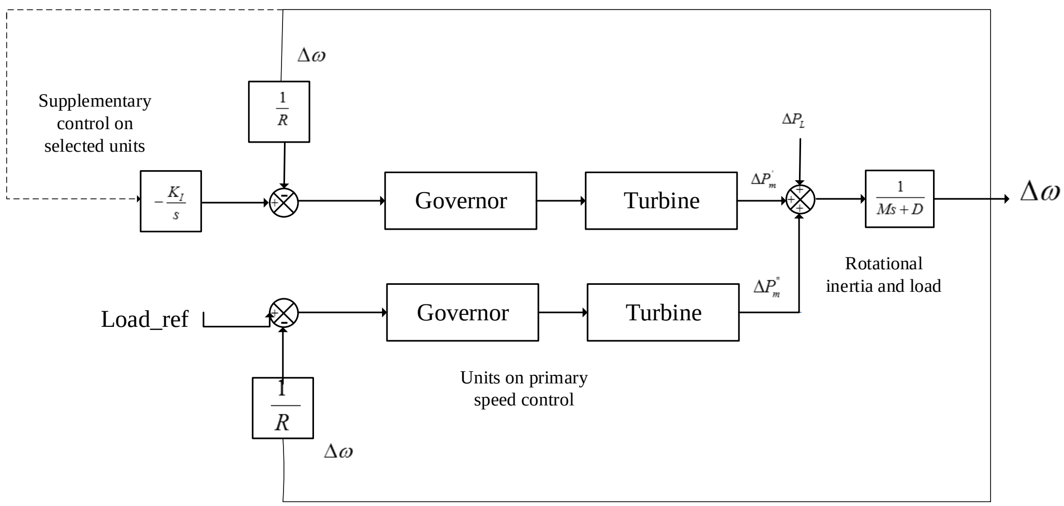

Figure 2-1 Governor power frequency control.

During the period of IFR, the frequency variation, directly after a significant generation-load imbalance, is determined by the equation

$$P_m - P_e = \frac{d\left(\frac{1}{2} \cdot J_{system} \cdot \omega_{el}^2\right)}{dt} \tag{2.1),}$$

where P_m is the generated power, P_e is the demanded power. The right side of the equation is the derivative of the kinetic energy stored in the generator.

Another constant called H constant (also known as inertia constant) is defined as [38]

$$H = \frac{\textit{Stored energy at rated speed} \text{ in MW} \cdot \text{S}}{\text{MVA rating}} = \frac{1}{2} \frac{J\omega_{om}^2}{VA_{base}} \tag{2.2).}$$

The inertia constant is measured in seconds and it falls typically in the range of 2-9 s for large power plants [39]. Figure 2-2 shows a typical waveform of a SG subjected to a loss of generation unit or a sudden increase in load. If the inertia available in the grid is large, the drop in frequency is not that much. The nadir drops down to 59.65 Hz in this case. When the frequency drops, the inertia energy from SG is automatically released.

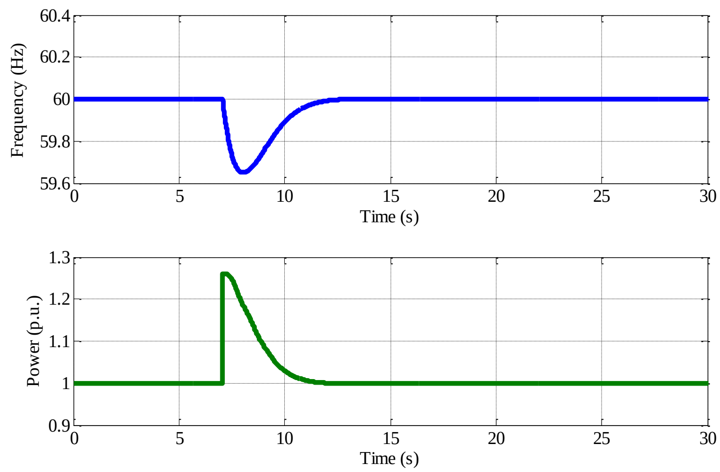

Figure 2-2 Typical system frequency response for a generation outage.

The energy generated by the generator is relatively large. However, the available energy during the initial transient of the system is not that much since the SG needs to be in synchronism with the system. The grid code has set up the minimum frequency drop it can be, and it is typically within the range of 0.1-1 Hz [36]. Thus, the actual available inertia energy is proportional to its inertia constant *H*,

$$H\_available = \frac{\frac{1}{2}J\omega_{om}^2 - \frac{1}{2}J\omega_{\min}^2}{MVA} \propto \frac{(\omega_{om}^2 - \omega_{\min}^2)}{\omega_{om}^2} \cdot H \tag{2.3}$$

Only this limited amount of energy will be utilized for IFR. Here inertial constant *H* is adopted to describe the different ratings of the SG. As can be seen from Figure 2-3, the actual available inertia energy is in the time frame of 7-300 ms.

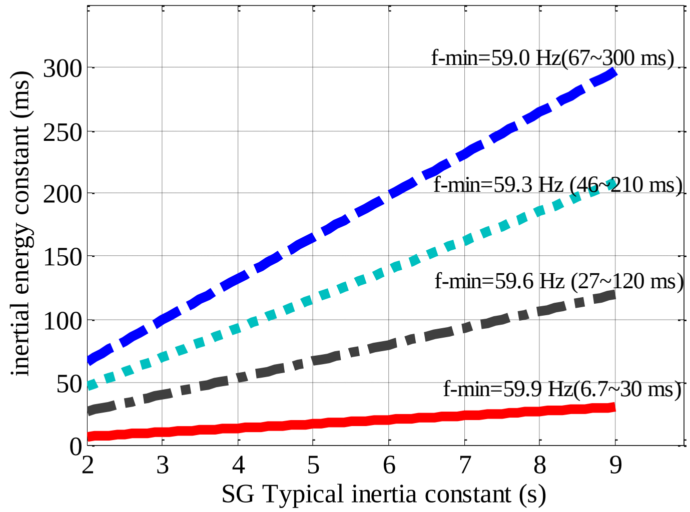

Figure 2-3 Available inertial energy from SG with different minimum frequency.

Given this very limited value of available inertia constant of SG, it is worthy studying the possible methods of improving IFR. Like mentioned previously, SC, SVC and STATCOM are the most three frequently used reactive power compensators, and among which, only SC have been claimed to contribute to the total inertia of the system. However, it is not the obvious truth. The following section will address the possible contribution from STATCOM for IFR and a comparison between SC and STATCOM have been made.

2.2.2 Frequency Response of Synchronous Condenser

SC has been used since 1930 as a source of dynamic VARs (both inductive and capacitive) to improve system stability and support voltage under varying load conditions and contingencies. Its field is controlled by a voltage regulator to either generate or absorb reactive power as needed to control the voltage of the power system. The synchronous condenser is a rotating machine without a prime mover. Because of this, they can provide a lower inertia from the kinetic energy stored in the rotating mass. The typical H value of SC is 1-1.25 s [39], thus the available inertial energy from the SC can be estimated similarly using equation in (2.3). As can be seen from Figure 2-4, the actual available inertia energy of SC is in the time frame of 3-41 ms.

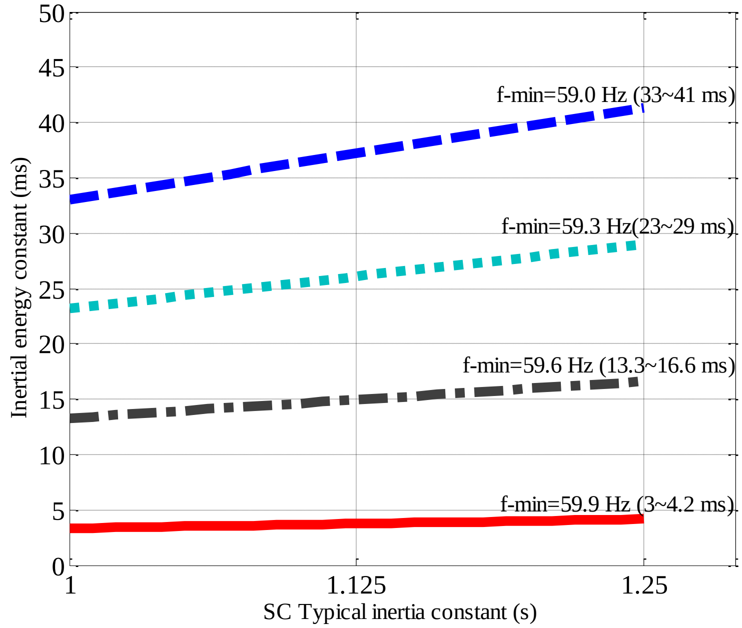

Figure 2-4 Available inertial energy from SC with different minimum frequency.

Figure 2-5 shows a typical connection of a SC with SG. As have been discussed in [40], SC shows a good dynamic performance for reactive power compensation. Furthermore, SC will contribute to the total inertia of the system as well and the ROCOF is reduced.

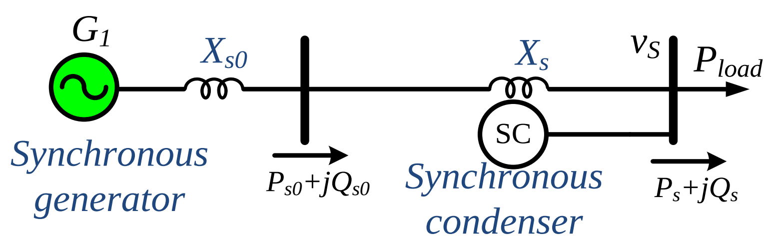

Figure 2-5 SG with SC connected to load bus.

Although the benefit of SC, the drawback of synchronous condenser is that it calls for high demand of cooling for thermal consideration and it cannot be controlled fast enough to compensate for rapid load changes.

For the above two perspectives, STATCOM shows a better performance since VSC based FACTS device has a much quicker response time and very low thermal design requirement.

2.2.3 Synthetic Inertial Control of Wind Turbine

Similar to the inertia energy in the SG's rotating mass, significant amount of kinetic energy is stored in the rotating turbine blades with typical inertia constants in the range of 2-6 s [41]. However, unlike the inherent response of conventional synchronous machines, inertial wind turbine generator (WTG) response is dependent on active controls. Since the rotating mass of variable-speed wind turbines is decoupled from the grid frequency and does not provide an inertial response unless controlled for the purpose. Figure 2-6 shows a typical response of the wind turbine under load disturbance. As can be seen from Figure 2-6, the WTG power generation reminds unchanged since it is driven by its own maximum power point tracking (MPPT) control [41].

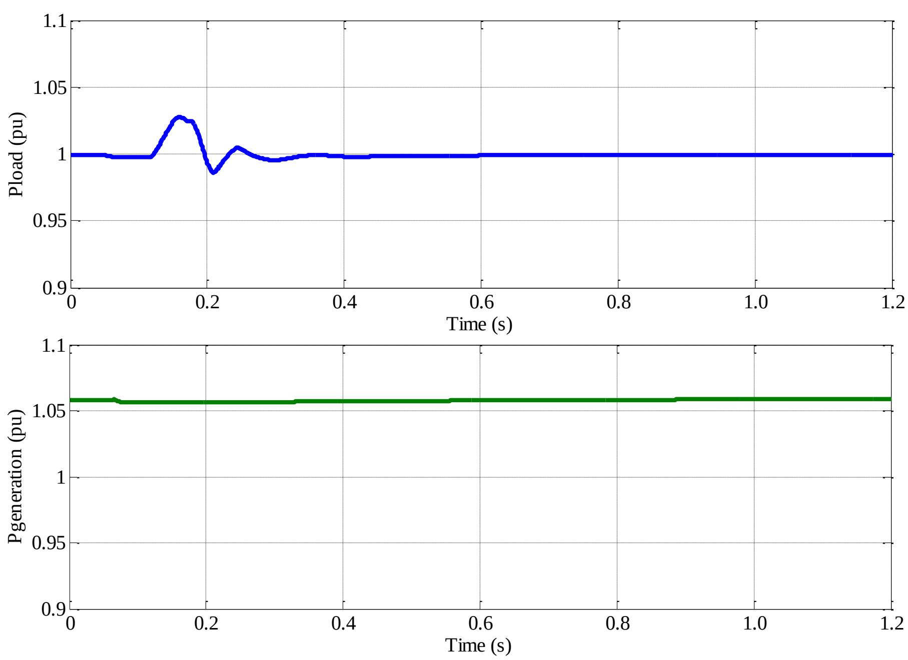

Figure 2-6 Typical system frequency response for a wind-turbine generator.

A literature survey shows that researchers have proposed a wind-turbine synthetic inertial control (SIC) to deal with inertial frequency response problem [42-44]. The principle of wind-turbine SIC is well known and involves modification of the demanded torque in response to a change in system frequency by adding an extra torque term [42]. Figure 2-7 shows the rotating-mass-based virtual inertia implementation of wind turbine.

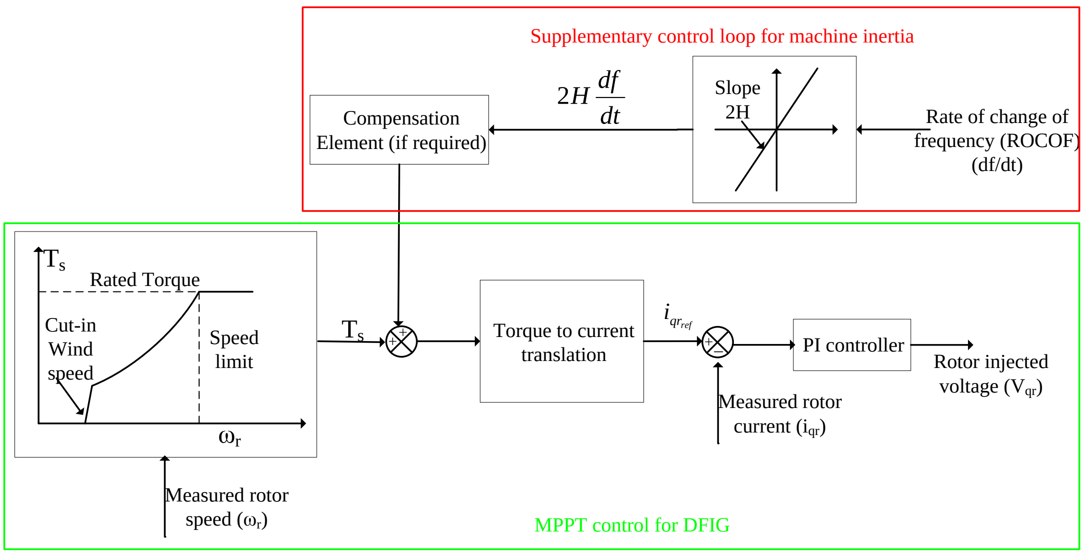

Figure 2-7 Wind synthetic inertia control diagram.

It seems that this rotating mass based virtual inertia does not need any new component or de-rating, its performance is highly dependent on DFIG rotating speed during disturbance. This rotating speed is a function of wind speed which is unpredictable. When wind speed is too slow or the frequency drop is too high, this supplementary control has to be deactivated. Furthermore, the maximum wind power extraction was sacrificed to enhance the system stability. This changing torque operating point will lead to non-optimal operation of wind generator or unnecessary reserve.

Wind turbine, especially the offshore WP generator, has been equipped with STATCOM at the load bus for the reactive power compensation purpose. It has been shown in [45] that

STATCOM can perform inertial response for the frequency regulation purpose. The following section will address the possible contribution from STATCOM for IFR in WP.

2.3 Modeling and Analysis of STATCOM for Frequency Support

It has been witnessed that VSC based STATCOMs are built all over the world. However, the benefit of STATCOM is not fully potential. As a VSC based reactive compensator, STATCOM has been penalized for not being able to help with frequency regulation. The reason is that it has no rotating mass thus has no stored kinetic energy. However, it will be shown in this section that electric energy stored in the dc-link capacitor of STATCOM, especially for the CMI-based STATCOM, has large electric energy stored, will significantly help the inertial response if properly controlled.

2.3.1 Normal Operation of STATCOM

Basically, the STATCOM system is connected to the weak grid bus at PCC. The CMI-based system is composed of three main parts: a multilevel-cascaded VSC with separate DC sources, a coupling inductor and a controller, as shown in Figure 2-8 [46].

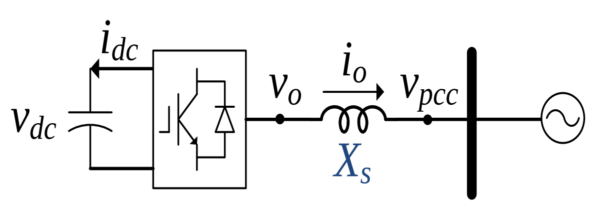

Figure 2-8 Single line diagram of the cascaded multilevel inverter based STATCOM.

The exchange of real and reactive power between cascaded inverter and the power system can be controlled by adjusting the amplitude and phase angle of the converter output voltage.

Usually, it can be divided into capacitive mode and inductive mode, as shown in Figure 2-9. Two important control laws of cascaded-multilevel VSC for STATCOM application:

1. The amount of transferred reactive power (Q) can be controlled by adjusting the magnitude of converter output voltage;
2. The amount of transferred real power (P) can be controlled by adjusting the phase angle of the converter output voltage with respect to the voltage at PCC.

2.3.2 Inertia Energy from STATCOM

As a VSC based reactive power compensator, STATCOM have no real "inertia". However, we use a term of virtual inertia constant in this chapter, similar as defined in [31], associated with the inertia constant in synchronous rotary condensers,

$$H_{STATCOM} = \frac{\frac{1}{2} C \cdot N \cdot (V_{dc\_\max}^2 - V_{dc\_\min}^2)}{S_{STATCOM}} \quad (2.4).$$

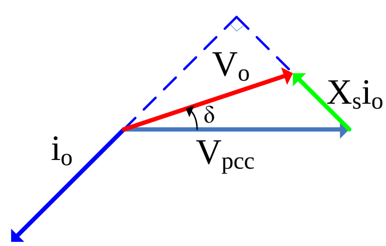

(a). operation in non-ideal condition

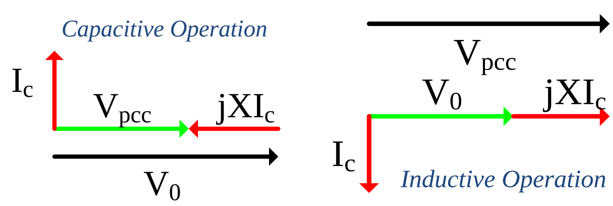

(b). operation in lossless condition

Figure 2-9. Normal operation of STATCOM as var generator.

The voltage rating of the dc link is determined by the connected network. A detailed analysis can be referred to [14]. Figure 2-10 shows a schematic for CMI-based STATCOM for the utility connected application.

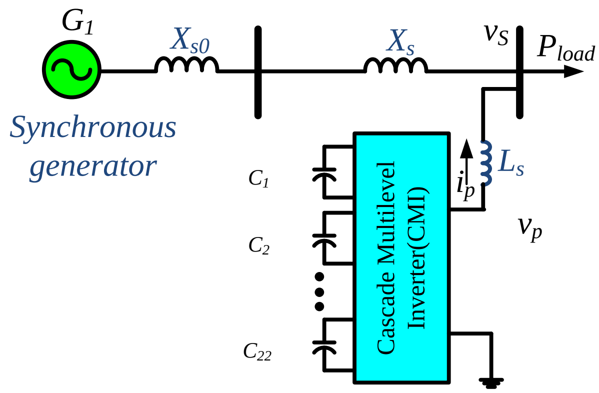

Figure 2-10 SG with STATCOM connected to load bus.

Figure 2-11 shows a schematic for cascaded inverter based STATCOM for the WT generator connected application. The wind power generator can be ranged from double fed induction generation (DFIG), fixed-speed induction generator (FSIG) or permanent magnet synchronous generator (PMSG).

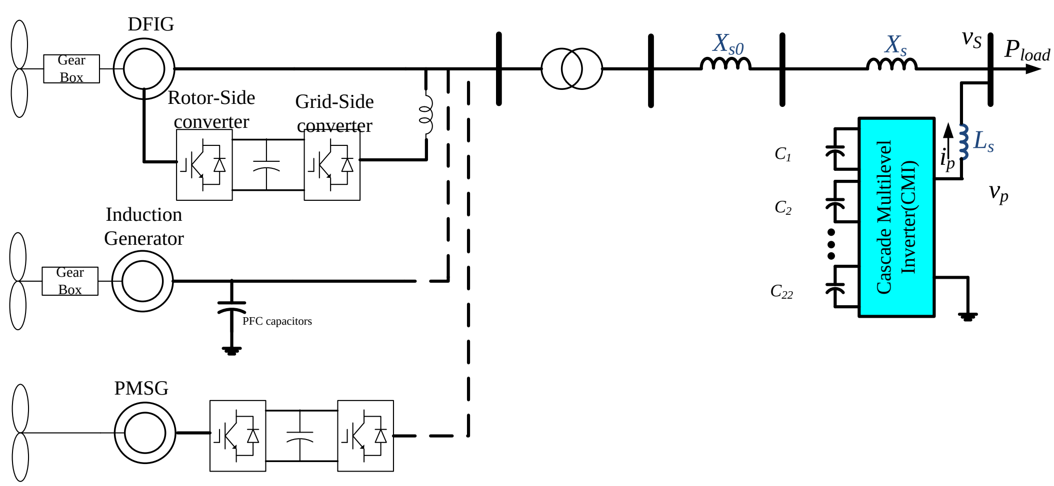

Figure 2-11 Wind power plant with CMI-based STATCOM.

Dc-link voltage has limited variation range. For the design of CMI-based STATCOM, some redundancy has been considered and in this analysis, 10% redundancy is used so the minimum voltage rating is taken to be 0.9 pu. Besides, the maximum voltage V_{dcmax} cannot exceed the voltage ratings of the power semiconductor devices and dc-link capacitors. In this analysis, 1.4 pu is taken as the upper limit.

Another important parameter that determines the energy capacity is the dc link capacitor. For the proposed cascade inverter, since each phase has its own separate dc capacitors, calculation of the required capacitance of each H-bridge dc capacitor needs to cover both positive-sequence and negative-sequence reactive power [14]. The required capacitance, C_i, can be formulated as

$$C_i = \frac{\Delta Q_i}{\Delta V_{dc}} = \frac{\int_{\theta_i(t)}^{T/4} \sqrt{2} I \cos \omega t dt}{2\varepsilon V_{dc}} = \frac{\sqrt{2} I (1 - \sin \theta_i)}{2\omega\varepsilon V_{dc}} \tag{2.5}$$

Therefore, the total capacitance for a three-phase M-level inverter is,

$$C = 3 \sum_{i=1}^{(M-1)/2} C_i \tag{2.6}$$

Table 2.1 shows the parameters used for the theoretical analysis and simulation.

Table 2.1 System Parameters for Virtual Inertia Control of STATCOM.

Parameter	Value
S (rated power)	1 MVA
V_{s0} (ph-ph rms)	13.8 kV∠0, 60 Hz
V_{dc}	600 V
V_{dcmin}	540 V
V_{dcmax}	840 V
Number of CMI per phase	22 (10% redundancy)
H-bridge capacitance	4700 μF

Therefore, the relationship between initial dc link voltage (V_{dc0}), dc-link capacitance (C_{dc}) and inertia constant from STATCOM ($H_{STATCOM}$) is shown in Figure 2-12.

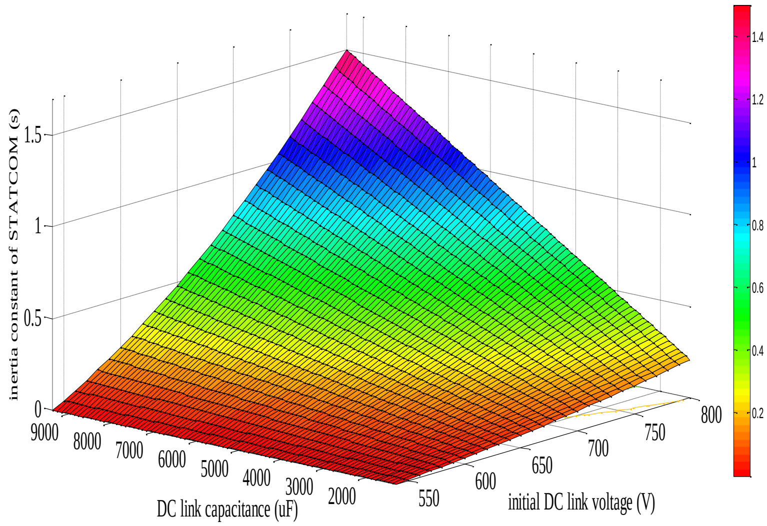

Figure 2-12 Relationship between V_{dc}, C_{dc} and $H_{STATCOM}$.

A comparison between SC and STATCOM for possible available inertial energy using parameters from Table 2.1 is shown in Figure 2-13. As can be obtained from Figure 2-13, STATCOM can provide possible competitive inertia energy compared to SC, and under some conditions, it will provide even more inertia energy. This is largely because that although the inertia response from SG and SC is natural and automatic, it obviously limited by the frequency deviation due to the grid code. However, as a voltage controlled device, the STATCOM is independent of that requirements and can provide large inertia energy given enough short term energy storage.

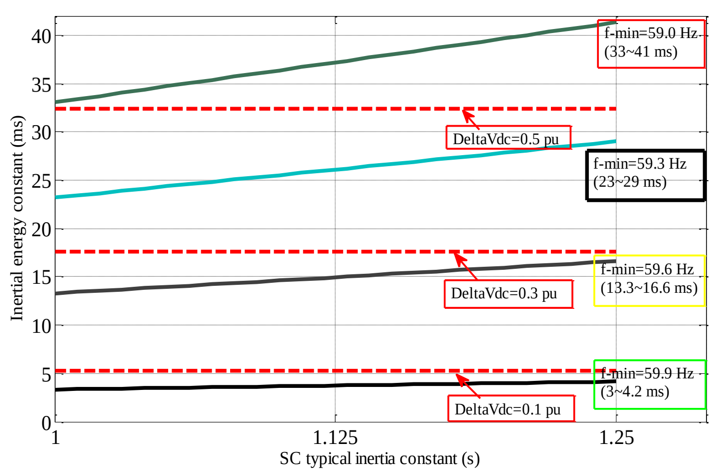

Figure 2-13 Theoretical inertial energy comparison between STATCOM and SC.

2.3.3 Virtual Inertia Control for STATCOM

In order for the STATCOM to generate desired active current (i_d^*) and reactive current (i_q^*). The decoupling feedforward and feedback control has been used as the controller [17]. The relationship is given as in

$$\begin{bmatrix} V_{pd}^* \\ V_{pq}^* \end{bmatrix} = \begin{bmatrix} V_{Sd} + \omega L I_{pq}^* - \left(L \dfrac{d}{dt} I_{pd}^* + R I_{pd}^* \right) \\ V_{Sq} - \omega L I_{pd}^* - \left(L \dfrac{d}{dt} I_{pq}^* + R I_{pq}^* \right) \end{bmatrix} \tag{2.7}$$

And

$$\begin{cases} V_p^* = \sqrt{V_{pd}^{*2} + V_{pq}^{*2}} \\ \alpha_p^* = \tan^{-1}\left(\dfrac{V_{pq}^*}{V_{pd}^*} \right) \end{cases} \tag{2.8}$$

The typical control of CMI-based STATCOM is known as balancing control and individual control. The traditional control principle is to maintain the DC link voltage stable and balanced between different modules. In this study, since it is desired to utilize the energy stored in the DC link capacitor during load disturbance or frequency variation, a modified control strategy is utilized. Similar deviation has been adopted in [47]. The equation of the machine angular motion is given in

$$\frac{2H}{f_0} \cdot \frac{df}{dt} = P_M - P_E = \Delta P_1 \ \ (pu) \tag{2.9}$$

In order to equate the available power of the dc link capacitors to that of an electrical machine, the capacitor dynamics (in terms of dc link voltage and output power) are presented in (2.10):

$$\frac{NCV_{DC}}{S_{STATCOM}} \cdot \frac{dV_{DC}}{dt} = P_{in} - P_{out} = \Delta P_2 \ \left(pu\right) \tag{2.10}$$

The virtual inertia constant $H_{STATCOM}$ can be obtained by equating the SG power variation in (2.9) with capacitor power in (2.10) yields,

$$\frac{2\frac{W_{STATCOM}}{W_K + W_{STATCOM}} H_{STATCOM}}{f_0} \cdot \frac{df}{dt} = \frac{NCV_{DC}}{S_{STATCOM}} \cdot \frac{dV_{DC}}{dt} + \frac{2\frac{W_{STATCOM}}{W_K + W_{STATCOM}} H}{f_0} \cdot \frac{df}{dt} \tag{2.11}$$

The new dc link voltage reference is obtained through the relationship between frequency variation and inertial energy can be used from dc link,

$$\frac{2H_{STATCOM} \cdot f}{f_0} = \frac{NCV_{DC}^2}{2S_{STATCOM}} + 2H_{STATCOM} - \frac{NCV_{DC0}^2}{2S_{STATCOM}} \tag{2.12}$$

Then the new dc-link voltage reference can be obtained as,

$$V_{DC}^{*} = \sqrt{\frac{4S_{STATCOM}H_{STATCOM}}{NCf_0} \cdot f - K_2} \tag{2.13}$$

where, $K_2 = (4S_{VSC}H_{VSC})/(NC) - V_{DC0}^2$

Based on the above analysis, the virtual inertia control (VIC) strategy of the STATCOM is presented in Figure 2-14. It is modified from traditional control.

To verify the working principle of the proposed VIC controller, a simulation has been carried out. The simulated waveform is shown in Figure 2-15. The active current reference is commanded from frequency variation and reactive current reference stays constant. It can be seen that I_{pd} rapidly tracks the step-changing reference while the reactive current I_{pq} remains unchanged. Complete decoupled control is achieved. Next section will show simulation results of the STATCOM with the proposed VIC control in system study.

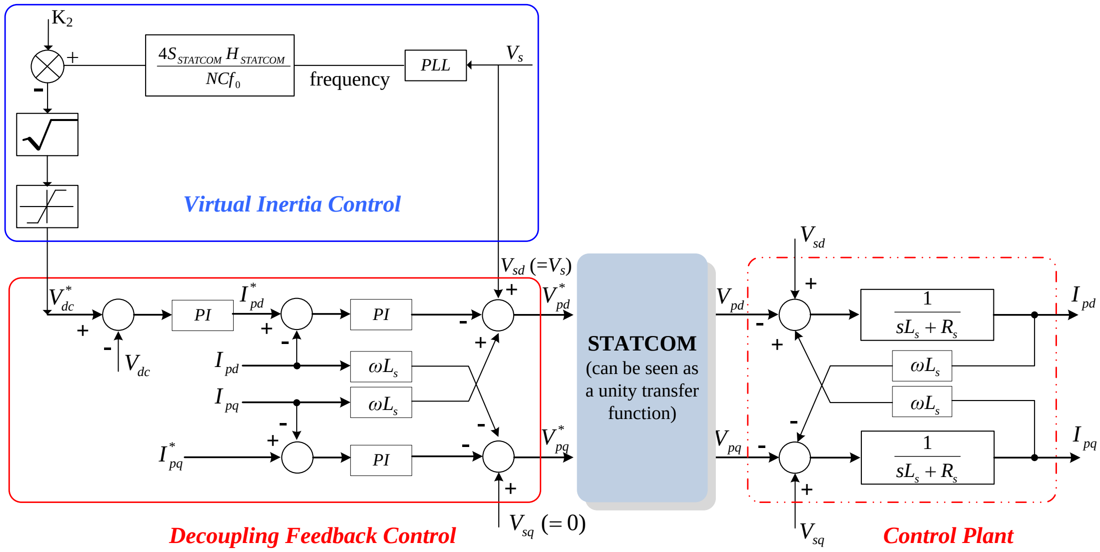

Figure 2-14 Virtual inertia control for CMI-based STATCOM.

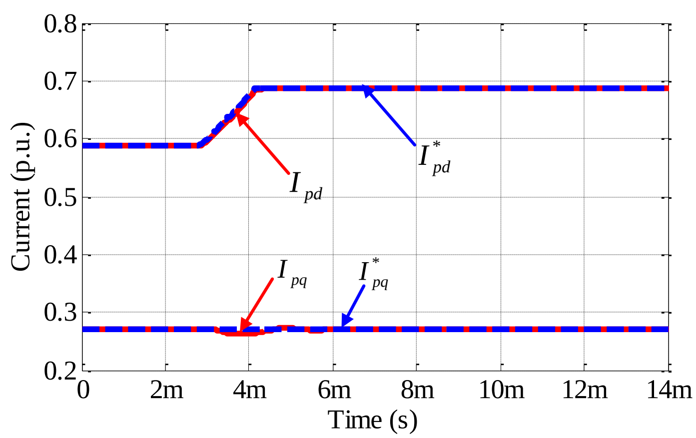

Figure 2-15 Simulated waveforms showing virtual inertia based decoupling feedback control for CMI-based STATCOM.

2.4 Simulation Results

The effectiveness of the proposed VIC of STATCOM is validated in Matlab/Simulink. The tested system is a two-area-four-machine system [38]. It compromises with two fully symmetrical of four machines, and good for studying low frequency electromechanical oscillation and inertial response of the generator. Each generator equipped with its own governor and excitation control. The system illustration is shown in Figure 2-16. The tested CMI-based

STATCOM and SC are connected to load bus at L7 and L9 for system dynamic performance comparison.

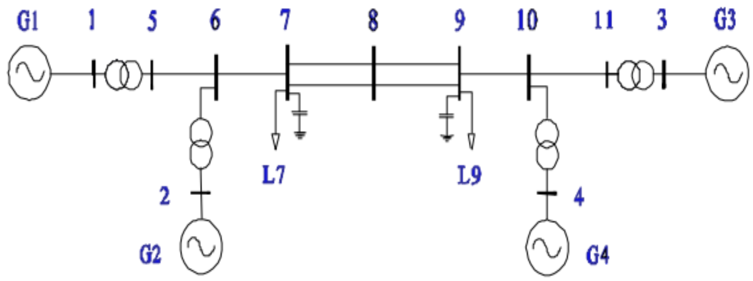

Figure 2-16 Two-area-four-machine system.

2.4.1 Case I. Variation in DC-link Capacitance

The first simulation study was carried out for variation of dc-link capacitance of CMI-based STATCOM. By changing the dc-link short-term energy storage of the STATCOM, a series of IFR from VIC based system can be obtained. ΔV_{dc}=0.3 pu. The rest of the parameters are in accordance with Table 2.1. This is compared with SC with H=1.25 s. The disturbances include load increase and load decrease, respectively. Simulation results are shown in Figure 2-17 and Figure 2-18.

As can be seen from Figure 2-17 and Figure 2-18, with the VIC based STATCOM, the ROCOF of SG is damped, this will largely improve the system stability. Since very limited frequency deviation, SC released very limited energy for the IFR and STATCOM perform better during this period of time.

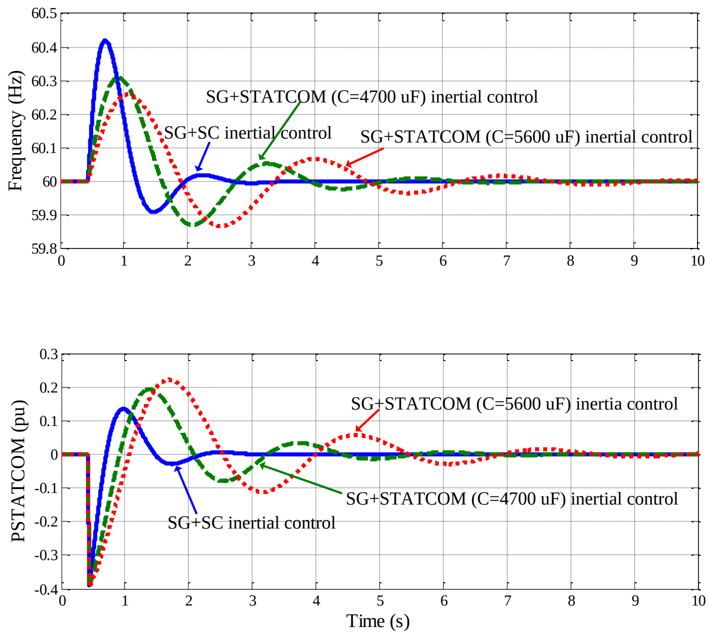

Figure 2-17 System response for 10% loadshed.

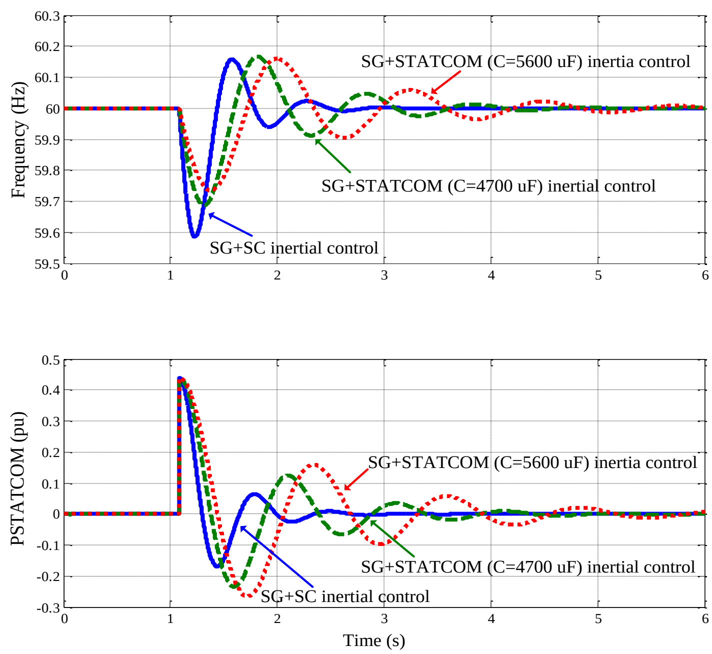

Figure 2-18 System response for 10% load increase.

2.4.2 Case II. Variation in Allowable DC-link Voltage

The second simulation study was carried out for variation of allowable dc-link voltage of CMI-based STATCOM. By changing the depth of voltage variation, a series of IFR from VIC based system is illustrated. C_{dc}=4700 μF. The rest of the parameters are in accordance to Table 2.1. This is compared with SC with H=1.25 s. Simulation result is shown in Figure 2-19.

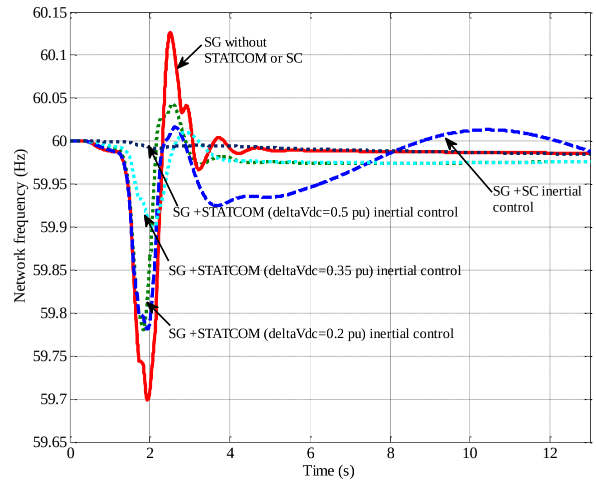

Figure 2-19 Simulation results for different conditions as of inertial energy response.

Like mentioned previously, the different inertia values of STATCOM can be obtained by varying capacitance value and dc-link voltage. From a practical point of view, once the STATCOM is installed there, its capacitance cannot be varied easily. So variation of dc-link voltage makes more practical sense. As can be seen from the simulation results, the generator without STATCOM or SC will suffer from a high oscillation and the lowest frequency can be 59.7 Hz. With the help of inertial energy from SC, the system operation will be better, although not as good as the STATCOM inertial control. Since it is locked by the system frequency to make synchronized with the system. For the STATCOM to provide this inertial energy, as we allow more deviation for DC link voltage, the frequency deviation will become smaller thus will benefit the system stability and reliability.

2.4.3 Wind Turbine Frequency Response

The system illustration is the same as shown in Figure 2-16. Two DFIGs with an inertial constant of 3.5 s is implemented, replacing the conventional SG in the system setup. The tested CMI-based STATCOM is connected to load bus at L7 and L9 for system dynamic performance. The comparison is made between virtual inertia control (VIC) and synthetic inertial control (SIC).

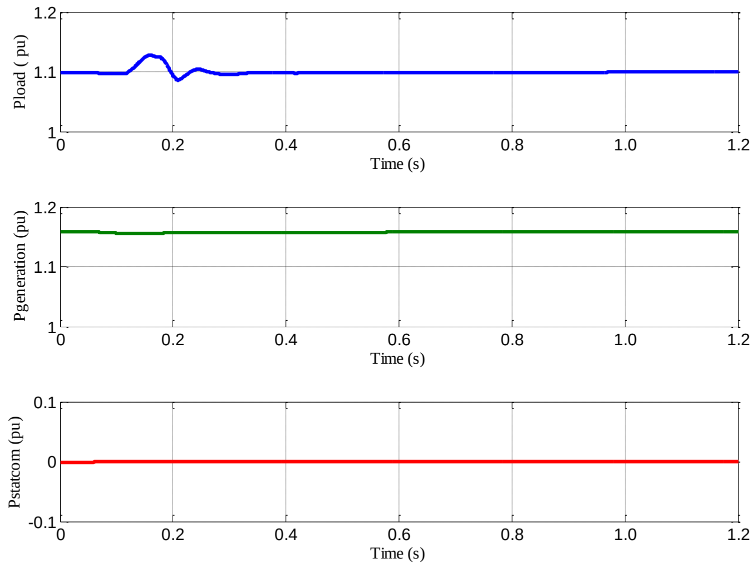

Figure 2-20 System response without VIC and SIC control.

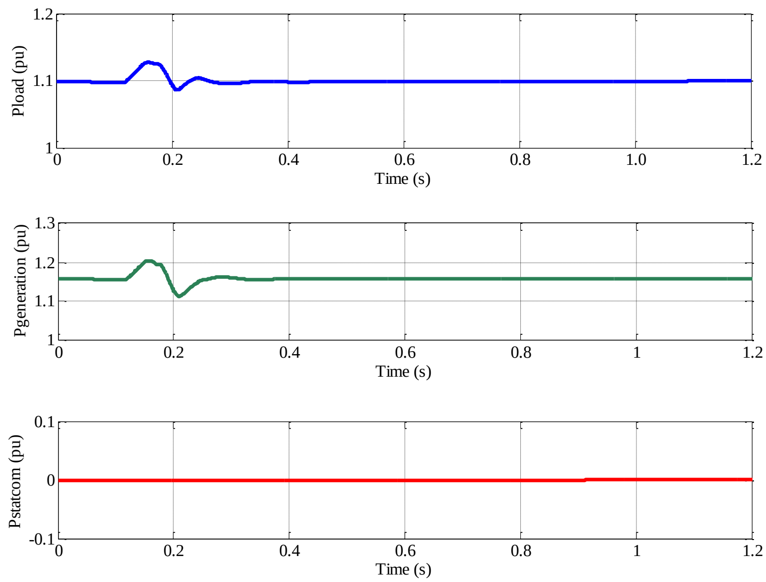

Figure 2-21 System response with SIC control.

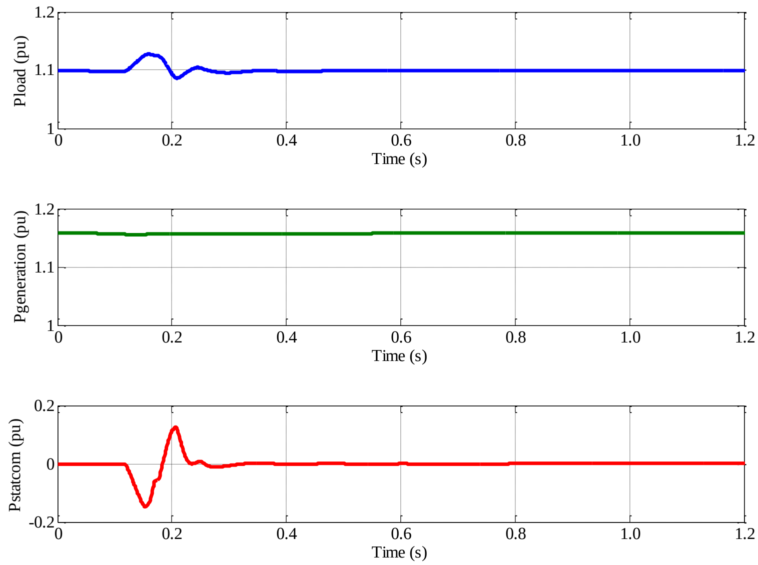

Figure 2-22 System response with VIC control.

As can be seen from the simulation results, system response without any control, with SIC control and VIC control have been demonstrated in Figure 2-20 to Figure 2-22. When there is load disturbance in the system, if the system is operated without any active control, the generation from the wind generator would not change since it is independent of the system disturbance and driven only under its own MPPT algorithm. When the SIC control is implemented, WP generator would change its output power accordingly to the load disturbance whereas the active power from the STATCOM is almost zero since its function is only to maintain the connected load bus, where only the reactive power exchange with the grid. Finally, while the system driven by the VIC control, the WP generator will still operate under its MPPT algorithm and STATACOM will be driven by the VIC strategy. Their comparative frequency variation has been demonstrated in Figure 2-23. The generator without any supplementary control will suffer from a high oscillation. With the help of SIC from rotating mass, the system operation will be improved, and STATCOM's VIC control has similar impact.

Furthermore, Figure 2-24 shows system frequency response under different wind speed. As can be seen from the simulated waveform, when the wind speed reduces, the synthetic inertia control is weakened or even deactivated.

Like mentioned previously, the different inertia values of STATCOM can be obtained by varying capacitance value and dc-link voltage. From a practical point of view, once the STATCOM is installed there, its capacitance cannot be varied easily. So variation of dc-link voltage makes more practical sense. As can be seen from the simulation results in Figure 2-25, the wind-turbine generator without VIC or SIC control will suffer from a high oscillation and the nadir point can be 59.7 Hz. With the help of inertial energy from SIC control, the system operation will be better, although not as good as the STATCOM based VIC control, since it is restricted by the wind speed in real application. For the STATCOM to provide this inertial energy, as we allow more deviation for dc link voltage or allow a larger dc link capacitance, the frequency deviation will become smaller thus will benefit the system stability and reliability.

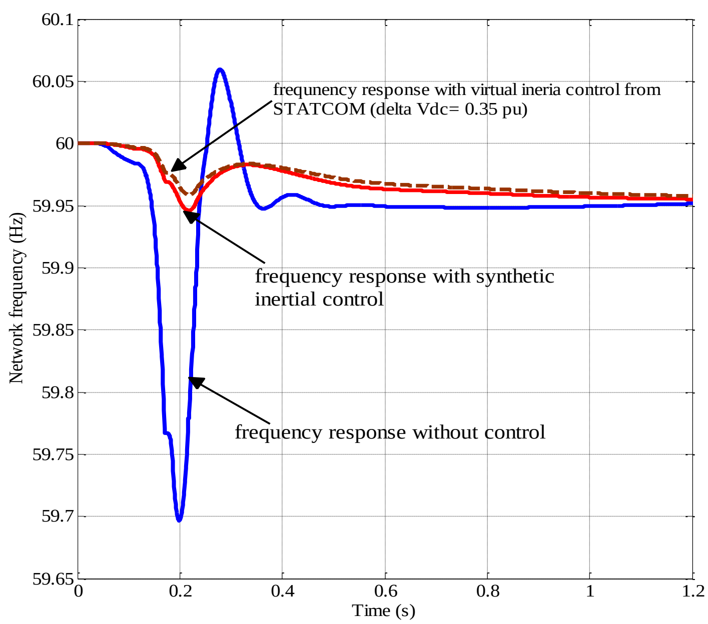

Figure 2-23 Network frequency response with different control.

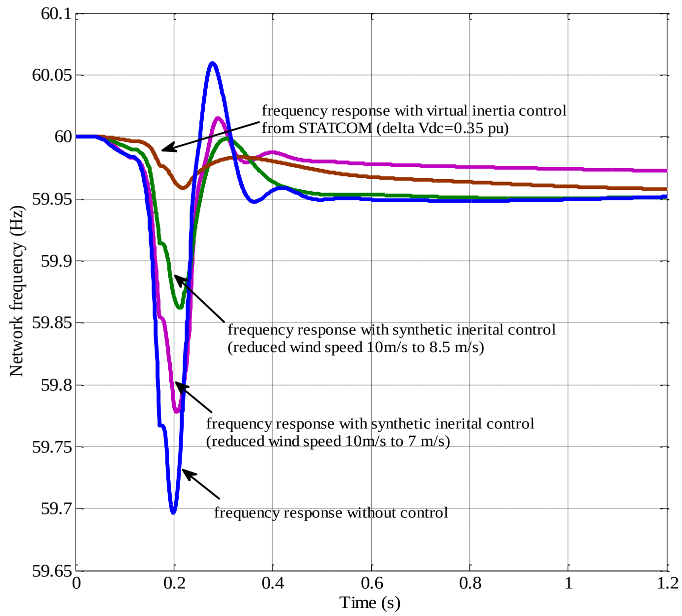

Figure 2-24 Network frequency response with different wind speed.

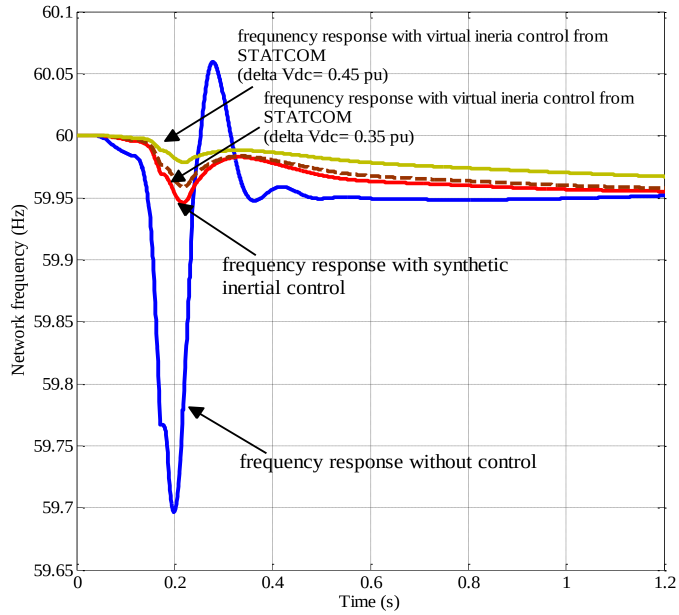

Figure 2-25 Network frequency response with different voltage variation.

2.5 Conclusion

A virtual inertial control for the CMI-based STATCOM is introduced in this chapter. Its contribution to inertial frequency response has been compared with SC. With the modified virtual inertia control of the DC link voltage, STATCOM can provide competitive inertial energy response as SC or provide even better response. Since this electric inertia is not limited by the system frequency rather its own dc link capacitance (short term energy storage) and dc link voltage variation, it is attractive to system study of STATCOM.

A virtual inertial control for the CMI-based STATCOM in wind-power generator application is introduced in this chapter. Its contribution to inertial frequency response has been compared with the SIC based rotating mass inertia control. With modifying the dc link voltage control strategy, STATCOM can provide competitive inertial energy response as SIC control. Since this electric inertia is not limited by the system frequency or generator atmosphere conditions (wind speed for wind application or irradiance in PV application) rather its own dc link capacitance (short term energy storage) and dc link voltage variation.

CHAPTER 3 Modulation and Control of Transformer-less UPFC

In this chapter, a modulation and control method for the new transformer-less unified power flow controller (UPFC) is presented. As is well known, the conventional UPFC that consists of two back-to-back inverters requires bulky and often complicated zigzag transformers for isolation and reaching high power rating with desired voltage waveforms. To overcome this problem, a completely transformer-less UPFC based on an innovative configuration of two cascade multilevel inverters (CMIs) has been proposed. The new UPFC offers several advantages over the traditional technology, such as transformer-less, light weight, high efficiency, low cost and fast dynamic response. This chapter focuses on the modulation and control for this new transformer-less UPFC, including optimized fundamental frequency modulation (FFM) for low total harmonic distortion (THD) and high efficiency, independent active and reactive power control over the transmission line, dc-link voltage balance control, etc. The new UPFC with proposed control method is verified by experiments based on 4160-V test setup. Both the steady-state and dynamic-response results will be shown in this chapter.

3.1 Introduction

The unified power flow controller (UPFC) is able to control, simultaneously or selectively, all the parameters affecting power flow in the transmission line (i.e., voltage magnitude, impedance, and phase angle) [11, 48, 49]. The conventional UPFC consists of two back-to-back connected voltage source inverters (VSIs) that share a common dc link, as shown in Figure 3-1. The injected series voltage from Inverter-2 can be at any angle with respect to the line current, which provides complete flexibility and controllability to control both active and reactive power flows over the transmission line. The resultant real power at the terminals of Inverter-2 is provided or absorbed by Inverter-1 through the common dc link. As a result, UPFC is the most versatile and powerful flexible ac transmission systems (FACTS) device. It can effectively reduce congestions and increase the capacity of existing transmission lines. This allows the overall system to operate at its theoretical maximum capacity. The basic control methods, transient analysis, and practical operation considerations for UPFC have been investigated in [50-56].

The conventional UPFC has been put into several practical applications [57-59], which has the following features: 1) both inverters share the same dc link; 2) both inverters need to exchange real power with each other and the transmission line; 3) a transformer must be used as an interface between the transmission line and each inverter. In addition, any utility-scale UPFC requires two high-voltage, high-power (from several MVA to hundreds of MVA) inverters. This high-voltage, high-power inverters have to use bulky and complicated zigzag transformers to reach their required VA ratings and desired voltage waveforms. The zigzag transformers are: 1) very expensive (30-40% of total system cost); 2) lossy (50% of the total power losses); 3) bulky (40% of system real estate area and 90% of the system weight); and 4) prone to failure [60]. Moreover, the zigzag transformer-based UPFCs are still too slow in dynamic response due to large time constant of magnetizing inductance over resistance and pose control challenges because of transformer saturation, magnetizing current, and voltage surge [61].

Recently, there are two new UPFC structures under investigation: 1) the matrix converter-based UPFC [62-64] and 2) distributed power-flow controller (DPFC) [65] derived from the conventional UPFC. The first one uses the matrix converter replacing the back-to-back inverter to eliminate the dc capacitor with ac capacitor on one side of the matrix converter. The DPFC employs many distributed series inverters coupled to the transmission line through single-turn transformers, and the common dc link between the shunt and series inverters is eliminated. The single-turn transformers lose one design freedom, thus making them even bulkier than a conventional transformer given a same VA rating. In summary, both UPFCs still have to use the transformers, which inevitably cause the same aforementioned problems associated with transformers (such as bulky, lossy, high cost, and slow in response).

The cascade multilevel inverter (CMI) is the only practical inverter technology to reach high-voltage levels without the use of transformers, a large number of semiconductor devices (diodes), or a large number of capacitors [14, 17, 60, 66]. The CMI-based STATCOMs (up to ±200 Mvar) have been installed in Europe and Asia [19, 32, 67, 68]. However, the CMI could not be directly used in the conventional UPFC, because the conventional UPFC requires two inverters connected back-to-back to deal with active power exchange. To address this problem, a UPFC with two face-to-face connected CMIs was developed in [16] to eliminate the zigzag transformers that are needed in the conventional multi-pulse inverter-based UPFC. However, it still required an isolation transformer.

To eliminate the transformer completely, a new transformer-less UPFC based on an innovative configuration of two CMIs has been proposed in [35]. The system configuration is shown in Figure 3-2 (a). As shown in Figure 3-2 (a), the transformer-less UPFC consists of two CMIs, one is series CMI, which is directly connected in series with the transmission line; while the other is shunt CMI, which is connected in parallel to the sending end after series CMI. Each CMI is composed of a series of cascaded H-bridge modules as shown in Figure 3-2 (b). The transformer-less UPFC has significant advantages over the traditional UPFC such as highly modular structure, light weight, high efficiency, high reliability, low cost, and a fast dynamic response. The basic operation principle, operation range, and required VA rating for series and shunt CMIs have been studied in [35]. Nevertheless, there are still challenges for the modulation and control of this new UPFC: 1) UPFC power flow control, such as voltage regulation, line impedance compensation, phase shifting or simultaneous control of voltage, impedance, and phase angle, thus achieving independently control both the active and reactive power flow in the line; 2) dc capacitor voltage balance control for H-bridges of both series and shunt CMIs; 3) modulation of the CMI for low total harmonic distortion (THD) of output voltage and low switching loss; 4) fast system dynamic response. This chapter presents the modulation and control for the new transformer-less UPFC to address aforementioned challenges. The UPFC functionality with proposed control method is verified at low voltage level (4,160 V), and both the steady-state and dynamic responses results will be shown in this chapter.

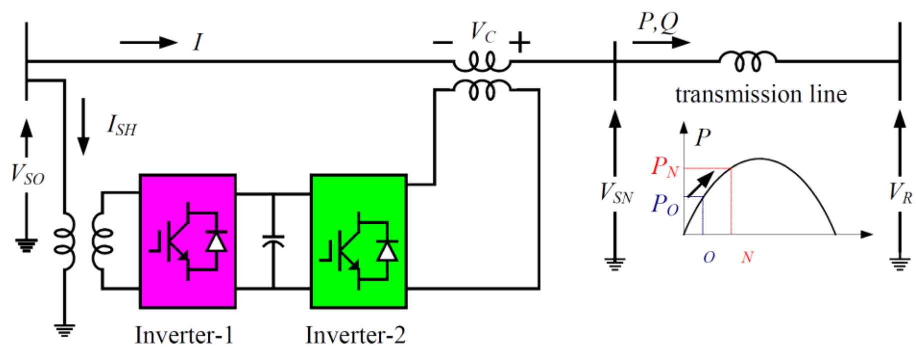

Figure 3-1 The conventional unified power flow controller.

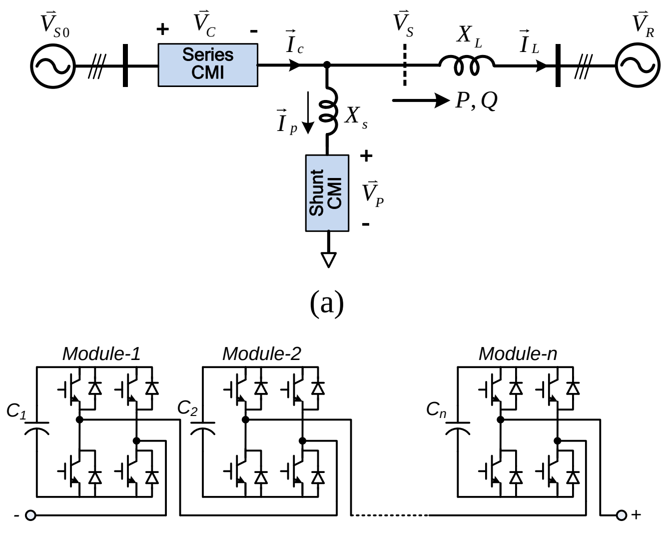

(a)

(b)

Figure 3-2 New transformer-less UFPC, (a) System Configuration of Transformer-less UPFC , (b) One phase of the cascaded multilevel inverter.

3.2 Operation Principle of the Transformer-less UPFC

With the unique configuration of the series and shunt CMIs, the transformer-less UPFC has some new features:

1) Unlike the conventional back-to-back dc link coupling, the transformer-less UPFC requires no transformer, thus it can achieve low cost, light weight, small size, high efficiency, high reliability, and fast dynamic response;

2) The shunt inverter is connected after the series inverter, which is distinctively different from the traditional UPFC. Each CMI has its own dc capacitor to support dc voltage;

3) There is no active power exchange between the two CMIs and all dc capacitors are floating;

4) The new UPFC uses modular CMIs and their inherent redundancy provides greater flexibility and higher reliability.

Due to the unique system configuration, the basic operation principle of the transformer-less UPFC is quite different from conventional UPFC. Figure 3-3 shows the phasor diagram of the transformer-less UPFC, where $\vec{V}_{S0}$ and $\vec{V}_R$ are the original sending-end and receiving-end voltage, respectively. Here, $\vec{V}_{S0}$ is aligned with real axis, which means phase angle of $\vec{V}_{S0}$ is zero. The series CMI is controlled to generate a desired voltage $\vec{V}_C$ for obtaining the new sending-end voltage $\vec{V}_S$, which in turn, controls active and reactive power flows over the transmission line. Meanwhile, the shunt CMI injects a current $\vec{I}_P$ to the new sending-end bus to make zero active power into both CMIs, i.e., to make the series CMI current $\vec{I}_C$ and the shunt CMI current $\vec{I}_P$ be perpendicular to their voltages $\vec{V}_C$ and $\vec{V}_S$, respectively. As a result, both series and shunt CMIs only need to provide the reactive power. In such a way, it is possible to apply the CMIs to the transformer-less UPFC with floating dc capacitors for H-bridge modules.

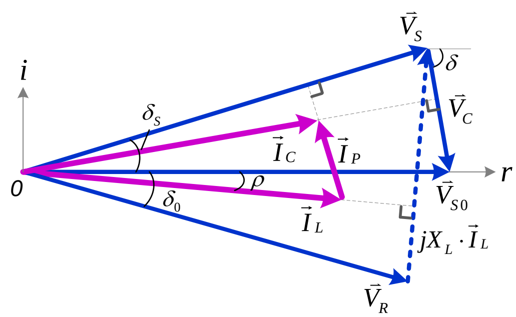

Figure 3-3 Phasor diagram of the transformer-less UPFC.

The detailed operating principle of the transformer-less UPFC can be formulated as follows. With referring to Figure 3-2 and Figure 3-3, the transmitted active power P and reactive power Q over the line with the transformer-less UPFC can be expressed as

$$
\begin{aligned}
P + jQ &= \vec{V}_R \cdot \left(\frac{\vec{V}_{S0} - \vec{V}_C - \vec{V}_R}{jX_L} \right)^* \\
&= \left(-\frac{V_{S0}V_R}{X_L}\sin\delta_0 + \frac{V_C V_R}{X_L}\sin(\delta_0 - \delta) \right) + \\
& j\left(\frac{V_{S0}V_R\cos\delta_0 - V_R^2}{X_L} - \frac{V_C V_R}{X_L}\cos(\delta_0 - \delta) \right)
\end{aligned}
\qquad (3.1),
$$

where symbol * represents the conjugate of a complex number; δ_0 is the phase angle of the receiving-end voltage $\vec{V}_R$; δ is the phase angle of the series CMI injected voltage $\vec{V}_C$; X_L is the equivalent transmission line impedance. The original active and reactive powers, P_0 and Q_0 with the uncompensated system (without the UPFC, or V_C=0) are

$$
\begin{cases}
P_0 = -\dfrac{V_{S0}V_R}{X_L}\sin\delta_0 \\
Q_0 = \dfrac{V_{S0}V_R\cos\delta_0 - V_R^2}{X_L} \quad .
\end{cases}
\qquad (3.2).
$$

The net differences between the original (without the UPFC) powers expressed in equation (3.2) and the new (with the UPFC) powers in equation (3.1) are the controllable active and reactive powers, P_C and Q_C by the transformer-less UPFC, which can be expressed as

$$
\begin{cases}
P_C = \dfrac{V_C V_R}{X_L}\sin(\delta_0 - \delta) \\
Q_C = -\dfrac{V_C V_R}{X_L}\cos(\delta_0 - \delta) .
\end{cases}
\qquad (3.3).
$$

Therefore, we can rewrite equation (3.1) as

$$
P + jQ = \left(\underbrace{-\frac{V_{S0}V_R}{X_L}\sin\delta_0}_{P_0} + \underbrace{\frac{V_C V_R}{X_L}\sin(\delta_0 - \delta)}_{P_C} \right) + j\left(\underbrace{\frac{V_{S0}V_R\cos\delta_0 - V_R^2}{X_L}}_{Q_0} \underbrace{-\frac{V_C V_{Rc}}{X_L}\cos(\delta_0 - \delta)}_{Q_C} \right) \quad . \qquad (3.4).
$$

Because both amplitude V_C and phase angle δ of the UPFC injected voltage $\vec{V}_C$ can be any values as commanded, the new UPFC provides a full controllable range of $\left(-V_C V_R / X_L\right)$ to

$\left(+V_C V_R / X_L\right)$ for both active and reactive powers, P_C and Q_C, which are advantageously independent of the original sending-end voltage and phase angle δ_0. In summary, equations (3.1) to (3.4) indicate that the new transformer-less UPFC has the same functionality as the conventional UPFC.

Firstly, the series CMI voltage $\vec{V}_C$ is injected according to transmission line active/reactive power command, which can be calculated from (3.3)

$$\vec{V}_C = V_C \angle \delta = \frac{X_L}{V_R}\sqrt{P_C^2 + Q_C^2}\,\angle(\delta_0 - \arctan(\frac{P_C}{Q_C})) \quad (3.5).$$

Once the series CMI injected voltage $\vec{V}_C$ is decided by (3.5), the new sending-end voltage $\vec{V}_S$ and the transmission line current will be decided accordingly.

$$\vec{V}_S = V_S \angle \delta_S = \vec{V}_{s0} - \vec{V}_C \quad (3.6),$$

where

$$\begin{cases} V_S = \sqrt{\left(V_{S0} - V_C\cos\delta\right)^2 + \left(V_C \sin\delta\right)^2} \\ \delta_S = \arctan\left(\dfrac{-V_C\sin\delta}{V_{S0} - V_C\cos\delta}\right) \end{cases} \quad (3.7),$$

and $\vec{I}_L = I_L \angle \rho$, where

$$\begin{cases} I_L = \dfrac{\sqrt{\left(V_C\sin\delta + V_R\sin\delta_0\right)^2 + \left(V_{S0} - V_C\cos\delta - V_R\cos\delta_0\right)^2}}{X_L} \\ \rho = \arctan\left(\dfrac{V_{S0} - V_C\cos\delta - V_R\cos\delta_0}{V_C\sin\delta + V_R\sin\delta_0}\right) \end{cases} \quad (3.8).$$

Next, the shunt CMI injects current $\vec{I}_P$ to decouple the series CMI current $\vec{I}_C$ from the line current $\vec{I}_L$. In such a way, zero active power exchange to both series and shunt CMIs can be achieved, making it possible to apply the CMI with floating capacitors to the proposed transformer-less UPFC. Therefore, we have

$$\begin{cases} P_{se} = \vec{V}_C \cdot \vec{I}_C = 0 \\ P_{sh} = \vec{V}_S \cdot \vec{I}_P = 0 \end{cases} \tag{3.9}$$

It means the series CMI current $\vec{I}_C$ and the shunt CMI current $\vec{I}_P$ need to be perpendicular to their voltages $\vec{V}_C$ and $\vec{V}_S$, respectively, as illustrated in Figure 3-3. With the geometrical relationship of the voltages and currents in Figure 3-3, the shunt CMI output current can be calculated as

$$\vec{I}_P = I_P \angle \theta_{Ip} \tag{3.10}$$

where

$$\begin{cases} I_P = I_L \left(\dfrac{\cos(\rho - \delta_S)}{\tan(\delta - \delta_s)} - \sin(\rho - \delta_S) \right) \\ \theta_{Ip} = 90 + \delta_S \end{cases} . \tag{3.11}$$

In summary, there are two critical steps for the operation of UPFC: a) calculation of injected voltage $\vec{V}_C$ for series CMI according to active/reactive power command over the transmission line expressed in (3.5), and b) calculation of injected current $\vec{I}_P$ for shunt CMI from (3.10) and (3.11) to guarantee zero active power into both series and shunt CMIs.

3.3 Fundamental Frequency Modulation for CMIs

Before embarking on development of UPFC control, the modulation strategy for CMIs is introduced first. In general, the modulation for CMIs can be classed into two main categories: 1) fundamental frequency modulation (FFM) [14, 16, 17, 66, 67, 69] and 2) high-frequency pulse width modulation (PWM) [18, 19, 70-73]. Compared to the high-frequency PWM, the FFM has much lower switching loss, making it attractive for the transmission-level UPFC and other high-voltage high-power applications. Furthermore, it will also demonstrate that CMIs with FFM can also achieve fast dynamic response, e.g. 8 ms. Compared to carrier based high-frequency PWM scheme, the CMIs with FFM have the following features:

1. FFM has much lower switching loss, thus higher efficiency;
2. With high number of H-bridge modules, output voltage could be very close to sinusoidal, and extremely low THD (e.g. 0.85%) could be achieved without any extra filters;
3. It is notable that FFM does not actually mean slow dynamic response. With high-frequency sampling, FFM can also achieve fast dynamic response, e.g. < 10 ms, which will be discussed and experimentally verified in next section.

3.4 Power Flow and Dc-link Voltage Control of Transformer-less UPFC

3.4.1 Dynamic Models of UPFC System

The equations derived from the phasor diagram in section II are limited to steady-state operation analysis. In order to design the vector oriented control (VOC) for the proposed transformer-less UPFC with considering both steady-state and dynamic performance, the dynamic modules are necessary. The models are based on synchronous (dq) reference frame. The phase angle of original sending-end voltage V_{s0} is obtained from a digital phase-locked loop (PLL), which is used for abc to dq transformation.

The dynamic models for the whole system shown in Figure 3-2 (a) will be divided into several parts. Firstly, we can get the dynamic model from the new sending-end bus to sending-end bus

$$\begin{cases} V_{sd} = R_L\, i_{Ld} + L_L \dfrac{di_{Ld}}{dt} - \omega L_L i_{Lq} + V_{Rd} \\ V_{sq} = R_L\, i_{Lq} + L_L \dfrac{di_{Lq}}{dt} + \omega L_L i_{Ld} + V_{Rq} \end{cases} \tag{3.12}$$

Since the new sending-end voltage V_s is equal to original sending-end voltage V_{s0} minus series CMI injected voltage V_c, thus we have

$$\begin{cases} V_{Cd} = V_{S0d} - V_{Sd} \\ V_{Cq} = V_{S0q} - V_{Sq} \end{cases} \tag{3.13}$$

Furthermore, the model from the new sending-end to shunt CMI is

$$\begin{cases} V_{sd} = R_s\, i_{Pd} + L_s \dfrac{di_{Pd}}{dt} - \omega L_s i_{Pq} + V_{pd} \\ V_{sq} = R_s\, i_{Pq} + L_s \dfrac{di_{Pq}}{dt} + \omega L_s i_{Pd} + V_{pq} \end{cases} \tag{3.14}$$

3.4.2 Power Flow and DC-link Voltage Control

It's desired to design a control system, which can independently regulate the active power P and reactive power Q in the line, at the same time, maintain the capacitor voltages of both CMIs at the given value. Figure 3-4 (a) shows the overall control system, which is divided into three stages, i.e. stage I to stage III.

Stage I: the calculation from P^*/Q^* to $\overrightarrow{V_{C0}^*}$ and $\overrightarrow{I_{p0}^*}$. As mentioned before, the $\overrightarrow{V_{C0}^*}$ is the voltage reference for series CMI, which is generated according to the transmission line power command as given in (3.5), while $\overrightarrow{I_{p0}^*}$ is current reference for shunt CMI, which is used to keep zero active power for both CMIs as given in (3.10), (3.11). Note that instead of calculating $\overrightarrow{V_{C0}^*}$ directly from (3.5), an alternative way is shown in Figure 3-4 (b). Here, the line current reference

I_{Ld}^{*}/I_{Lq}^{*} is calculated out of the P^{*}/Q^{*} reference, then V_{C0d}^{*}/V_{C0q}^{*} is calculated according to (3.15), where the dynamic model of (3.12) is included. The line current is controlled in a way of decoupling feedforward control, thus better line current dynamic response could be achieved.

Stage II: overall dc-link voltage regulation. With the $\overrightarrow{V_{C0}^{*}}$ and $\overrightarrow{I_{p0}^{*}}$ given in stage I, the dc-link voltage can't be maintained due to the following three main reasons: (a) the CMIs always have a power loss, (b) the calculation error caused by the parameter deviations, (c) the error between reference and actual output. In order to control dc-link voltage with better robustness, two variables $\overrightarrow{\Delta V_C}$ and $\overrightarrow{\Delta I_P}$ were introduced for the independent dc-link voltage regulation of series CMI and shunt CMI, respectively, as shown in Figure 3-4 (a). In this figure, $V_{dc\_sh}^{*}$ and $V_{dc\_se}^{*}$ are dc voltage references for shunt and series CMIs, respectively; V_{dc_sh} and V_{dc_se} are the averaged dc feedback of series and shunt CMIs, respectively. For the series CMI, P_{se} is the output of overall dc-link voltage regulation loop, R_{se} is then calculated by dividing P_{se} by I_c^2 (square of rms value of series CMI current), finally $\overrightarrow{\Delta V_C}$ is the product of Rse and series CMI current $\overrightarrow{I_C}$. Obviously, the introduced $\overrightarrow{\Delta V_C}$ is always in phase with series CMI $\overrightarrow{I_C}$, which can be regarded as active voltage component. Basically, Rse is the equivalent resistance of series CMI, and the dc-link can be balanced when P_{se} is equal to P_{loss} (total power loss of series CMI). For the shunt CMI, $\overrightarrow{\Delta I_P}$ is introduced for the dc-link voltage control in a similar way.

The mathematical model and detailed parameters design for the overall dc voltage control can be found in reference. Usually, the cascade multilevel inverter should be considered as three single-phase inverters, therefore, the dc capacitor voltage will contain the 2ω (2 times of the fundamental frequency) component. To keep the average dc track the command without being affected by the 2ω ripple, the bandwidth of current control loop and dc voltage control loop is designed to be differential. For example, the current control loop has been designed to have fast dynamic response (e.g. half cycle, 8 ms), while dc voltage control loop has been designed to have much slower dynamic response (e.g. 10 cycles). In this way, the 2ω ripple can be suppressed in the voltage control loop.

Stage III: voltage and current generation for series and shunt CMI, respectively. For series CMI, output voltage could be directly generated from the reference $\vec{V}_C^*$ by FFM. While for shunt CMI, decoupling feedback current control is used to control output current to follow the reference current $\vec{I}_P^*$, as shown in Figure 3-4 (c) [17].

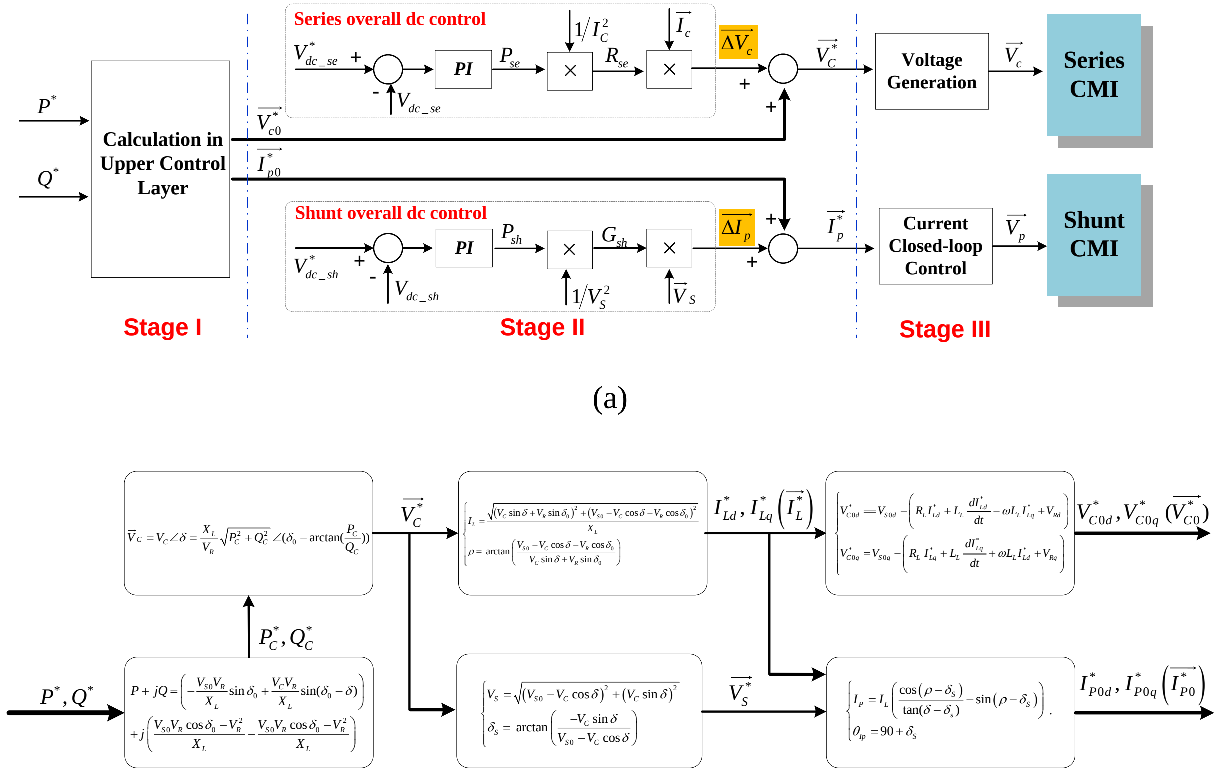

(a)

(b)

Figure 3-4 Control system for transformer-less UPFC, (a) overall control diagram for both power flow and dc capacitor voltage control, (b) detailed calculation from P^*/Q^* to V_{c0}^* and I_{p0}^*, (c) decoupling feedback current control for shunt CMI.

Figure 3-4 (cont'd)

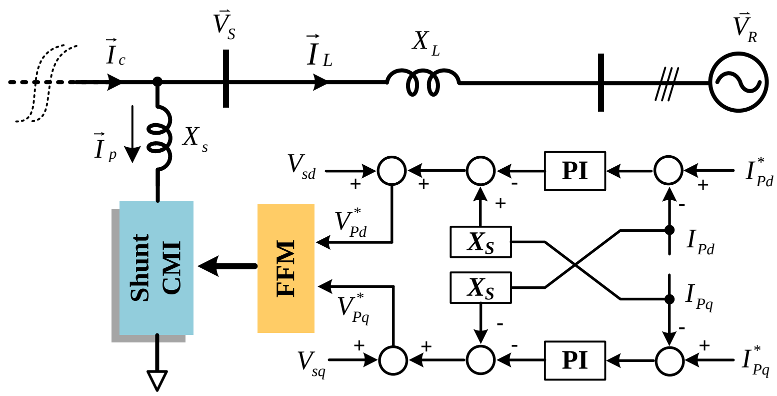

(c)

$$\begin{cases} V_{C0d}^{*} = V_{S0d} - V_{Sd}^{*} = V_{S0d} - \left(R_L I_{Ld}^{*} + L_L \dfrac{dI_{Ld}^{*}}{dt} - \omega L_L I_{Lq}^{*} + V_{Rd} \right) \\ V_{C0q}^{*} = V_{S0q} - V_{Sq}^{*} = V_{S0q} - \left(R_L I_{Lq}^{*} + L_L \dfrac{dI_{Lq}^{*}}{dt} + \omega L_L I_{Ld}^{*} + V_{Rq} \right) \end{cases} \tag{3.15}$$

3.5 Experimental Results

To validate the functionality of the transformer-less UPFC system with proposed modulation and control algorithm, a 4160 V test setup has been developed as shown in Figure 3-5 (a), and the main system parameters for this test setup are given in Table 3.1. Figure 3-5 (b) shows the corresponding equivalent circuit of this test setup, which is consistent with the circuit configuration shown in Figure 3-2 (a). In Figure 3-5 (b), the equivalent receiving-end voltage $\vec{V}_R$ has same amplitude as original sending-end voltage $\vec{V}_{S0}$, but 30° phase lagging. This 30° phase lagging is introduced by Transformer 2 with Y/Δ configuration (Y/Δ, 480 V/ 4160 V). The basic functions of the UPFC (i.e. voltage regulation, line impedance compensation, phase shifting and simultaneous control of voltage, impedance and angle) have been tested based on this setup. Some experimental results are given in this section.

Table 3.1. System Parameters for 4160 V Test Setup

Parameter	Value	Parameter	Value
Grid voltage (low voltage side) V_g	480 V	Dc capacitance of each H-bridge	2350 μF
Rated frequency	60 Hz	Rated line current	10 A
Sampling frequency	2.5 kHz	Reactor X_1	2.5 mH
V_{dc} command of each shunt H-bridge	600 V	Reactor X_2	3.2 mH
V_{dc} command of each series H-bridge	600 V	Leakage inductance of Transformer 1 (Δ/Δ)	35 mH (6% pu)
No. of H-bridges per phase (Shunt)	6	Leakage inductance of Transformer 2 (Y/Δ)	35 mH (6% pu)
No. of H-bridges per phase (Series)	3	Equivalent line inductance X_L	0.31 H (50% pu)
Transformer 1 (Δ/Δ)	480 V/ 4160 V, 75 kVA	Equivalent shunt filter inductance X_S	0.22 H (36% pu)
Transformer 2 (Y/Δ)	480 V/ 4160 V, 75 kVA, 30^0 lagging		

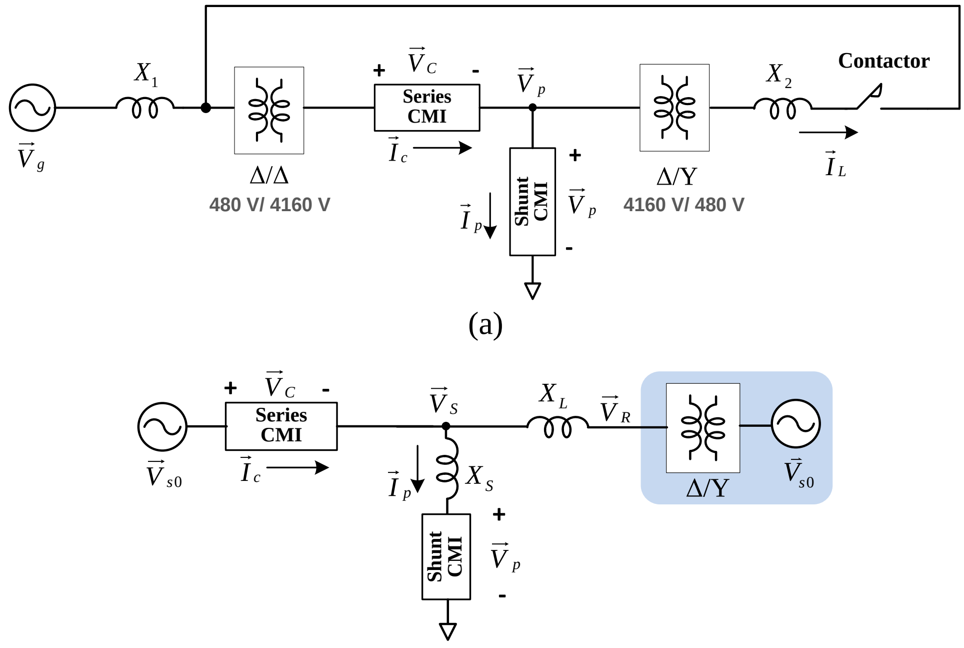

Figure 3-5 4160-V Transformer-less UPFC Test setup, (a) circuit configuration and (b) corresponding equivalent circuit.

3.5.1 UPFC Operation - Phase Shifting

The UPFC can function as a perfect phase angle regulator, which achieves the desired phase shift (leading or lagging) of the original sending-end voltage without any change in magnitude. Three operating points with different shifted phases are considered as shown in Figure 3-6, (a) case A1: 30°, (b) case A2: 15°, and (c) case A3: 0°. All three phase shifting cases (case A1 to case A3) have been tested and corresponding test results are shown in Figure 3-7-Figure 3-10. Some discussions about the test results are given as follows:

1) Figure 3-7 shows the experimental waveforms of UPFC operating from case A1 to case A2 (Phase shifting 30° to 15°). As mentioned before, in the test setup, there is already 30° phase difference between the original sending-end voltage $\vec{V}_{S0}$ and the receiving-end voltage $\vec{V}_R$. For case A1, series CMI voltage $\vec{V}_C$ is injected to shift $\vec{V}_{S0}$ by 30° lagging, as a result, $\vec{V}_S = \vec{V}_R$. In

this case, UPFC is used to compensate voltage difference caused by transformer 30° phase shift. Therefore, the resulting line current in this case is almost zero. While for case A2, new sending-end voltage $\vec{V}_S$ is shifted from $\vec{V}_{S0}$ by 15°, therefore, there is 15° phase difference between $\vec{V}_S$ and $\vec{V}_R$. This will result in about 7 A (peak value) line current. Figure 3-7 (a) and (b) show the experimental waveforms of shunt current I_{pa}, line current I_{La}, and shunt CMI output phase voltage V_{pa}, V_{pb}. The V_{pa} and V_{pb} are stair-case waveforms, which are generated by the FFM with optimized switching angles for low THD. Figure 3-7 (c) and (d) show the line voltage, which is very close to sinusoidal due to absence of the triplen harmonics in a balanced three-phase system. Furthermore, Figure 3-7 also shows that the current smoothly and quickly raised from zero to 7 A, when the operating point is changed from case A1 to A2.

2) Similarly, Figure 3-8 shows the experimental waveforms of UPFC operating from case A2 to case A3 (Phase shifting 15° to 0°). For case A3, phase shifting is zero degree, indicating a system without compensation. Therefore, $\vec{V}_S = \vec{V}_{S0}$, and the phase angle between $\vec{V}_S$ and $\vec{V}_R$ is 30°. The resulting current amplitude in this case is 14 A.

3) Figure 3-9 shows the measured dynamic response with operating point changing from case A2 to case A3, where the current amplitude would change from 7 A to 14 A. Since the system dynamic model has been included in the control algorithm as shown in Figure 3-4, the UPFC system has achieved fast dynamic response, with response time < 10 ms. This dynamic performance is good enough for transmission-level power flow control.

4) Figure 3-10 shows the experimental results of dc capacitor voltage of both series and shunt CMIs when operating from case A2 to case A3, where top three waveforms correspond to average dc voltage of each phase, and bottom one corresponds to average dc voltage of all three

phases. During the transition, the dc link voltage almost kept constant, which means the dc link voltage can be controlled to follow the reference faithfully regardless of operating points.

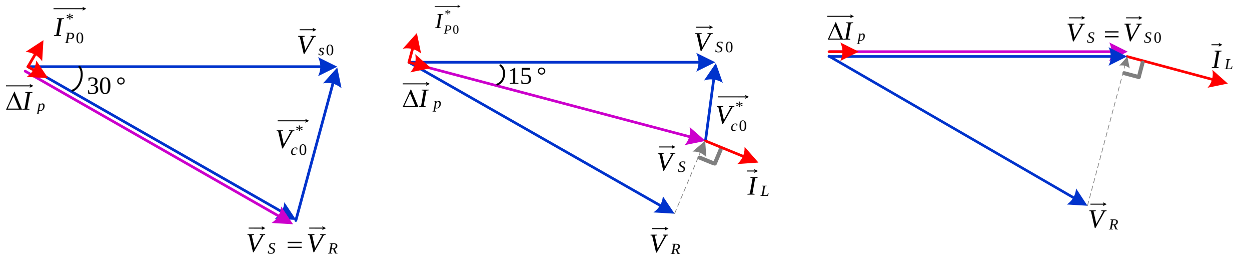

(a) (b) (c)

Figure 3-6 UPFC operating points with different phase shifting, (a) case A1: 30 °, (b) case A2: 15 °, and (c) case A3: 0 °.

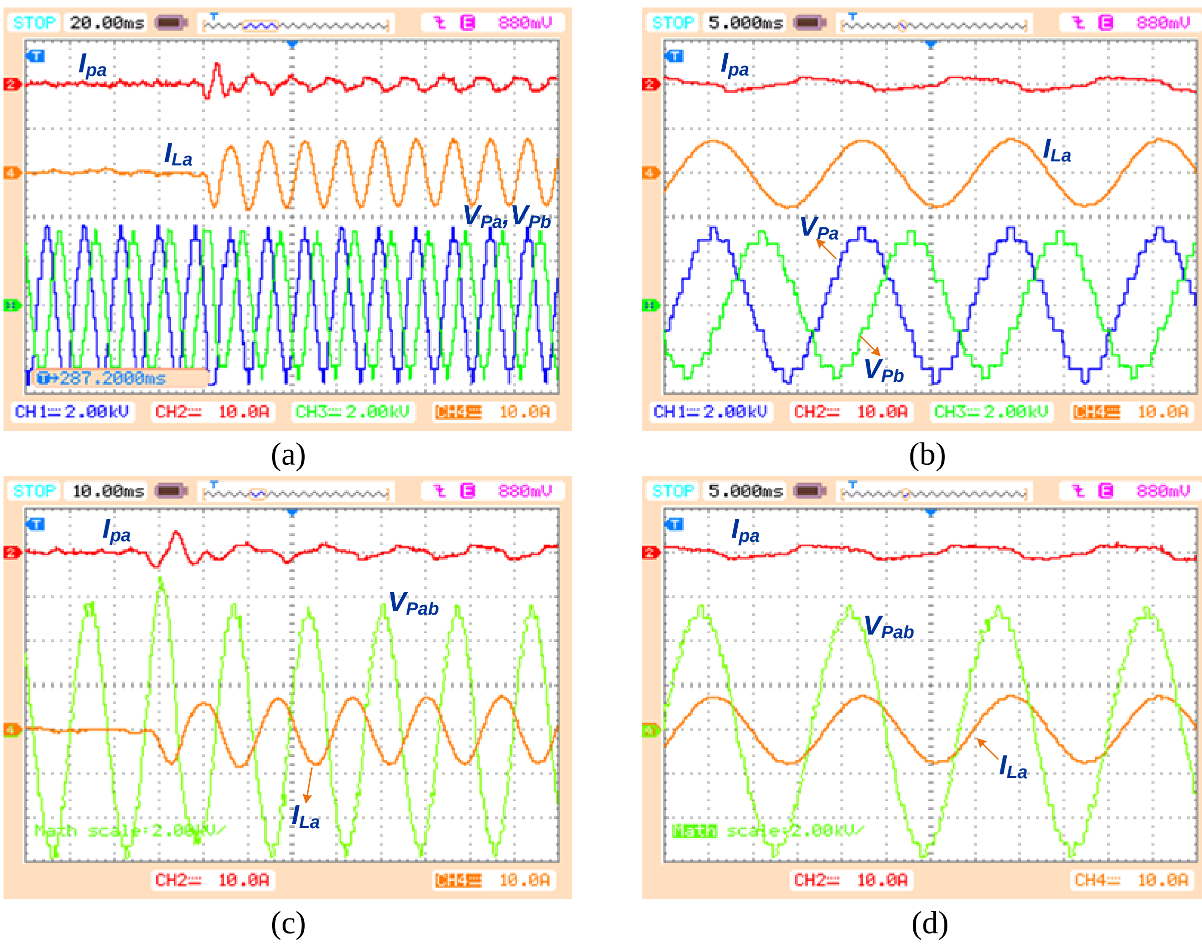

Figure 3-7 Experimental waveforms of UPFC operating from case A1 to case A2 (Phase shifting 30 °to 15 °), (a) and (b) shunt CMI phase voltage V_{Pa} and V_{Pb}, shunt CMI phase current I_{Pa}, and line current I_{La}, (c) and (d) shunt CMI line voltage V_{Pab}, shunt CMI phase c

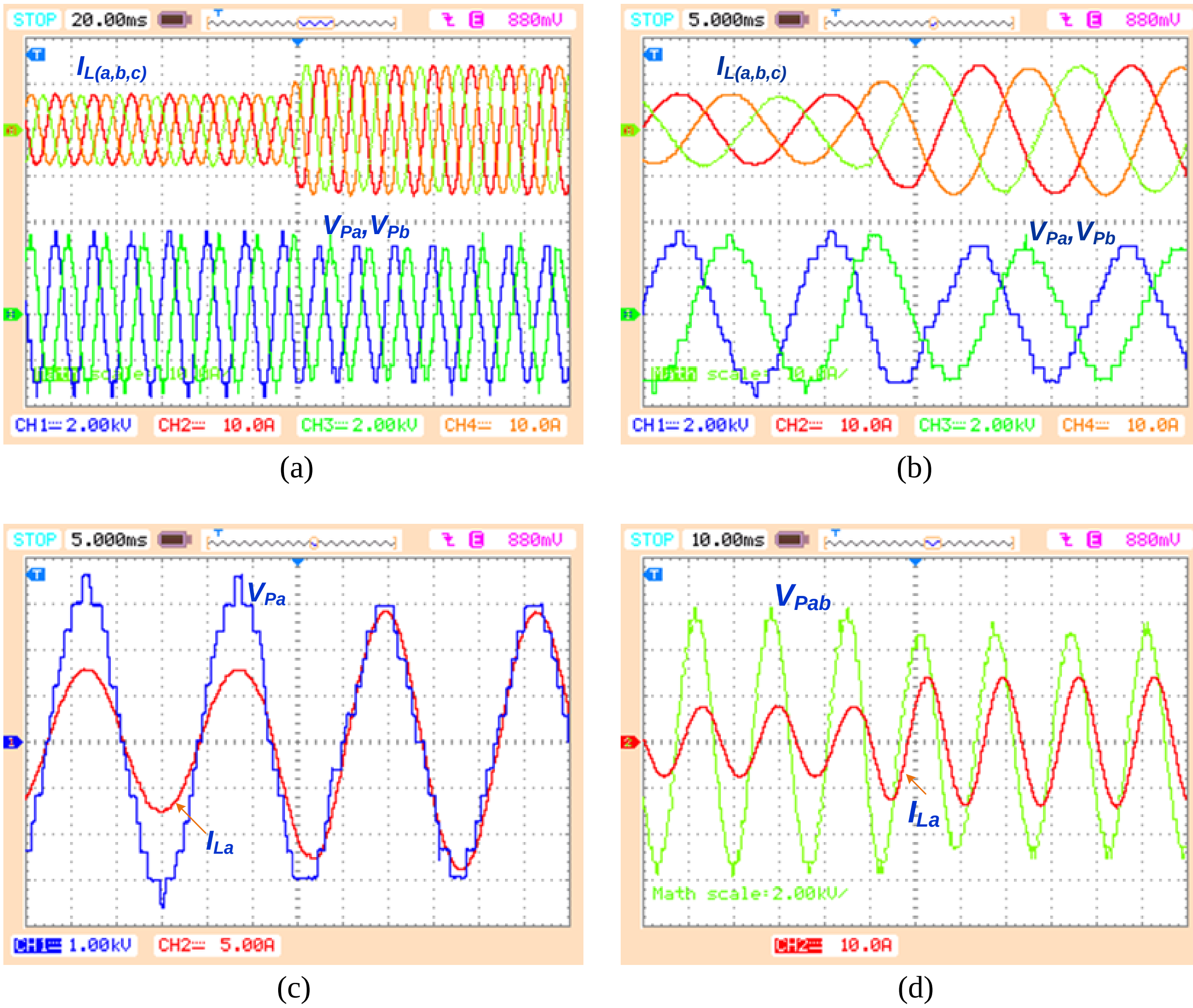

Figure 3-8 Experimental waveforms of UPFC operating from case A2 to case A3 (Phase shifting 15° to 0°), (a) and (b) shunt CMI V_{Pa}, V_{Pb} and I_{La}, I_{Lb}, I_{Lc}, (c) line current I_{La} and shunt CMI V_{Pa}, and (d) line current I_{La} and line voltage V_{pab}.

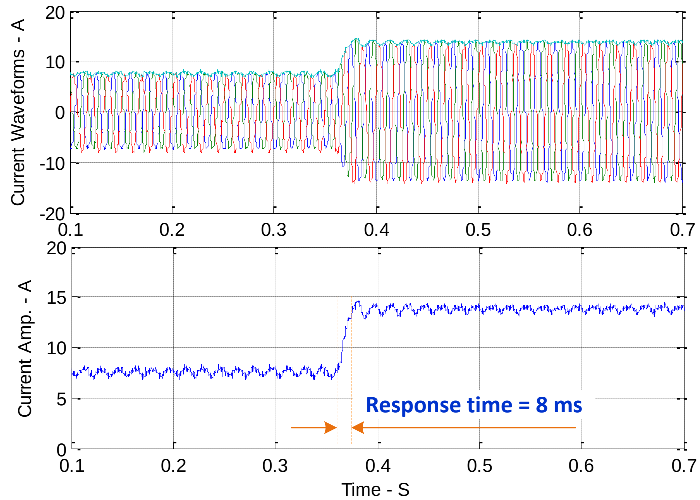

Figure 3-9 Measured dynamic response with operating point changing from case A2 to case A3 (Phase shifting 15 °to 0 °).

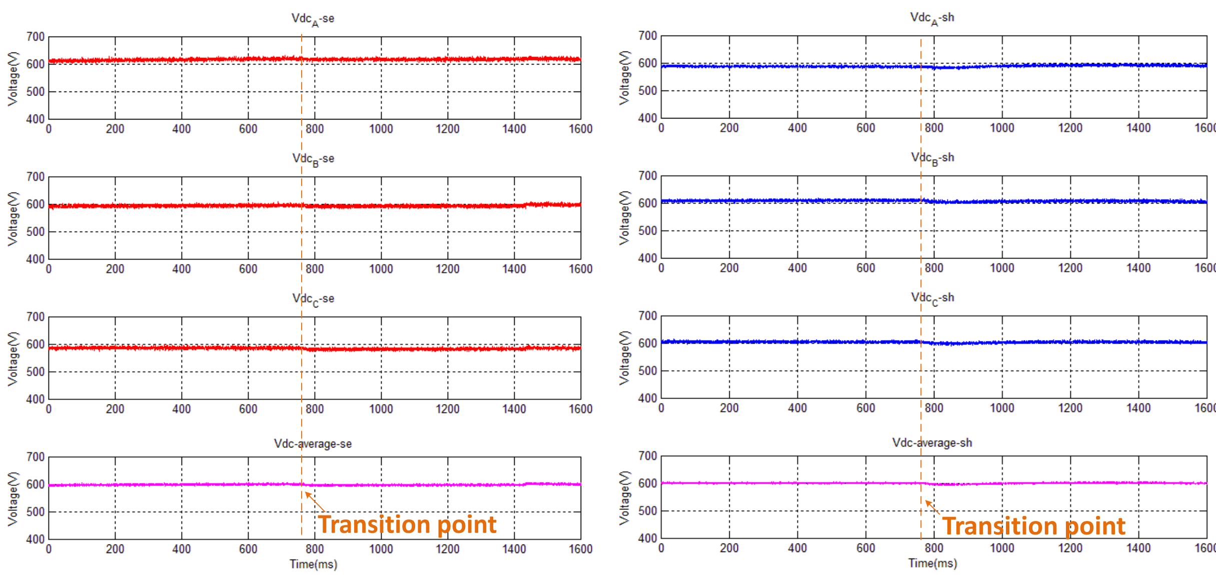

(a) (b)

Figure 3-10 Experimental results of dc capacitor voltage of series and shunt CMIs, from case A2 to case A3 (Phase shifting 15 °to 0 °), (a) dc capacitor voltage of series CMI, and (b) dc capacitor voltage of shunt CMI.

3.5.2 UPFC Operation - Line Impedance Compensation

UPFC function of line impedance compensation is different from phase shifting, where the series CMI voltage $\vec{V}_C$ is injected in quadrature with the line current. Functionally it's similar to series capacitive or inductive line compensation attained by static synchronous series compensator (SSSC). Figure 3-11 shows three operation points with line impedance compensation, (a) case B1: Original line impedance without compensation = 0.5 pu, (b) case B2: Equivalent line impedance after compensation = 1 pu, and (c) case B3: Equivalent line impedance after compensation = ∞. For case B1 (same as case A3), system without compensation has 0.5 pu voltage between $\vec{V}_S$ and $\vec{V}_R$ (corresponding to 30° voltage difference). With the line impedance= 0.31 H (0.5 *pu*) given in Table 3.1, the resulted line current is 1 *pu* (amplitude 14 A), which is the nominal current for transformer 1 and transformer 2 in the 4160 V test setup. Due to the current limitation of transformers, for case B2 and case B3, UPFC is purposely controlled to increase the line impedance. Nevertheless, the transformer-less UPFC is also able to reduce the line impedance for higher line current (or higher *P/Q*).

Figure 3-12 shows the experimental results of UPFC operation from case B1 to case B2, where the line impedance changed from original 0.5 pu without compensation to 1 pu after compensation. Figure 3-12 (a) and (b) shows the waveforms of shunt CMI phase voltage V_{Pa}, V_{Pb} and line current I_{La}, I_{Lb} and I_{Lc}, where the line current smoothly changed from 14 A to 7 A (peak value) due to the doubled line impedance. Figure 3-12 (c) shows the line current I_{La} and shunt CMI line voltage V_{Pab}. Furthermore, Figure 3-12 (d) shows the waveforms of the series CMI injected voltage V_{Ca} and line current I_{La}. From this figure, we can see the line current I_{La} is lagging V_{Ca} by 90°, which means the series CMIs act as inductors. This is the reason that, after compensation, the line impedance is increased from 0.5 pu to 1 pu. Figure 3-13 shows the dynamic response with operating point changing from case B1 to case B2. The measured response time is about 8 ms.

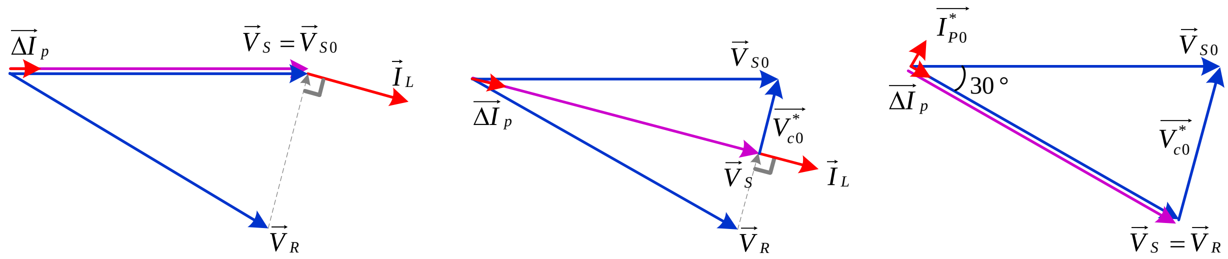

(a) (b) (c)

Figure 3-11 UPFC operating points with line impedance compensation, (a) case B1: Original line impedance without compensation = 0.5 pu, (b) case B2: Equivalent line impedance after compensation = 1 pu, and (c) case B3: Equivalent line impedance after compensation = ∞

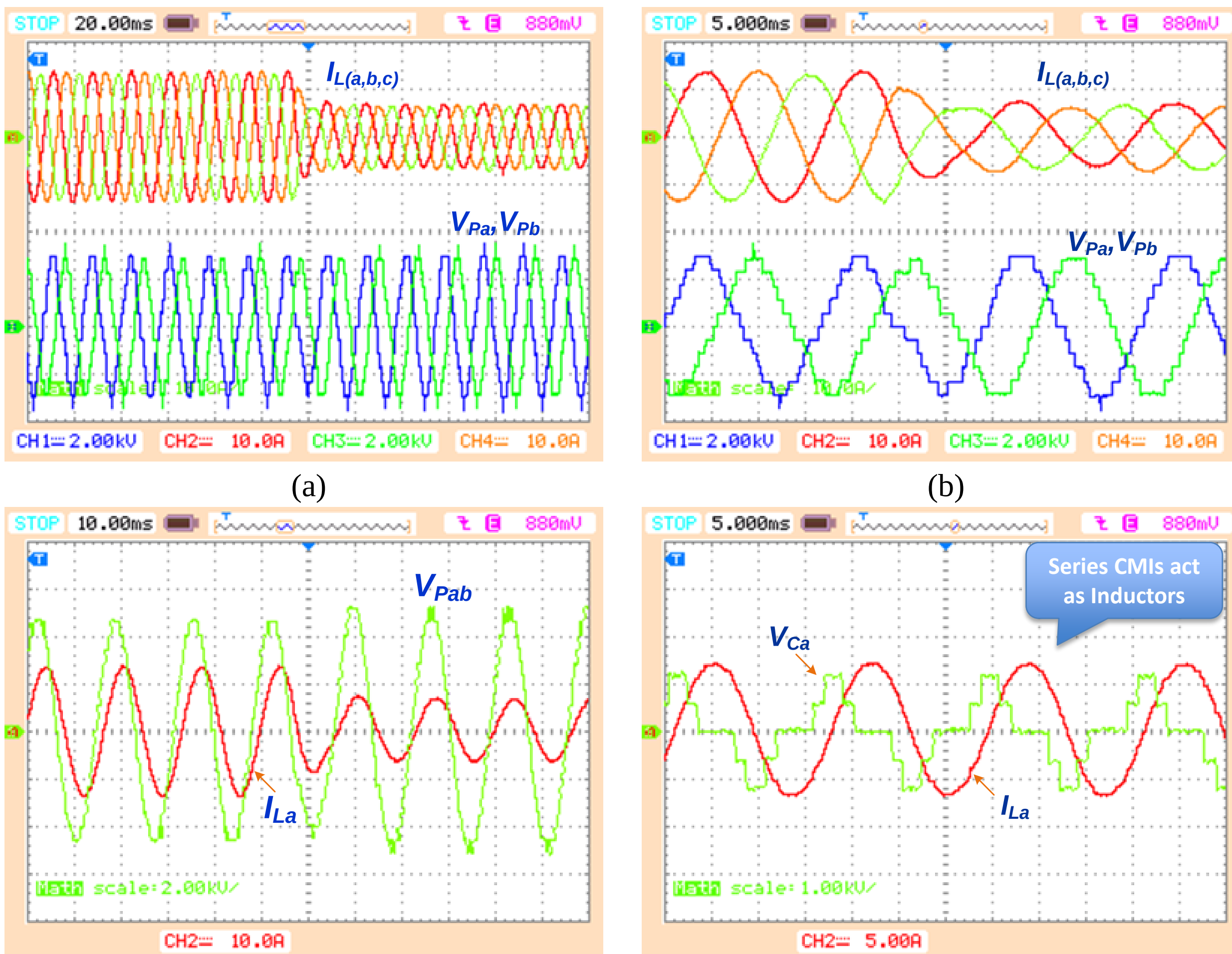

(c) (d)

Figure 3-12 Experimental waveforms of UPFC operating from case B1 to B2 (line impedance from original 0.5 pu to 1 pu), (a) and (b) shunt CMI phase voltage V_{Pa}, V_{Pb} and line current I_{La}, I_{Lb}, I_{Lc}, and, (c) line current I_{La} and series voltage V_{ca}.

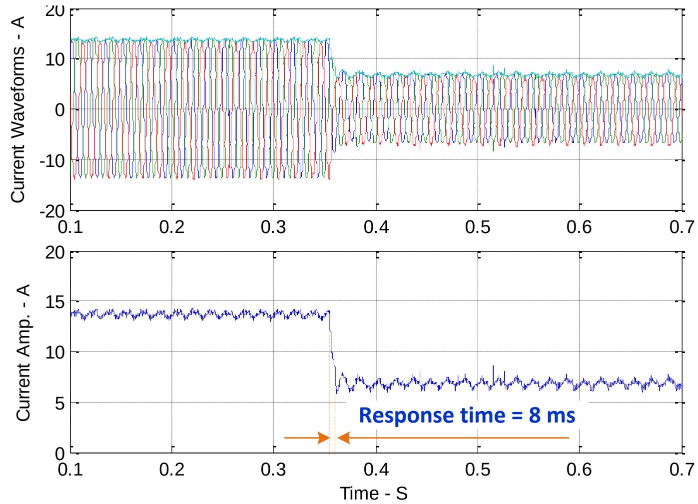

Figure 3-13 Measured dynamic response with operating point changing from case B1 to case B2 (line impedance from original 0.5 pu without compensation to 1 pu after compensation).

3.5.3 UPFC Operation - Independent *P/Q* Control

The functions of voltage regulation, phase shifting and line impedance compensation are from the standpoint of traditional power transmission control. Actually, the UPFC can simply control the magnitude and phase angle of the injected voltage in real time so as to maintain or vary the active and reactive power flow in the line to satisfy load demand and system operating conditions, i.e. independent *P/Q* control.

The blue curve in Figure 3-14 (a) shows the transmittable active power P and receiving-end reactive power Q vs. receiving-end voltage phase angle δ_0 in the uncompensated system, where original sending-end voltage is oriented to 0°. The circle in Figure 3-14 (a) shows the control region of the attainable active power P_0 and receiving-end reactive power Q_0 with series CMI voltage =0.517 pu and $\delta_0 = -30°$. In general, at any given δ_0, the transmitted active power P as well as receiving-end reactive power Q within the circle can be controlled by the UPFC, of course, with the rating limitation of series and shunt CMIs [35]. Several operating points of independent *P/Q* control have been tested. Figure 3-14 (b) shows the phasor diagram for one of the test cases, case C1: P =0.25, Q =0, in this case, line current $\vec{I_L}$ is in phase with receiving-end voltage $\vec{V_R}$ due to zero receiving-end reactive power Q. In this case, the calculated line current amplitude is 7.5 A. Figure 3-15 shows the corresponding experimental waveforms, (a) line current I_{La} and shunt CMI line voltage V_{Pab}, and (b) line current I_{La} and series CMI phase voltage V_{Ca}.

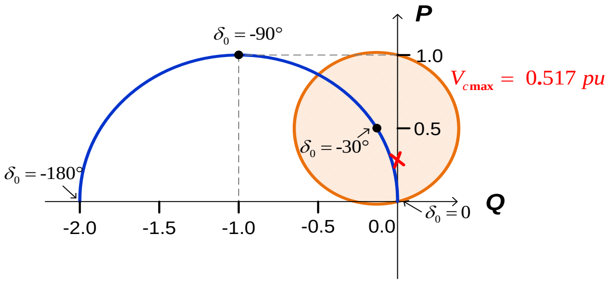

(a)

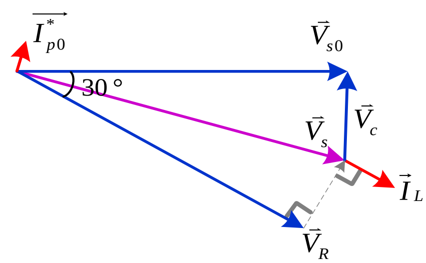

(b)

Figure 3-14 Independent P/Q control, (a) control region of the attainable active power P and receiving-end reactive power Q with series CMI voltage =0.517 pu and , (b) case C1: P =0.25, Q =0.

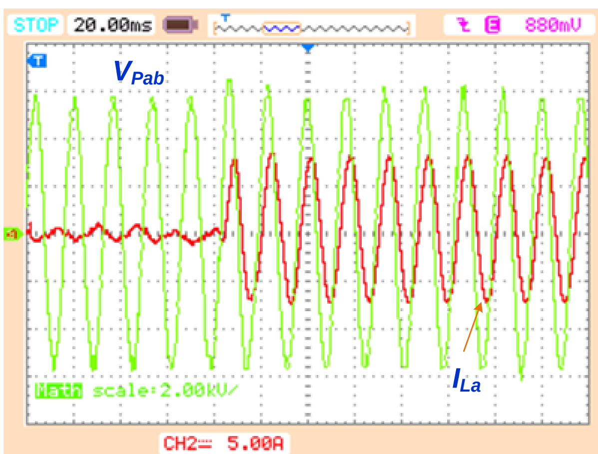

(a)

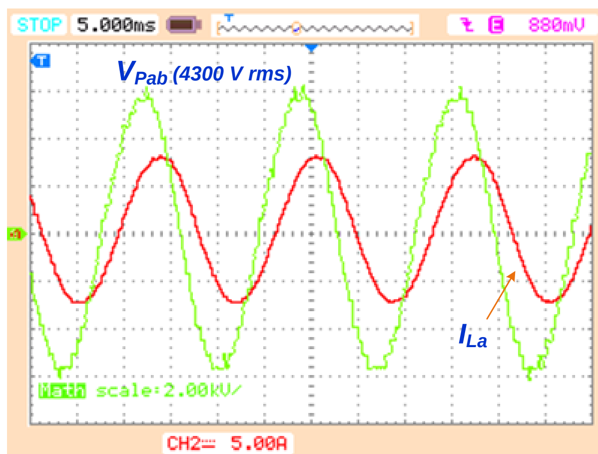

(b)

Figure 3-15 Experimental waveforms of UPFC operation case C1: P=0.25, Q=0, (a) and (b) line current I_{La} and shunt CMI line voltage V_{Pab} (c) line current I_{La} and shunt CMI phase voltage V_{Pa}, (d) line current I_{La} and series CMI phase voltage V_{Ca}.

Figure 3-15 (cont'd)

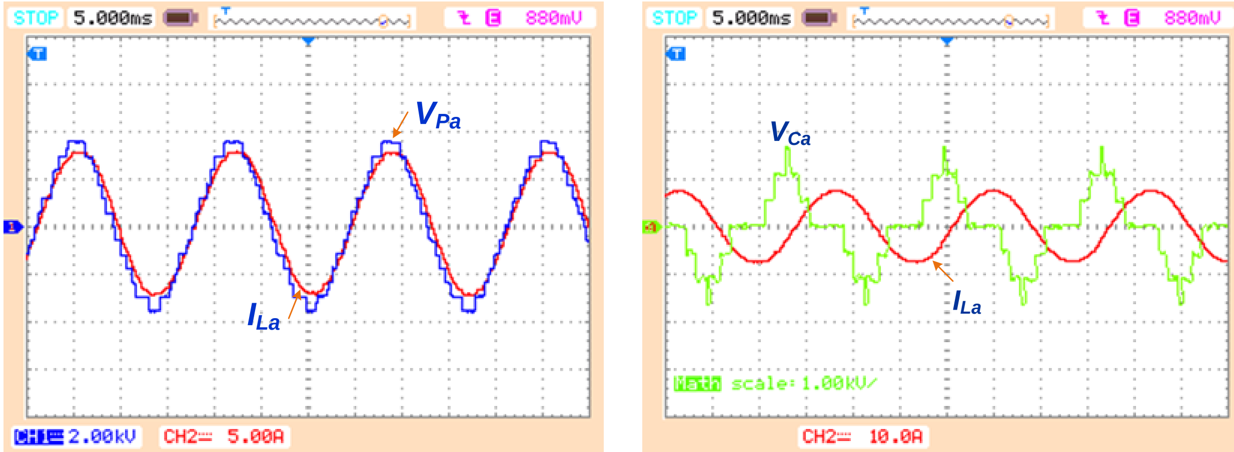

(c) (d)

3.6 Conclusion

This chapter present a modulation and control method for the transformer-less UPFC, which has the following features: 1) Fundamental frequency modulation of the CMI for extremely low THD of output voltage, low switching loss and high efficiency; 2) All UPFC functions, such as voltage regulation, line impedance compensation, phase shifting or simultaneous control of voltage, impedance, and phase angle, thus achieving independent active and reactive power flow control over the transmission line; 3) Dc capacitor voltage balancing control for both series and shunt CMIs; 4) Fast dynamic response (< 10 ms). The transformer-less UPFC with proposed modulation and control can be installed anywhere in the grid to maximize/optimize energy transmission over the existing grids, reduce transmission congestion and enable high penetration of renewable energy sources.

Next chapter will demonstrate an application of transformer-less UPFC for interconnecting two synchronous grids with large phase difference at a higher voltage higher power rating. Detailed analysis and experimental verification will be shown.

CHAPTER 4 Application of Transformer-less UPFC for Interconnecting Two Synchronous AC Grids with Large Phase Difference

In this chapter, application of innovative transformer-less unified power flow controller (UPFC) for interconnecting two synchronous AC grids with large phase difference is presented. The proposed transformer-less UPFC is based on two cascaded multilevel inverters (CMIs). As is well known, the real power flow between two generators is mainly determined by their phase difference. If two grids with large phase difference are initially separate from each other, once connected, there will be huge current flowing through the transmission line and will thus damage the generators or other supplementary equipments. Therefore, to connect two synchronous AC grids with each other without using extra device is mission impossible. Researchers have been investigating different approaches for this problem but still difficult to conquer, especially for real hardware implementation. An effective solution using transformer-less UPFC is demonstrated in this chapter. The proposed transformer-less UPFC can realize grid interconnection control, independent active and reactive power control, dc-link voltage balance control, etc. Furthermore, 1-pu equipment can effectively compensate system with phase difference as large as 30°. Experimental results based on 13.8-kV/ 2-MVA transformer-less UPFC prototype are demonstrated to validate the theoretical analysis.

4.1 Introduction

The modern power grid is a complicated mesh structure and sometimes suffered from severe congestions [74]. Furthermore, due to lack of effective control device (hardware), the grid network has to be/been over-built with lots of excessive capacity, still calling for new lines. However, excessive capacity and new lines do not increase total loadability proportionally. Sometimes, switching off line would even be better choice.

Another attempt to release the burdened transmission line is trying to connect two synchronous grids together or an islanded grid with a stronger grid [75-77]. Regarding the grid interconnection, researchers have emphasized more on system simulation and optimization [77-86]. Several existing technologies have been considered for power flow control along two synchronous grids with phase difference, such as series reactor [87], phase shifting transformers (PST) [81, 88, 89], variable frequency transformers (VFT) [80, 83] and HVDC [77, 84-86, 90, 91]. Furthermore, their benefits and drawbacks are analyzed as follows:

1. For the series reactor, it has easy implementation and simple operation principle. However, it has inevitably introduced huge reactive losses when current flowing through the reactor and can only be used to either increase power flow or decrease power flow, which is lack of adjustability;
2. For the PST, they can change the phase angle difference by changing the tap on the PST regulating winding. However, they suffered from single degree of adjustment, so in reality, it might need multiple PSTs in series. Moreover, it also consumes some Vars during operation;

3. The VFT is essentially a continuously variable PST that can operate at an adjustable phase angle. However, it does not have the ability to use Vars to regulate voltage, makes the system vulnerable to voltage fluctuation;
4. HVDC is the technology that used most frequently in this application these years, no matter it is a line-commutated converter (LCC) HVDC, capacitor commutated converter (CCC) HVDC and voltage source converter (VSC) HVDC. It is an enabling and promising technology but suffered from larger converter rating. It has been discussed that back to back connected HVDC have requirement of two full-power rating converter to interconnect two grids, which is cost expensive and efficiency reduction [92].

Besides the aforementioned technologies, few have really paid attention to the possibility of utilizing unified power flow controller (UPFC). As have been addressed in Chapter 4, one of the main reason limiting the wide application of UPFC is owing to the high cost and size of the bulky zigzag transformers. This high-voltage, high-power inverters have to use bulky and complicated zigzag transformers to reach their required VA ratings and desired voltage waveforms. The zigzag transformers are: 1) very expensive (30-40% of total system cost); 2) lossy (50% of the total power losses); 3) bulky (40% of system real estate area and 90% of the system weight); and 4) prone to failure.

To eliminate the transformer completely, a new transformer-less UPFC based on an innovative configuration of two CMIs has been proposed in [35], which is a modular transformer-less unified power flow controller (UPFC). The system configuration is as shown in Figure 3-2(a) and main system parameters for a 13.8-kV/ 2-MVA prototype (target system) is shown in Table 4.1.

Nevertheless, there are still challenges for the grid interconnection control of this new UPFC: 1) UPFC grid-interconnection control thus achieving independently control both the active and reactive power flow in the line; 2) dc capacitor voltage balance control for H-bridges of both series and shunt CMIs; This chapter presents the detailed modulation and control for the new transformer-less UPFC to address aforementioned challenges. The analytical analysis shows that this transformer-less UPFC can be 7 times smaller than a back-to-back HVDC in the same application. The UPFC functionality with proposed control method is verified at voltage level of 13.8 kV and both the steady-state and dynamic responses results will be shown in this chapter.

Table 4.1 Main System Parameters for 13.8 kV Prototype.

Parameters	**Value**
System power rating	2 MVA
V_{s0} rms	13.8 kV
Max series CMI current, I_C *rms*	84 A
Max shunt CMI current, I_P *rms*	42 A
V_{dc} (Shunt)	600 V
V_{dc} (Series)	600 V
H-bridge capacitance	4700 μF
No. of H-bridges per phase (Shunt)	20
No. of H-bridges per phase (Series)	8

4.2 Operation Principle of the Transformer-less UPFC for Grid Interconnection

The basic operation principle for transformer-less UPFC has been addressed in section 4.2. This section will focus on the operation principle of the transformer-less UPFC for grid interconnection application.

Figure 4-1 shows the application of the new transformer-less UPFC, which is used to interconnect two synchronous AC grids, where $\vec{V}_{S0}$ and $\vec{V}_R$ are the original sending-end and receiving-end voltage, respectively. Usually, the phase angle difference θ between $\overrightarrow{V_{s0}}$ and $\vec{V}_R$ is small, in this circumstance, UPFC is used to increase phase difference θ for higher power flow through the transmission line. Here, a totally different scenario is considered, the original θ is assumed to be big, e.g. 30° exists between $\overrightarrow{V_{s0}}$ and $\overrightarrow{V_R}$. In such a case, it is impossible to close this line directly; otherwise, huge current/power will go through the line to cause overload. For the system without UPFC compensation (V_C=0), the phase angle difference θ between $\overrightarrow{V_S}$ and $\overrightarrow{V_R}$ is fixed at 15°. When the UPFC is installed in a position between two grids (here is in the middle-point of the line, where the line impedance X_s=X_L) as shown in Figure 4-1, the series CMI is controlled to generate a desired voltage $\overrightarrow{V_C}$, in such a way, the amplitude and phase angle of middle-point voltage (shunt CMI voltage) $\overrightarrow{V_S}$ can be controlled according to active/reactive power command through the transmission line. For example, when the V_c is injected to adjust the phase angle θ from original 15° to a smaller value, the power flow through the line then is controlled in a limited value.

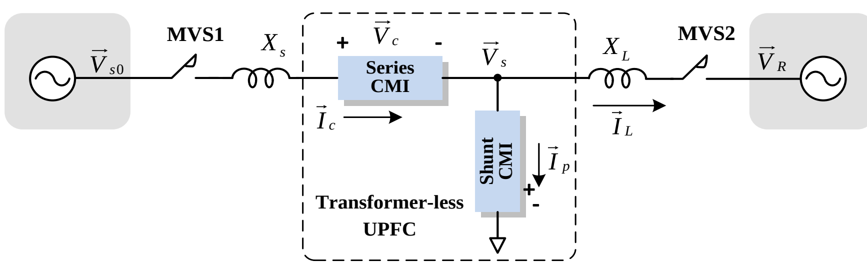

Figure 4-1 Interconnecting two synchronous grids with transformer-less UPFC.

The control objective for transformer-less UPFC in this chapter is: 1) Active Power (i.e. power angle between V_S and V_R) regulation by the series CMI; 2) Reactive power compensation by shunt CMI. The shunt CMI will compensate the line reactive power and support the middle-point voltage like a static synchronous compensator (STATCOM); 3) DC balance control for both CMIs (series CMI current $\overrightarrow{I_C}$ and the shunt CMI current $\overrightarrow{I_P}$ to be perpendicular to their voltages $\vec{V}_C$ and $\vec{V}_S$, respectively). Figure 4-2 shows the corresponding phasor diagram, where $\overrightarrow{V_{s1}} = \overrightarrow{V_{s0}} - \overrightarrow{V_C}$. The injected series voltage changes the original sending-end voltage from $\overrightarrow{V_{s0}}$ to $\overrightarrow{V_{s1}}$. As a result, the phase angle θ between $\overrightarrow{V_s}$ and $\overrightarrow{V_R}$ is reduced from original 15°, to a new value decided by the active power requirement over the transmission line. At the same time, the reactive power of the line is compensated by the shunt CMI, thus the active and reactive power flow out of $\overrightarrow{V_{s0}}$ are exactly the same as active and reactive power flow into $\overrightarrow{V_R}$, respectively.

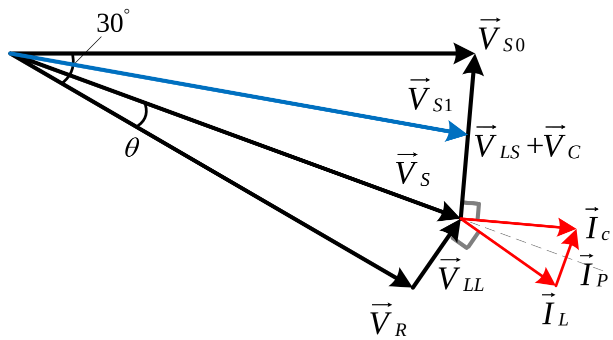

Figure 4-2 Phasor diagram of transformer-less UPFC to compensate phase difference between two grids.

Generally, the rating of the series CMI voltage is determined by its controllable region, or more specifically, the phase difference between sending and receiving end. Once the transmitted active power P and reactive power Q over the line with the transformer-less UPFC is given, the power angle θ can be calculated according to

$$P + jQ = \vec{V}_R \cdot \left(\frac{\vec{V}_S - \vec{V}_R}{jX_L} \right)^*, \vec{V}_R = 1\angle(-30), \vec{V}_S = V_S\angle(-30+\theta) \qquad (4.1),$$

where symbol * represents the conjugate of a complex number, θ is the phase angle between new sending-end voltage $\vec{V}_S$ and receiving-end voltage $\vec{V}_R$, X_L is the equivalent transmission line impedance. The new sending end $\vec{V}_S$ magnitude V_s, can be decided according to the geometrical relationship,

$$\frac{V_s}{\sin(180-\theta-\delta/2)}=\frac{1}{\sin(90-\delta/2)},\quad \delta=30° \tag{4.2}$$

Once the power angle θ is obtained, the series CMI injected voltage $\vec{V}_C$ can be calculated as

$$\vec{V_c}=\overrightarrow{V_{s0}}-\vec{V_R}e^{j2\theta}=1-\cos(-30+2\theta)-j\sin(-30+2\theta) \tag{4.3}$$

As can be seen from (4.3), the rating of the series CMI is closely related to the power angle and their analytical relationship is shown in Figure 4-3.

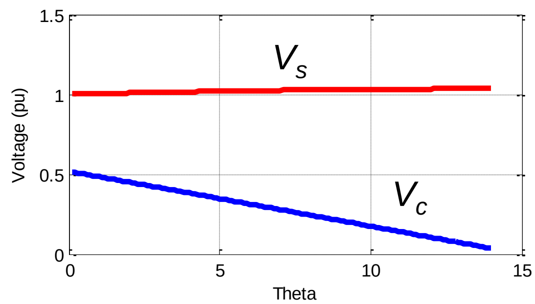

Figure 4-3 Series and shunt voltage rating of transformer-less UPFC versus power angle θ.

The current rating $\vec{I}_L$ is determined by

$$\overrightarrow{I_L}=\frac{\vec{V}_S-\vec{V}_R}{jX_L},\ where\ \vec{V}_S=V_s\angle(-30+\theta) \tag{4.4}$$

Next, the shunt CMI injects current $\vec{I}_P$ to decouple the series CMI current $\vec{I}_C$ from the line current $\vec{I}_L$. In such a way, zero active power exchange to both series and shunt CMIs can be achieved, making it possible to apply the CMI with floating capacitors to the proposed transformer-less UPFC. Therefore, we have

$$\begin{cases} P_{se}=\vec{V}_C\cdot\vec{I}_C=0 \\ P_{sh}=\vec{V}_S\cdot\vec{I}_P=0 \end{cases} \tag{4.5}$$

It means the series CMI current $\vec{I}_C$ and the shunt CMI current $\vec{I}_P$ need to be perpendicular to their voltages $\vec{V}_C$ and $\vec{V}_S$, respectively, as illustrated in Figure 4-2. With the geometrical relationship of the voltages and currents in Figure 4-2, the shunt CMI output current can be calculated as

$$\overrightarrow{I_p} = \frac{\sin(\delta)}{\sin\left((180-\delta)/2\right)} \overrightarrow{I_L} e^{j((180-\delta)/2)} \tag{4.6}$$

In summary, there are two critical steps for the operation of UPFC: a) calculation of injected voltage $\vec{V}_C$ for series CMI according to active/reactive power command over the transmission line expressed in (4.3), and b) calculation of injected current $\vec{I}_P$ for shunt CMI from (4.6) to guarantee zero active power into both series and shunt CMIs.

An important thing to highlight here is with a given 30° phase angle difference between $\overrightarrow{V_{s0}}$ and $\overrightarrow{V_R}$, from Figure 4-1 and Figure 4-2, we can calculate that the voltage rating of shunt CMI is about 1 *pu*, and current rating of shunt CMI is about 0.5 *pu*, while the voltage rating for series CMI is about 0.517 *pu*, and the current rating of series CMI is 1 *pu*. Therefore, the total UPFC rating is 1 *pu*. Consequently, the much reduced converter rating of transformer-less UPFC will minimize the system cost and initial capital investment.

4.3 Fundamental Frequency Modulation for CMIs

As discussed in chapter 4, there are basically two main categories for modulation strategy used for multilevel structure, which are fundamental frequency modulation (FFM) and high-frequency pulse width modulation (PWM). Compared to the high-frequency PWM, the FFM has much lower switching loss, making it attractive for the transmission-level UPFC and other high-voltage high-power applications. The FFM has been investigated for many years, however, most studies focused on the FFM optimization with low number of modules (e.g. 4 to 5) and the steady-state THD minimization. In this work, FFM will be designed with high number of modules. Specifically, switching angles will be optimized for all 8 series H-bridge modules and 20 shunt H-bridge modules to achieve extremely low THD.

4.3.1 Optimization of Switching Angles for Minimum THD

Figure 4-4 shows the operation principle of traditional FFM, where phase a output voltage of an 11-level CMI is shown as an example. A stair-case voltage waveform, V_a could be synthesized when each of five H-bridge modules generates a quasi-square wave, V_{H1}, V_{H2}, …, V_{H5}. Each H-bridge has the identical dc-link voltage V_{dc} for the modular design consideration. Different approaches have been studied to decide the switching angles of H-bridge modules for selected harmonic elimination (SHE) or minimum THD. However, these papers mostly focused on low number (less than 5) of H-bridge modules. In this work, switches angles will be optimized for minimum THD with the high number of H-bridge modules for the transformer-less UPFC (8 for series CMI and 20 for shunt CMI as given in Table 4.1).

The Fourier series expansion of the CMI output voltage shown in Figure 4-4 is

$$V_a(\omega t) = \sum_{n=1}^{\infty} V_{an} \cdot \sin(n\omega t) = \begin{cases} \dfrac{4}{n\pi} \displaystyle\sum_{k=1}^{s} V_{dc} \cdot \cos(n\alpha_k), & \text{for odd n} \\ 0, & \text{for even n} \end{cases} \tag{4.7}$$

where n is harmonic number, s is the total number of H-bridge modules, and α_k represents the switching angle for the k^{th} H-bridge module. For a three-phase system, the THD of line voltage instead of phase voltage is of interest. Therefore, all triplen harmonics will be ignored for voltage THD calculation, which then can be expressed as

$$THD = \frac{1}{V_{a1}} \sqrt{\sum_{n=5,7,11,...}^{\infty} V_{an}^2} \tag{4.8}$$

Basically, equation (4.8) gives an objective function to be minimized, with the following two constraints:

$$0 < \alpha_1 < \alpha_2 < \alpha_3 .... < \alpha_s < \frac{\pi}{2} \tag{4.9}$$

and

$$V_{a1} = \frac{4}{\pi} \sum_{k=1}^{s} V_{dc} \cos(\alpha_k) \qquad (4.10).$$

Equation (4.9) indicates that the switching angles from first H-bridge module to last H-bridge module gradually increase, while the corresponding duty cycles (pulse width) of output voltage would inversely decrease. In (4.10), V_{a1} is the desired fundamental voltage, which is equal to the reference voltage V_{a1}=V_a^*. With the Matlab optimization toolbox, we can get the minimum THD with above two constraints in (4.9) and (4.10). The corresponding results have been shown in Figure 4-5. For a comparison purpose, the line voltage THD with angles decided by nearest level is also given [93]. From Figure 4-5, it clearly shows that the THD is decreased with the increase of number of H-bridge modules *s*. When $s \geq 15$, the minimum THD will be smaller than 1% even without any additional filters.

In addition, an alternative optimization of FFM could be the "minimum weighted total harmonics distortion (WTHD)". The WTHD achieves the minimum current THD for inductive loads (i.e., directly optimized for best power quality), which is preferred for application where current distortion is of interest. Then, the objective function in (4.8) should be changed to

$$WTHD = \frac{1}{V_{a1}} \sqrt{\sum_{n=5,7,11,...}^{\infty} (V_{an}/n)^2} \qquad (4.11).$$

As shown in Table 4.1, for the 13.8 -kV/ 2 -MVA system, the number of H-bridges for shunt CMI is 8 and the number of H-bridges for series CMI is 20. Figure 4-6 shows FFM with total 20

H-bridges, (a) output voltage and current and (b) output voltage of each H-bridge, where modulation index MI=1 in this case. MI is defined as peak phase voltage divided by ($s*V_{dc}$). With total 20 H-bridges, the CMI output phase voltage can reach up to 41 levels. The output voltage is very close to sinusoidal waveform, achieving extremely low THD (= 0.85%). The corresponding optimized switching angles for this case are given in Table 4.2.

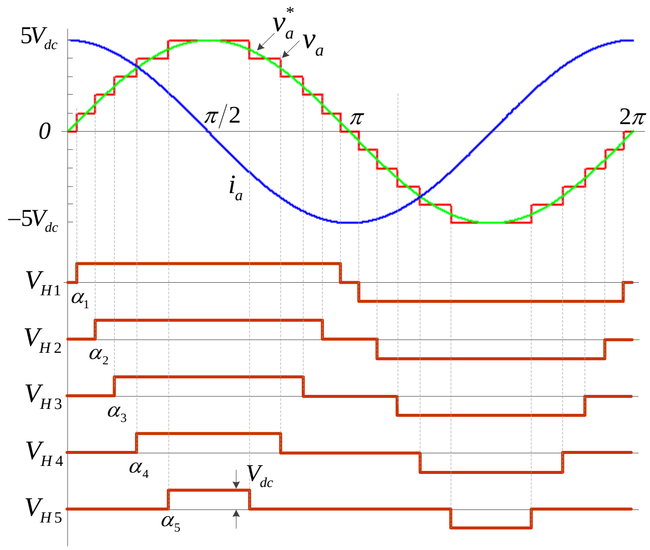

Figure 4-4 Operation principle of FFM.

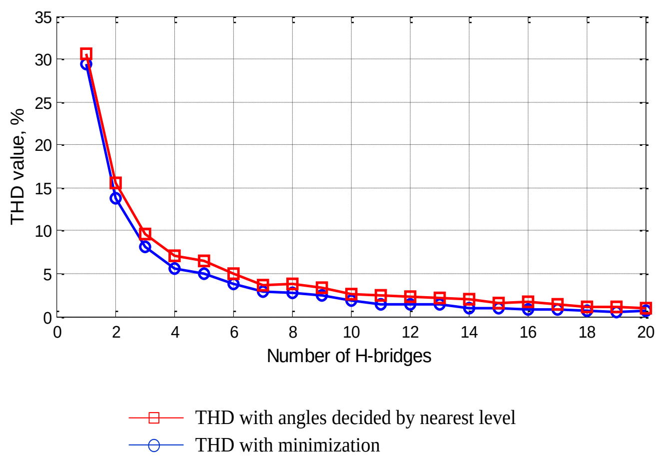

Figure 4-5 Minimum THD versus number of H-bridge Modules.

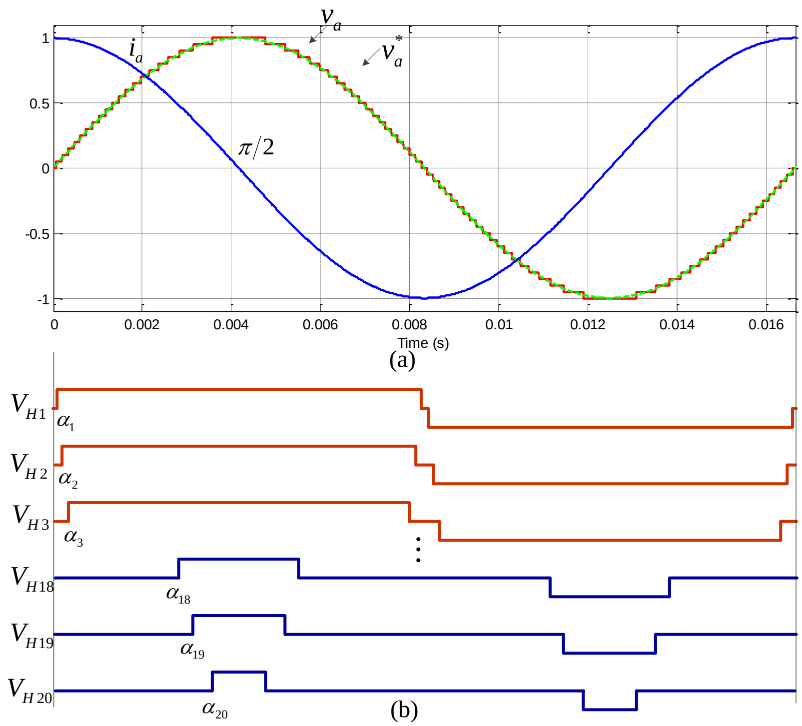

Figure 4-6 FFM with total 20 H-bridges, (a) output voltage and current (41 levels) and (b) output voltage of each H-bridge.

Table 4.2 Switching Angle for the Case MI=1.

Switching Angles	α_1	α_2	α_3	α_4	α_5	α_6	α_7	α_8	α_9	α_{10}
Value (rad)	*0.0276*	*0.0745*	*0.1244*	*0.1828*	*0.2194*	*0.2657*	*0.3380*	*0.3952*	*0.4438*	*0.4947*
Switching Angles	α_{11}	α_{12}	α_{13}	α_{14}	α_{15}	α_{16}	α_{17}	α_{18}	α_{19}	α_{20}
Value (rad)	*0.5535*	*0.6213*	*0.6897*	*0.7373*	*0.7972*	*0.8900*	*0.9689*	*1.0649*	*1.1849*	*1.3550*

4.3.2 Analysis of Capacitor Charge of H-bridges

Capacitor charge of H-bridges will be studied based on two layers: 1) first layer is overall capacitor charge, meaning the total capacitor charge of all H-bridges of any one of three phases; 2) the other layer is individual capacitor charge, meaning the capacitor charge of each H-bridge.

In previous analysis, the CMI output voltage is expected to lead or lag the output current by 90°, to achieve zero active power flow from ac side into dc capacitors. In practice, the dc capacitor voltage can't be maintained due to the power loss of switching devices and capacitors. Still take phase a of a CMI as an example, the overall active power flow of this phase from ac side into dc capacitors can be expressed as

$$P_a = V_o I_o \cdot \cos(\theta) \tag{4.12},$$

where V_o and I_o are rms values of CMI output phase voltage and current, respectively, and θ is the phase angle between output voltage and current. As mentioned before, if θ is exact 90°, then P_o = 0. No any active power will flow from ac side to dc side to charge dc capacitors. Obviously, in this case, no matter overall capacitor charge or individual capacitor charge is zero. However, if the phase angle θ is smaller than 90°, denoted as $\left(90^{\circ} - \Delta\theta\right)$, the overall dc capacitor voltage could be balanced if

$$P_a = V_o I_o \cdot \cos(90 - \Delta\theta) = V_o I_o \sin(\Delta\theta) = P_{loss} \tag{4.13},$$

where P_{loss} is the total power loss of switching devices and capacitors of one phase. Therefore, the CMI should be controlled to absorb small amount of active power in order to maintain the desired dc-link voltage.

On the other side, with the shifted phase angle $\Delta\theta$, the individual capacitor charge for k^{th} H-bridge, C_k over one fundamental period is:

$$C_k = \int i_{dc} dt = \frac{2}{\omega} \cdot \int_{\alpha_k - \Delta\theta}^{\pi - \alpha_k - \Delta\theta} \sqrt{2} I_o \cos(\theta) d\theta = \frac{4}{\omega} \sqrt{2} I_o \cos(\alpha_k) \sin(\Delta\theta) \tag{4.14},$$

where k=1, 2, …, s. In (4.14), the entire modules in the same phase will have same load current I_o and phase angle shift $\Delta\theta$. Equation (4.14) indicates the quite different individual capacitor charge due to the unequal duty cycles of H-bridge modules. Figure 4-7 illustrates the capacitor charges of 20 shunt H bridges with corresponding switching angles given in Table 4.2. When the same load current go through all these 20 H bridges, dc capacitor of each H bridge will be charged differently.

One important point here is, the smaller switching angle (corresponding to larger duty cycle) an H-bridge module has, the more capacitor charge it will get.

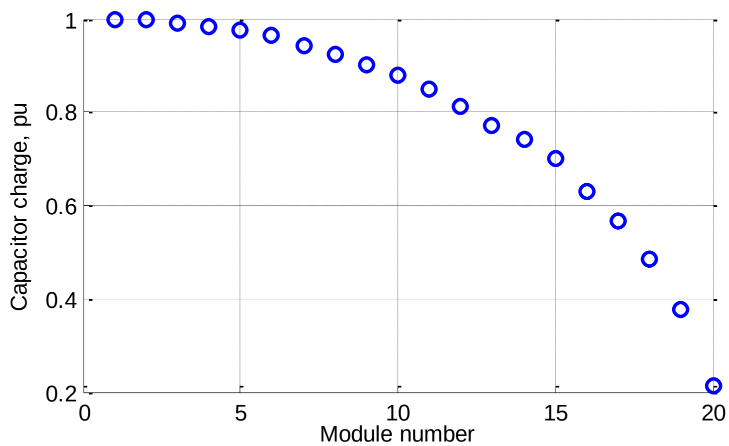

Figure 4-7 Capacitor charge of 20 H-bridge modules with FFM.

4.4 Power Flow and DC-link Voltage Control of Transformer-less UPFC

4.4.1 Individual DC Control and Phase Balance Control

The dynamic model and overall power flow and dc-link voltage control for transformer-less UPFC is addressed in Chapter 3. This section will focus on the analysis of phase balance and individual DC control of system.

Usually, the dc capacitor voltage balance control for CMIs adopts hierarchical control structure, e.g. an outer control loop and an inner control loop. The outer loop regulates the overall active power flowing to all H-bridge modules of any one of three phases, while the inner loop distributes power flowing equally to each individual H-bridge module [17]. As we discussed in section III, one fact is that the capacitor charge of individual H-bridge will be unequal due to the unequal duty cycles of each H-bridge by FFM. The smaller switching angle (corresponding to larger duty cycle) an H-bridge module has, the more capacitor charge it will get. Besides the overall dc capacitor voltage control present above, it's necessary to have the individual dc capacitor voltage control for the charge balance between the modules in the same phase. This is implemented by pulse swapping every fundamental cycle [69]. Figure 4-8 illustrates the pulse swapping from one fundamental cycle to the next fundamental cycle, taking 8 H-bridge modules as an example. In the first fundamental cycle, the optimized 8 switching angles are distributed to 8 H-bridge modules in a special sequence. After one cycle, the switching angles for the H-bridge modules will be swapped as illustrated in Figure 4-8. If we take a look at the switching angles for each of the ten modules, it would be in an order of α_1, α_8, α_2, α_7, α_3, α_6, α_4, α_5, α_1,… for the successive fundamental cycles. Since smaller switching angle (corresponding to larger duty cycle) of an H-bridge module results in more capacitor charge. Therefore, such an order for the H-bridge module would result in better charge/discharge balance, leading to lower dc-link voltage ripple.

Even with both overall and individual dc capacitor voltage control described above, it is still possible to have the dc capacitor voltage unbalance between the three phases. Physically, the shunt CMI or series CMI may have different power loss between the three phases. If same P_{sh} / P_{se} from overall dc voltage regulator is applied to all three phases of shunt/series CMI as shown in Figure 3-4(a), the mismatch between the absorbed active power and the power loss would cause the voltage unbalance. One simple solution to this problem is to change the overall dc voltage control in Figure 3-4(a) from one 3-phase integrated controller to three separated controllers. Figure 4-9 shows the three-phase separated overall dc voltage control for series CMI, where V_{dc_sea}, V_{dc_seb}, and V_{dc_sec} are dc capacitor voltage feedback of phase a, b, and c, respectively; P_{se_a}, P_{se_b}, P_{se_c} are active power commands, which are used to compensate the power loss of each phase; i_{c_a}, i_{c_b} and i_{c_c} are instantaneous currents of each phase of series CMIs; Δv_{c_a}, Δv_{c_b}, Δv_{c_c} are generated as the *active-voltage* components, which are in phase with current i_{c_a}, i_{c_b} and i_{c_c}, respectively. In a three-phase well balanced system, P_{se_a}, P_{se_b}, P_{se_c} will be close to each other, indicating the same active power is needed to compensate the power loss of each phase; while in a system with different power losses between three phases, the separated dc regulators will output different value of P_{se_a}, P_{se_b} and P_{se_c} to guarantee the balanced dc capacitor voltage. It is notable that the value of P_{se_a}, P_{se_b} and P_{se_c} are relatively small when compared to the total UPFC system rating. Similarly, from Figure 3-4(a) we can derive the corresponding three-phase separated overall dc voltage control for shunt CMI.

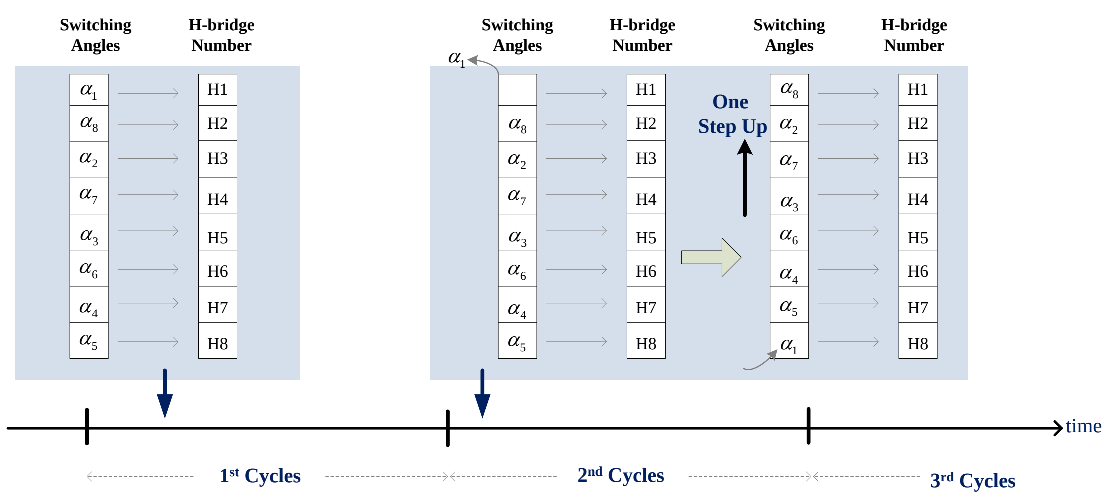

Figure 4-8 Illustration of pulse swapping from one fundamental cycle to next fundamental cycle.

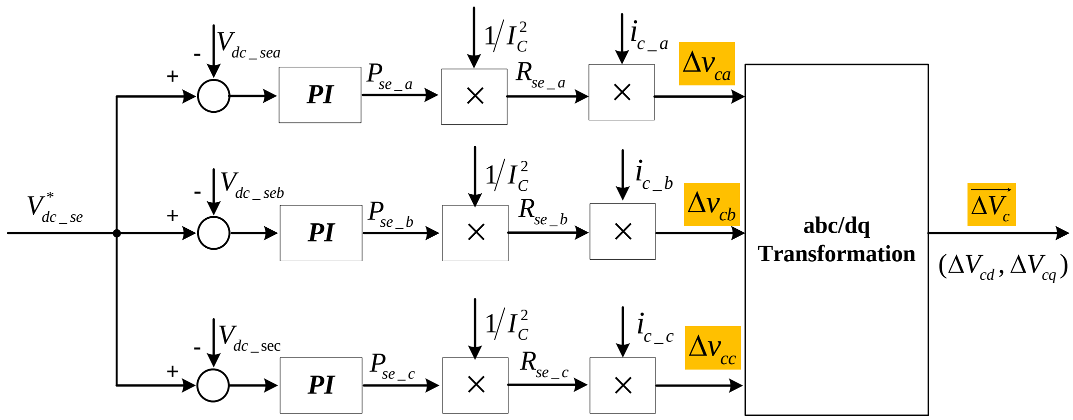

Figure 4-9 Three-phase separated overall dc voltage control for series CMI, considering capacitor-voltage unbalance between the three phases.

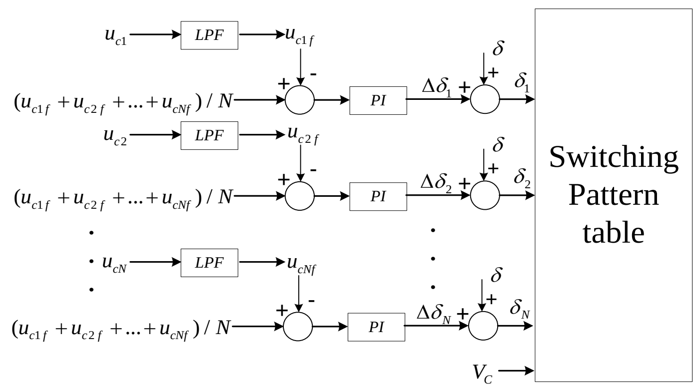

Figure 4-10 Individual DC voltage control for series/shunt CMI considering capacitor voltage unbalance between modules.

4.4.2 Implementation and Architecture of Control System

The control system for the CMIs based UPFC consists of a main control board for the system level control and local control boards for module level control as shown in Figure 4-11. The main control board has a state-of-the-art floating-point DSP and FPGA, which will be used for implementation of overall system control as shown in Figure 3-4(a), system level protection, as well as communications with local control board and Human machine interface (HMI). In the designed main control board, total 13*8 = 104 pairs of fiber-optic transmitters and receivers are available, which provides enough channels to communicate with total 84 H-bridge modules (24 series H-bridge modules, 60 shunt H-bridge modules). The main task of the local control board is to implement individual dc voltage feedback, fundamental switching signals generation, local protection and communication with main control board. The universal asynchronous receiver transmitter (UART) communication is used between the main control board and local control board. High communication speed with baud rate 500 k is used to support the high-frequency sampling ≥ 1 kHz.

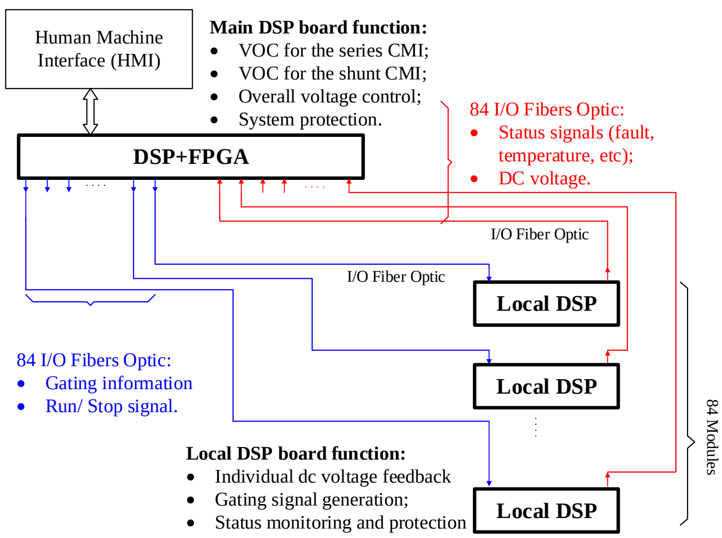

Figure 4-11 The architecture of the control system.

4.5 Experimental Results

4.5.1 Test System Setup

A 13.8 kV/ 2 MVA transformer-less UPFC prototype has been developed to validate the UPFC to interconnect two synchronous grids. The test setup is shown in Figure 4-1 and the main system parameters for the prototype are given in Table 4.3. The prototype of the whole system setup is shown in Figure 4-12. In Figure 4-1, the sending-end voltage $\vec{V}_{S0}$ has same amplitude as receiving-end voltage $\vec{V}_R$, but 30° phase leading. This 30° phase leading is introduced by the

Y/Δ transformer. As mentioned before, it is impossible to directly close this line without UPFC compensation, otherwise the huge current will flow through the line due to the voltage different caused by 30° phase angle difference. The line current/power can be controlled to any desired value when a transformer-less UPFC is installed between two grids. In Figure 4-1, the new UPFC is installed in the middle-point of two grids, and X_s=X_L. The series CMI is controlled to generate a desired voltage $\overrightarrow{V_C}$, in such a way, the amplitude and phase angle of middle-point voltage (shunt CMI voltage) $\overrightarrow{V_S}$ can be controlled according to active/reactive power command over the transmission line. Figure 4-13 shows the diagram for different operating points of the system compensated by UPFC. In Figure 4-13 (a), the phase angle θ between $\overrightarrow{V_S}$ and $\overrightarrow{V_R}$ is 15°, which is the original phase angle without UPFC compensation (V_C=0). This phase angle could be further increased for higher power flow or decreased for less power, as shown in Figure 4-13 (b) with θ = 20°, and Figure 4-13 (c) with θ = 10°. Here the different operating points with different θ indicate different transmitted active power. It is notable that in all cases, shunt CMI is used to compensate the line reactive power, and provide the middle-point voltage support.

Figure 4-12 UPFC installed to 15-KV Lab.

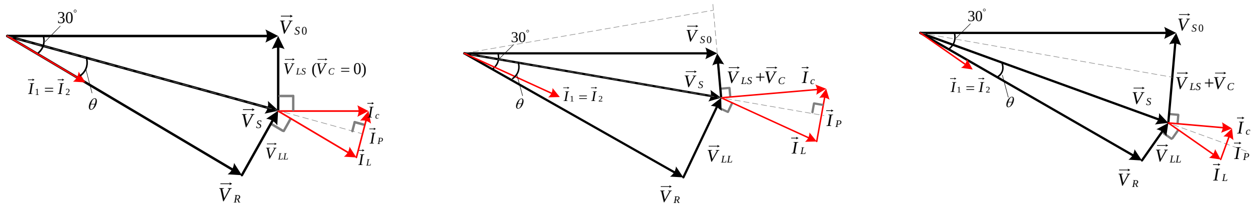

(a) (b) (c)

Figure 4-13 Phasor diagram for different operating points of independent *P/Q* control with (a) θ = 15 °, (b) θ = 20 °, (c) θ = 10 °(In all cases, line reactive power compensated by shunt CMI).

4.5.2 Startup Sequence and Grid Interconnection

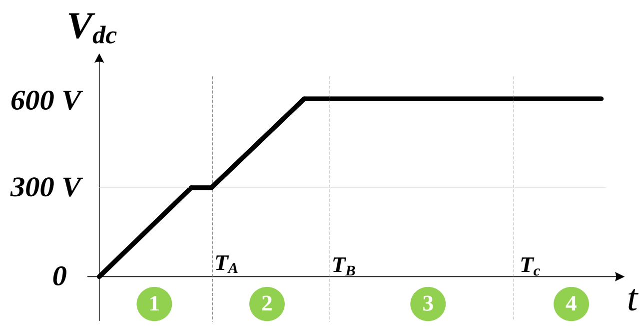

Figure 4-14 UPFC start-up sequence.

The whole operation of transformer-less UPFC is divided into four modes, which include pre-charge mode, inverter charge mode, grid interconnection mode and UPFC operation mode, which show in Figure 4-14.

Before grid interconnection, MVS1 in Figure 4-1 is closed while MVS2 is open. Initially, dc link of each module is charge to about 300 V by variac. Then power supply board of each module and local DSP board will begin functioning, the communication between main DSP and local DSP is established. After that, a running signal will be given by the upper command, the system will run into inverter charge mode. In inverter charge mode, each of the dc link voltage of shunt and series CMIs will charge to 550V and 600 V, separately.

Table 4.3 System Parameters for 13.8-kV Test Setup.

Parameters	**Value**
System power rating	2 MVA
V_{s0} rms	13.8 kV
Max series CMI current, I_C *rms*	84 A
Max shunt CMI current, I_P *rms*	42 A
Nominal V_{dc} (Shunt)	600 V
Nominal V_{dc} (Series)	450-600 V
H-bridge dc capacitance	2350 μF
No. of H-bridges per phase (Shunt)	20
No. of H-bridges per phase (Series)	8
X_S	60 mH (0.24 pu)
X_L	60 mH (0.24 pu)

After the inverter charge mode, the dc voltage maintains at its nominal value, the system is in standby status. Once the upper command of closing MVS2 is sent, the system will run into grid-interconnection mode. Before this step, the series CMI output almost zero voltage. During grid interconnection, the series CMI will output voltage to compensate for the 30° phase angle difference, the experimental results are shown in Figure 4-15. As can be seen, almost zero current flowing through the transmission line and small surge into the grid. After the grid-interconnection mode, the two previously separate grids are connected together and is ready to run at UPFC operation mode according to upper command.

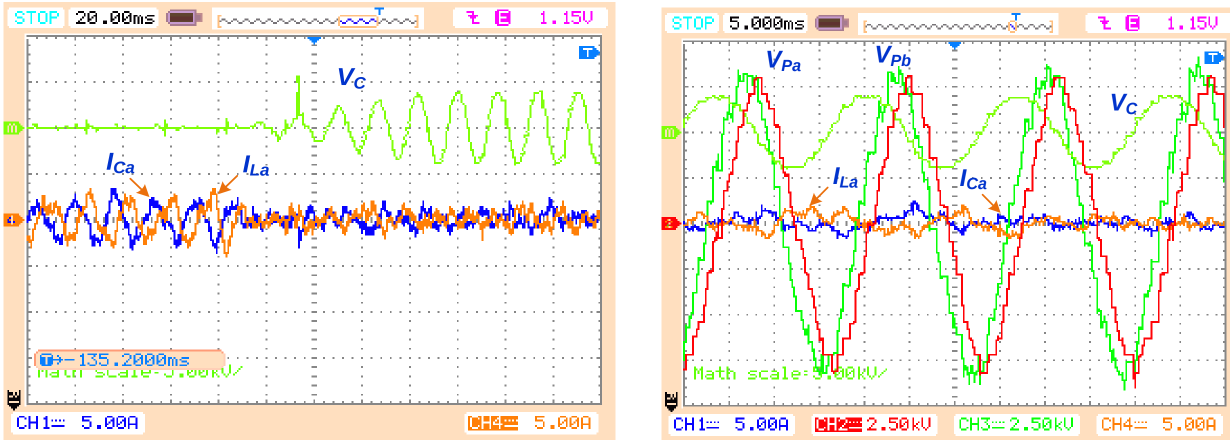

(a) (b)

Figure 4-15 Experimental waveforms of UPFC operation during grid interconnection (a). transition during recloser closes; (b). completion of grid interconnection.

4.5.3 Independent Power Flow Control and DC Control

After the grid interconnection, the system is now ready to run at UPFC operation mode. As mentioned previously, the control objective for transformer-less UPFC include active power regulation by the series CMI, reactive power compensation by shunt CMI and dc balance control for both CMIs. Some selected test results are shown to verify the effectiveness UPFC functionality and the control strategy.

Figure 4-16 shows the experimental waveforms of UPFC running at operating point 1: phase angle difference θ is equal to 2°. Figure 4-16 (a) shows line current I_{La} going to receiving-end, and shunt CMI line voltage V_{pab}; (b) and (c) are average dc link voltage error for shunt and series CMIs; (d)-(g) show individual dc link voltage error for shunt and series CMIs. Here, $v_{average-error} = v_{average} - v^{*}_{average}$ *and* $v_{individual-error} = v_{individual} - v_{average}$. The average series V_{dc} reference ($v^{*}_{average-se}$) is 600 V and average shunt V_{dc} reference ($v^{*}_{average-sh}$) is 550 V. The dc voltage references are chosen to keep the modulation index (MI) of inverter near unity to achieve lowest THD. As can be seen from the voltage-error waveforms, $\left|v_{average-error}\right| \leq 30\,V$ *and* $\left|v_{individual-error}\right| \leq 50\,V$. All the dc link voltages are well controlled and maintained to track their reference. From these test results, after the interconnection of the two grids, transformer-less UPFC can realize independent power flow control along the transmission line as well as a balanced dc link voltage control.

Figure 4-17 shows the experimental waveforms at operating point 2: phase angle difference is 7°. Figure 4-17(a) and (b) present line current I_{La}, series CMI current I_{Ca} and shunt current I_{Pa}, (c) and (d) are average dc link voltage error for shunt and series CMI; (e)-(h) show individual dc link voltage error for shunt and series CMI. The voltage-error definition is same as for operation point 1. With the phase angle θ controlled from 2° to 7°, the corresponding line current was increased from 10 A to 35 A, and the series CMI current was increase from 10 A to 40 A. In this operating point, the series CMI is unnecessary to output large voltage. Therefore, an adaptive dc link voltage control is utilized here in order to keep modulation index of series CMI to be unity where the FFM has best output waveform quality. Therefore, the average series V_{dc} reference is 450 V and average shunt V_{dc} reference is still 550 V. With the increasing of the line current, the voltage ripple on dc link capacitor becomes larger. However, the average dc link voltage of each phase is still able to track its reference value and all the individual dc link voltage of each module is able to track its average value, $\left|v_{average-error}\right| \leq 30\,V$ *and* $\left|v_{individual-error}\right| \leq 50\,V$. From these test results, the transformer-less UPFC can independently control real and reactive power over the transmission line, in heavy load and light load condition. All of the dc link voltage of CMI can be controlled around its reference value.

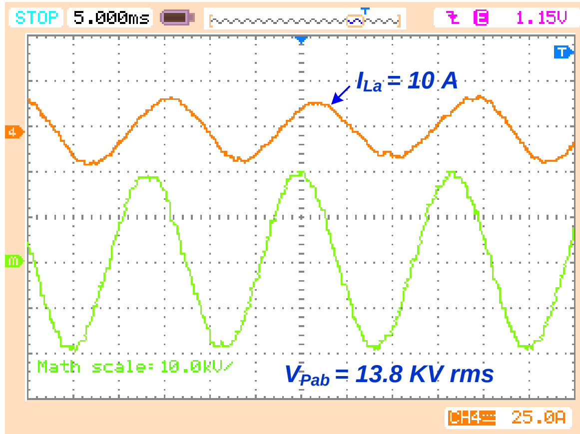

(a)

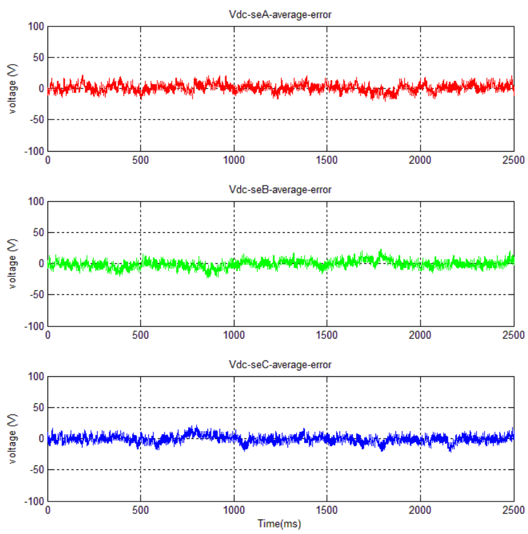

(b)

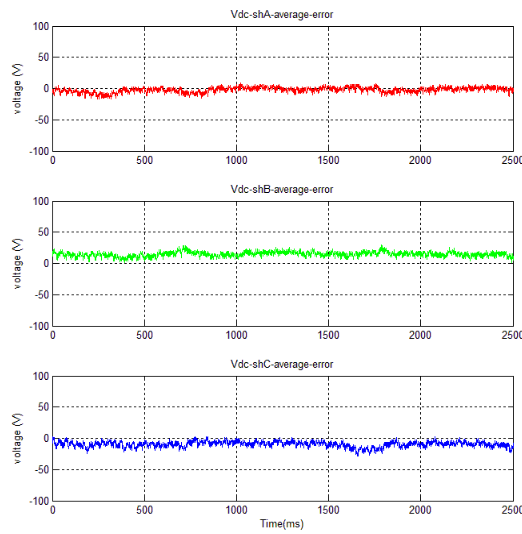

(c)

Figure 4-16. Experimental waveforms of UPFC running in operating point 1: Phase angle difference θ is controlled to 2°. (a). Transmission line current I_{La} and shunt CMI line voltage V_{pab}; (b). average series CMI dc link voltage error; (c). average shunt CMI dc link voltage error (d). series CMI individual module 1-4 dc link voltage error; (e). series CMI individual module 5-8 dc link voltage error; (f). selective shunt CMI individual module 1-4 dc link voltage error; (g). selective shunt CMI individual module 5-8 dc link voltage error.

Figure 4-16 (cont'd)

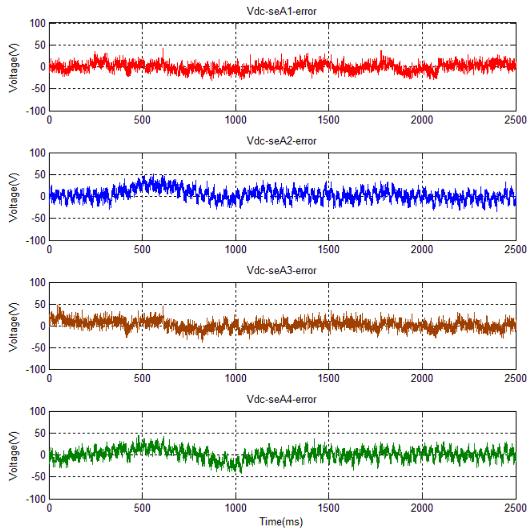

(d)

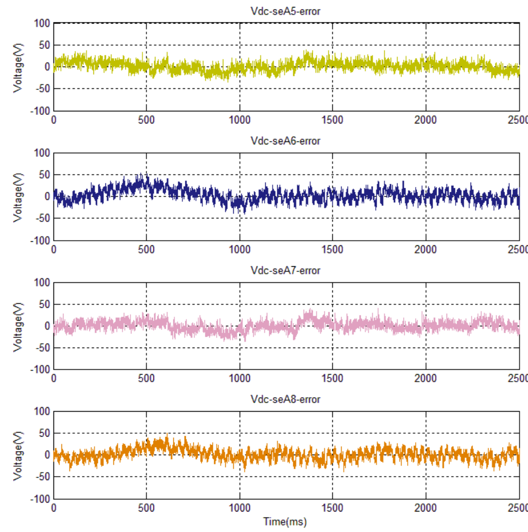

(e)

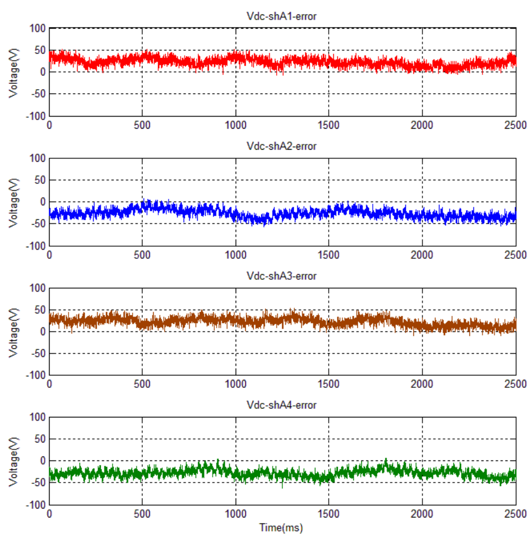

(f)

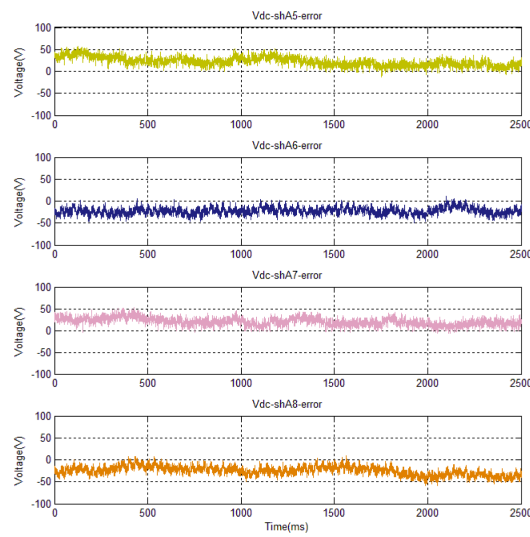

(g)

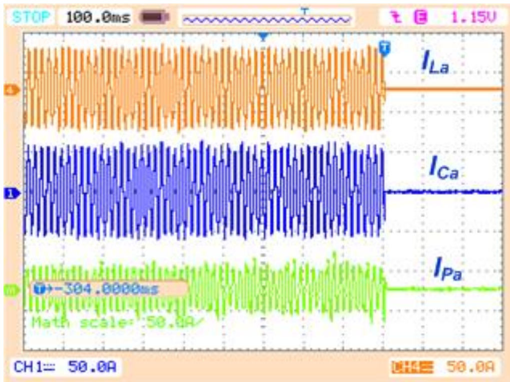

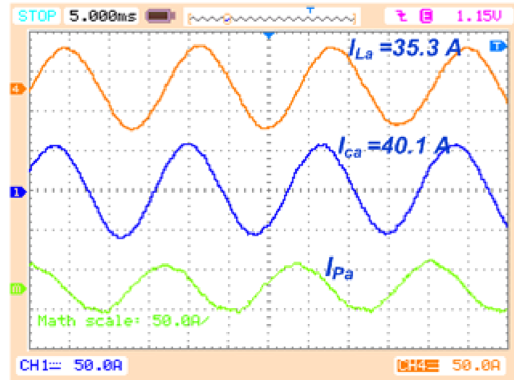

(a) (b)

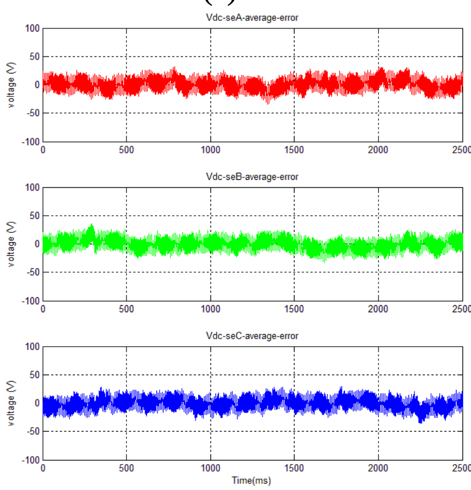

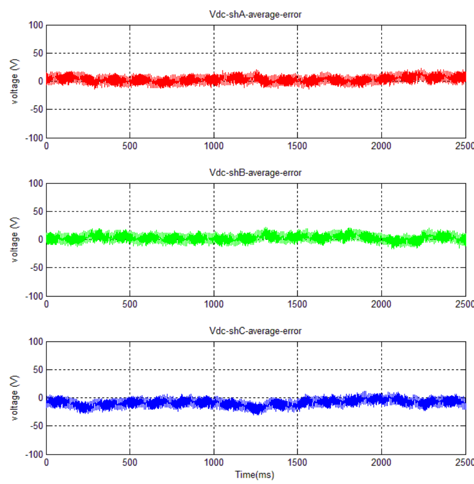

(c) (d)

Figure 4-17 Experimental waveforms of UPFC running in operating point 2: phase angle difference θ is controlled to 7°. (a). Transmission line current I_{La}, sending-end current I_{Ca} and shunt current I_{pa} (b). Zoom in waveform for I_{La}, I_{Ca} and I_{pa}; (c). Average series CMI dc link voltage error; (d). Average shunt CMI dc link voltage error (e). Series CMI individual module 1-4 dc link voltage error; (f). Series CMI individual module 5-8 dc link voltage error; (g). Selective shunt CMI individual module 1-4 dc link voltage error; (h). Selective shunt CMI individual module 5-8 dc link voltage error.

Figure 4-17 (cont'd)

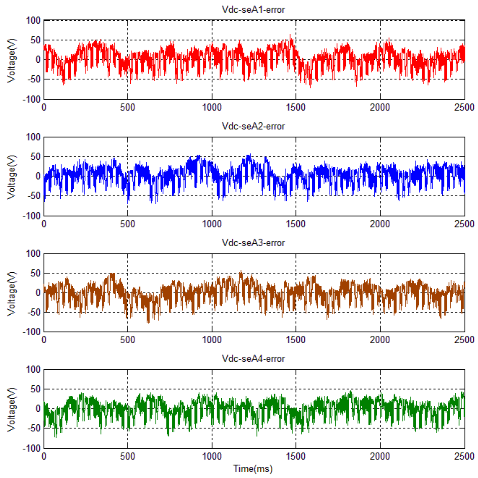

(e)

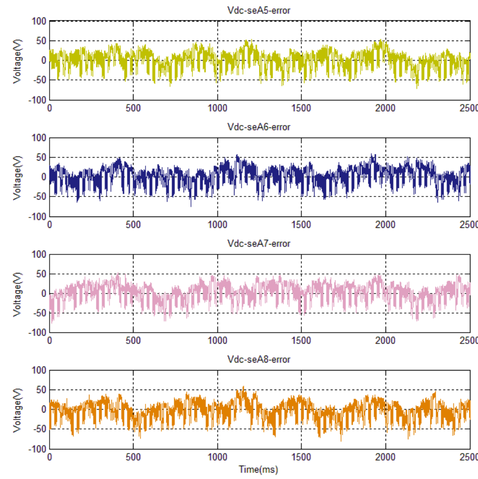

(f)

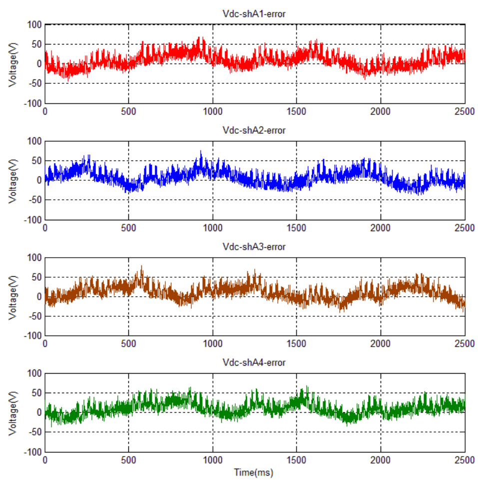

(g)

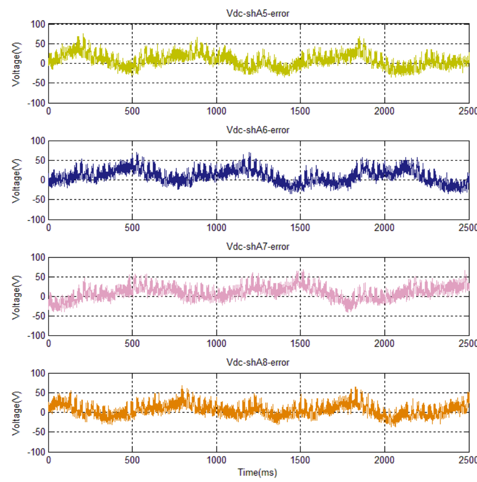

(h)

4.6 Conclusion

The innovative transformer-less UPFC demonstrated in this chapter have enormous technological and economic impacts on controlling the routing of energy over the existing power. The enabling technology of modularity, scalability makes it easy installation anywhere in the existing grid. The transformer-less UPFC helps maximize/optimize energy transmission over the existing grids to minimize the need for new transmission lines. Resulting increase in the transfer capability of the grid, combined with the controllability and speed of operation of the devices, will enable increased penetration of renewables and demand response programs. Reducing transmission congestion and increasing dynamic rating of transmission assets.

So far, modeling, control, analysis and one of the application of transformer-less UPFC have been demonstrated. Next chapter will present another application of transformer-less UPFC in congested grid.

CHAPTER 5 Application of Transformer-less UPFC for Power Flow Control of Congested Grid

In this chapter, application of transformer-less UPFC for power flow control of congested grid is presented. The proposed transformer-less UPFC is based on two cascaded multilevel inverters (CMIs). As is well known, the real power flow between two generators is mainly determined by their phase difference. If the phase difference between the sending-end generator and receiving-end customer is small, the transmission line will suffer from the transmission congestion. Several strategies have been investigated to solve the problems, such as upgrading existing overhead lines, installation of underground cables, installation of FACTS and HVDC device, etc. However, their benefits and drawbacks vary from each other. In this chapter, application of transformer-less UPFC to release power flow congestion is presented. The transformer-less UPFC can be directly installed with the existing overhead line and offers several advantages over the aforementioned traditional technologies, such as transformer-less, light weight, high efficiency, high reliability, low cost, and extremely fast dynamic response. Furthermore, experimental results based on 13.8-kV/ 2-MVA transformer-less UPFC prototype are shown to validate the theoretical analysis.

5.1 Introduction

The modern power grid is a complicated mesh structure and sometimes suffered from severe congestions [74]. Consequently, the need for transmission capacity is roaring and thus causes the transmission grid facing with serious challenges. Generally, two approaches have been considered for increasing power flow through existing assets: building new lines and installing hardware devices. Specifically, several technologies have been considered, installation of AC overhead lines [94], uprating of existing assets [8], installation of energy storage [95], installation of underground cables [96], installation of flexible alternating current transmission system (FACTS) devices [61, 97-100], installation of high-voltage direct current (HVDC) line [90, 101, 102], etc. Their benefits and drawbacks have been thoroughly investigated in [103].

In practice, power transmission lines carry power from generating plants to local substations, where they are connected to neighborhood distribution lines. Transmission lines can be built overhead on towers, or they can be buried underground (similarly for submarine cables under bodies of water), this is known as hybrid transmission. Figure 5-1 shows a typical radial system with hybrid transmission. According to the report in [104], the overhead lines will be preferred whenever practical. However, overhead lines are sometimes impractical or infeasible, like in the vicinity of airports, sea or a national park and so forth, underground cables are usually installed. Furthermore, overhead lines also encounter technical difficulty, when the power angle between sending-end generation units and receiving-end local substations is small, the transmission overhead line will suffer from congestion and cannot carry enough power as expected. Power will take the path of least impedance, as in the system shown in Figure 5-1, more power will flow along the underground cable. This is because underground cables have less impedance to power flow.

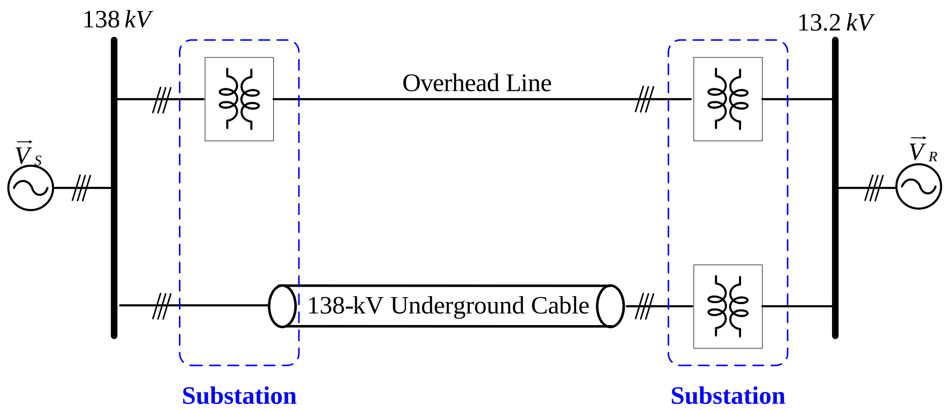

Figure 5-1. Radial system from generation to distribution/load center by overhead line and underground cable.

Although the benefits brought by underground cables, it is more costly to install than its counterparts, overhead lines. The largest cost component in underground cables is materials, such as cables and insulating fluid. Furthermore, underground cable needs large line charging current due to its large capacitance. The capacitance is far higher than the overhead line since the wires are closer to each other as well as closer to the earth. This limits the use of underground cable in long transmission line and in practice. Usually, the underground cable has a physical length limitation of 50 miles or so [105].

One of the solutions to large capacitance of long transmission underground cable is moving from ac to dc transmission, since DC cables do not suffer from problems as AC cables. However, this will add additional cost to the already expensive underground transmission, primarily a DC converter station, mostly frequently used, a HVDC station. HVDC, since its first installation in 1954 between Swedish mainland and Gotland island, it has drawn attention from industry and academic, and has been considered as one of the main hardware implementation in high-voltage transmission level application. The fundamental process that occurs in an HVDC is the conversion of electrical current from AC to DC (rectifier) at the transmitting end and from DC to

AC (inverter) at the receiving end. Among which, ABB's HVDC light [101] and Siemens's HVDC plus [102] have found its application in many fields and provided profound benefits.

The transformer-less UPFC can simply control the magnitude and phase angle of the series injected voltage in real time to maintain or vary the active and reactive power flow in the transmission line to satisfy load demand and system operating conditions, i. e. independent *P/Q* control. This will provide a much flexible solution to power transmission and will be readily installed at the overhead line wherever suitable. By installing the transformer-less UPFC, this overhead line become totally controllable, thus no underground cable installation is necessary for the congestion issue consideration. A possible connection and schematic diagram is shown in Figure 5-2. This chapter presents the analysis for the new transformer-less UPFC to control bidirectional power flow along the existing assets to release transmission grid congestion. The transformer-less UPFC functionality with proposed control method is experimentally verified at 13.8 kV/ 2 MVA prototype.

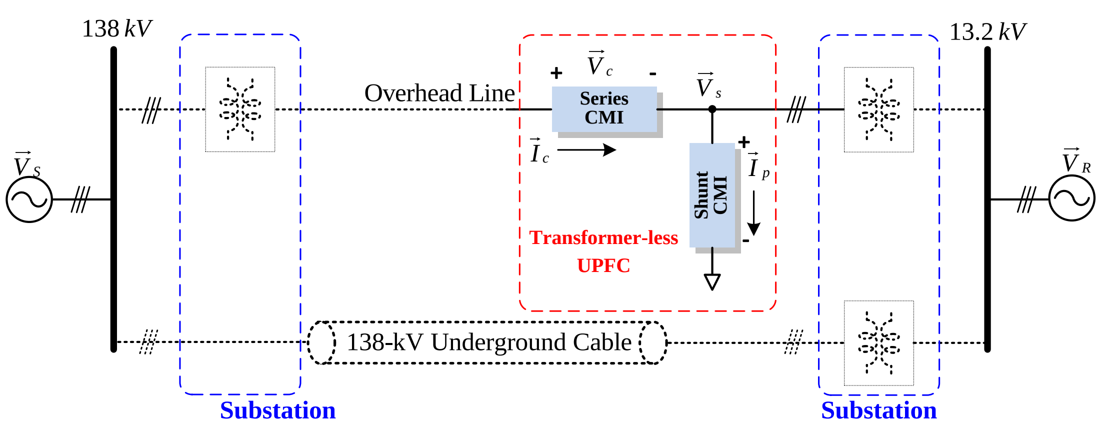

Figure 5-2 Radial system from generation to distribution with transformer-less UPFC.

5.2 Power Transfer Through Underground Cable

The underground AC cables have certain benefits, since it provides lower visibility and less affected by bad weather. It also helps to reduce outages, transmission congestion and transmission losses. There are quite different types of cables, such as cross-linked polyethylene (XLPE) cable, gas insulated lines (GIL), high temperature superconducting (HTS) cable, etc. However, costs of insulated cable and excavation are much higher than overhead construction. Besides, faults in buried underground cables take longer to locate and repair. Furthermore, underground cables are also strictly limited by their thermal capacity, which permits less overload or re-rating than overhead lines.

Underground cable has high capacitance. This may reduce their ability to provide useful power to loads beyond 50 miles [105]. One thing is that the long underground cables produce large amounts of capacitive power to the grid. This may cause reactive energy penalties according to tight regulation in some countries [106]. Another technical issue is that the capacitance and inductance may cause system resonance [107]. Thus, the implementation of underground cable needs additional reactive power compensation and active damping strategy. A schematic diagram of HVAC underground cable is shown in Figure 5-3.

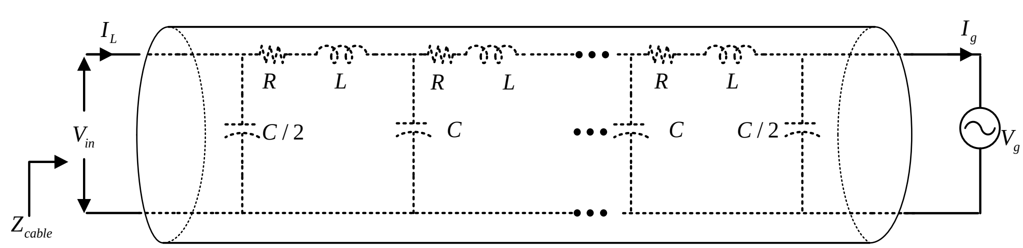

Figure 5-3 Schematic diagram of HVAC underground/submarine cable.

In order to resolve the problems with the high voltage AC cables, high-voltage DC cables have been utilized and also known as HVDC cable. Long underground DC cables can run for thousands of miles and free from resonance and capacitive power issues as their AC counterparts. However, as mentioned in the introduction of this chapter, the converter (HVDC rectifier and HVDC inverter) used in the HVDC station needs to withstand full voltage and current rating, makes it more expensive to solve the power transmission related problems. An important thing to highlight here is the reduced converter rating when using UPFC in the same application. In the same scenario, the back-to-back HVDC converter rating can be 7 times larger than the UPFC [108].

This chapter presents an alternative for the HVAC or HVDC cable when overhead line suffers from congestion, adding totally transformer-less UPFC to the existing power transmission line, thus the related power transmission problems can be easily solved in a much more economical way.

5.3 Operation Principle of the Transformer-less UPFC in Congested Grid

The transmitted active power P and reactive power Q over the line with the transformer-less UPFC can be expressed as

$$\begin{aligned} P + jQ &= \vec{V}_R \cdot \left(\frac{\vec{V}_{S0} - \vec{V}_C - \vec{V}_R}{jX_L} \right)^* \\ &= \left(-\frac{V_{S0}V_R}{X_L}\sin\delta_0 + \frac{V_C V_R}{X_L}\sin(\delta_0 - \delta) \right) \\ &+ j\left(\frac{V_{S0}V_R\cos\delta_0 - V_R^2}{X_L} - \frac{V_C V_R}{X_L}\cos(\delta_0 - \delta) \right) \end{aligned} \quad (5.1).$$

This can be considered as two parts, one is the original transmitted real power P_0 and Q_0, and the other part is introduced by the transformer-less UPFC, denoted as P_C and Q_C,

$$P + jQ = \left(\underbrace{-\frac{V_{S0}V_R}{X_L}\sin\delta_0}_{P_0} + \underbrace{\frac{V_C V_R}{X_L}\sin(\delta_0 - \delta)}_{P_C} \right) + j\left(\underbrace{\frac{V_{S0}V_R\cos\delta_0 - V_R^2}{X_L}}_{Q_0} \underbrace{-\frac{V_C V_R}{X_L}\cos(\delta_0 - \delta)}_{Q_C} \right) \tag{5.2}$$

Because both amplitude V_C and phase angle δ of the UPFC injected voltage $\overrightarrow{V_C}$ can be any values as commanded, the new UPFC provides a full controllable range of ($-V_C V_R/X_L$) to ($+V_C V_R/X_L$) for both active and reactive powers, P_C and Q_C, which are advantageously independent of the original sending-end voltage and phase angle δ_0. An example of variation of injected voltage V_c for active power flow P with the relationship of phase angle is shown in Figure 5-4.

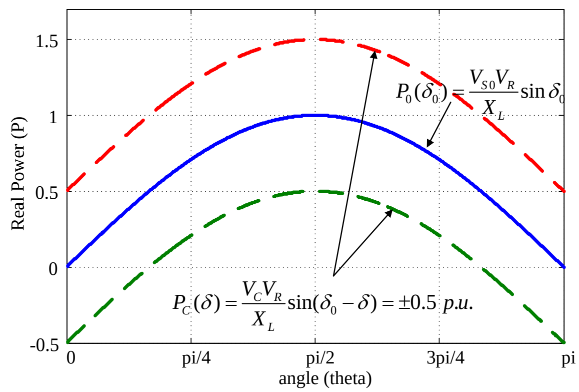

Figure 5-4 Range of transmittable real power P vs. transmission angle δ with different injected voltage V_C.

Figure 5-5 shows the schematic and experimental setup of using transformer-less UPFC in a congested power transmission grid, where $\overrightarrow{V_{S0}}$ and $\overrightarrow{V_R}$ have almost same magnitude and phase angle. This is an extreme case of power transmission grid, where the initial phase angle difference δ_0 between $\overrightarrow{V_{S0}}$ and $\overrightarrow{V_R}$ is 0°. Consequently, in such a case, there is almost no active power flow between sending and receiving end. To deal with this dilemma, the transformer-less UPFC is used to increase phase difference δ_0 for higher power flow through the transmission line.

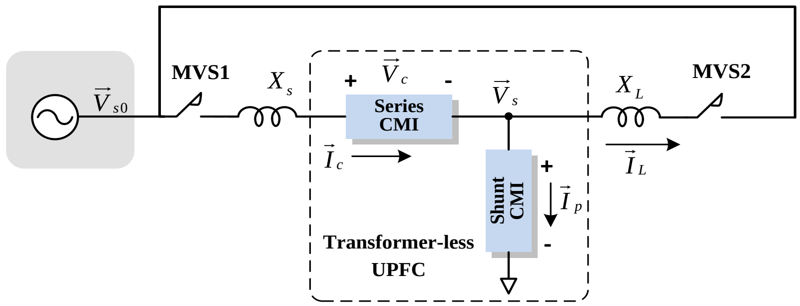

Figure 5-5. System setup of transformer-less in congested grid.

The control objective for transformer-less UPFC in this chapter is: 1) active power (i.e. power angle between V_S and V_R) regulation by the series CMI; 2) DC balance control for both CMIs (series CMI current $\vec{I_C}$ and the shunt CMI current $\vec{I_P}$ to be perpendicular to their voltages $\vec{V_C}$ and $\vec{V_S}$, respectively). Figure 5-6 shows the corresponding phasor diagram for the bidirectional power flow and the following analysis will take the positive power flow case for an example, whereas the negative power flow case can be analyzed similarly.

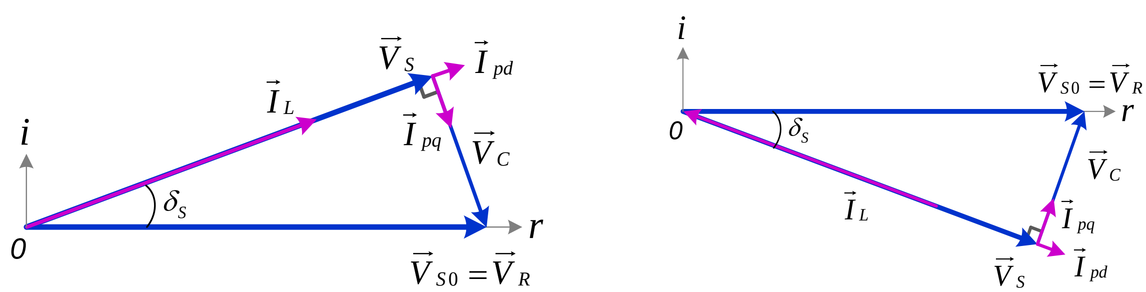

(a) (b)

Figure 5-6. Phasor diagram of transformer-less UPFC for bidirectional power flow control (a). positive power flow and (b). negative power flow.

Generally, the rating of the series CMI voltage is determined by its controllable region, or more specifically, the required power flow between sending and receiving end. Once the transmitted active power P and reactive power Q over the line with the transformer-less UPFC is given, the power angle δ_S can be calculated according to

$$P+jQ=\vec{V}_R\cdot\left(\frac{\vec{V}_S-\vec{V}_R}{jX_L}\right)^*, \vec{V}_R=1\angle(0), \vec{V}_S=V_S\angle(\delta_s)=\cos\delta_s\angle(\delta_s) \quad (5.3),$$

where symbol * represents the conjugate of a complex number, δ_S is the phase angle between new sending-end voltage $\vec{V_S}$ and receiving-end voltage $\vec{V_R}$, X_L is the equivalent transmission line impedance.

Once the power angle θ is obtained, the series CMI injected voltage $\vec{V_C}$ can be calculated as

$$\vec{V_c}=\overrightarrow{V_{s0}}-\vec{V_R}e^{j2\delta_s}=1-\cos(2\delta_s)-j\sin(2\delta_s) \quad (5.4).$$

As can be seen from (5.4), the rating of the series CMI is closely related to the power angle δ_S. The current rating $\vec{I_L}$ is determined by

$$\vec{I_L}=\frac{\vec{V}_S-\vec{V}_R}{jX_L}, \textit{where}\,\vec{V}_S=\cos\delta_s\angle(\delta_s) \quad (5.5).$$

Next, the shunt CMI in transformer-less UPFC injects current $\vec{I_P}$ to decouple the series CMI current $\vec{I_C}$ from the line current $\vec{I_L}$. In such a way, zero active power exchange to both series and shunt CMIs can be achieved, making it possible to apply the CMI with floating capacitors to the proposed transformer-less UPFC. Therefore, we have

$$\begin{cases} P_{se}=\vec{V}_C\cdot\vec{I}_C=0 \\ P_{sh}=\vec{V}_S\cdot\vec{I}_P=0 \end{cases} \quad (5.6).$$

It means the series CMI current $\vec{I_C}$ and the shunt CMI current $\vec{I_P}$ need to be perpendicular to their voltages $\vec{V_C}$ and $\vec{V_S}$, respectively, as illustrated in Figure 5-6. It is interesting that in this configuration, since I_C and I_L are almost in line with each other, the shunt current I_P is almost zero, only very small amount of I_P is needed for the purpose of dc link voltage balancing for series and shunt CMI, which will be discussed in detail in later section.

In summary, there are two critical steps for the operation of UPFC: a) calculation of injected voltage $\overrightarrow{V_C}$ for series CMI according to active/reactive power command (power angle δ_S) over the transmission line expressed in (5.4), and b) calculation of injected current $\overrightarrow{I_P}$ for shunt CMI to guarantee zero active power into both series and shunt CMIs and compensation for power loss for their dc link voltage.

5.4 Power Flow and Dc-link Voltage Control of Transformer-less UPFC

5.4.1 Power Flow and Overall DC Voltage Control

The overall control strategy of transformer-less UPFC can independently regulate the active power P and reactive Q in the line, at the same time, maintain the capacitor voltages of both CMIs at the given value. Figure 5-7 shows the overall control system. The dc link voltage control strategy is different from previous chapter due to the unique configuration in this test.

First, the upper command P^* and Q^* will decide $\delta_S{}^*$ and $I_p{}^*$ or say $\overrightarrow{V_{C0}^*}$ and $\overrightarrow{I_{p0}^*}$ for series and shunt CMI, respectively. As mentioned before, the $\overrightarrow{V_{C0}^*}$ is the voltage reference for series CMI, which is generated according to the transmission line power command (phase angle θ) as given in (5.4), while $\overrightarrow{I_{p0}^*}$ is current reference for shunt CMI, which is used to keep zero active power for both CMIs. In this case, since I_{se} and I_L are almost in line with each other, very small amount of I_p (or Q^*) is needed for the operation and its main contribution is for dc link voltage control for both shunt and series CMI.

In previous chapter, in order to control dc-link voltage with better robustness, two variables $\overrightarrow{\Delta V_C}$ and $\overrightarrow{\Delta I_P}$ were introduced for the independent dc-link voltage regulation of series CMI and shunt CMI, respectively. With the $\overrightarrow{V_{C0}^*}$ and $\overrightarrow{I_{p0}^*}$ calculated from upper P^* and Q^* command, the dc-link voltage can't be maintained due to the following three main reasons: (a) the CMIs always have a power loss, (b) the calculation error caused by the parameter deviations, (c) the error between reference and actual output. However, in this in-phase circuit configuration, the active component $\overrightarrow{\Delta V_C}$ will not help with the dc link voltage control. This is because I_{se} and I_L will always be in line with each other and $\overrightarrow{\Delta V_C}$ will always be in line with V_c thus has no contributes to the control and maintenance of series CMI dc link voltage. A modified control strategy which relies solely on active component $\overrightarrow{\Delta I_P}$ is realized in this configuration. Specifically, I_{pd} is for shunt CMI dc link voltage control and I_{pq} is for series CMI dc link voltage control. As shown in Figure 5-7, $V_{dc\_sh}^*$ and $V_{dc\_se}^*$ are dc voltage references for shunt and series CMIs, respectively; V_{dc_sh} and V_{dc_se} are the averaged dc feedback of shunt and series CMIs, respectively. For the series CMI, P_{se} is the output of overall dc-link voltage regulation loop, G_{se} is then calculated by dividing P_{se} by V_C^2 (square of *rms* value of series CMI voltage), finally ΔI_{pq} is the product of G_{se} and series CMI voltage $\overrightarrow{V_C}$. The dc-link can be balanced when P_{se} is equal to P_{loss} (total power loss of series CMI). Similarly, ΔI_{pd} is introduced for the dc-link voltage control for shunt CMI.

After getting the component of $\overrightarrow{V_{C0}^*}$ and $\overrightarrow{I_{p0}^*}$ from upper control layer and $\overrightarrow{\Delta I_P}$ for shunt and series dc link voltage control, voltage and current generation for series and shunt CMI can be obtained accordingly. For series CMI, output voltage could be directly generated from the reference $\overrightarrow{V_C^*}$ by FFM. While for shunt CMI, decoupling feedback current control is used to control output current to follow the reference current $\overrightarrow{I_P^*}$, as shown in Figure 3-4(c) [17].

5.4.2 Individual DC Voltage Control

Besides the overall dc-link voltage control present above, it is necessary to have the individual dc-link voltage control for the charge balance between the modules in the same phase. This is implemented by pulse swapping every fundamental cycle and individual phase shift method [14]. The realization of the pulse swapping from one fundamental cycle to the next fundamental cycle in a special sequence and has been detailed discussed in previous chapter. Furthermore, individual phase shift method is also included to take care of the small difference between each module and this is shown in Figure 5-8. In order to decide which modules to be charged and discharged at a specific time, the value of each individual instantaneous dc-link capacitor voltage and direction of current (current and voltage relationship) should be measured. As can be observed from Figure 5-6, for series CMI, during bidirectional power flow, series CMI current $\overrightarrow{I_C}$ is leading voltage $\overrightarrow{V_C}$; while for the shunt CMI, during positive power flow, $\overrightarrow{I_p}$ is lagging $\overrightarrow{V_S}$ and for the negative power flow, $\overrightarrow{I_p}$ is leading $\overrightarrow{V_S}$. The shifted angle $\Delta\alpha_i$ is adjusted accordingly. Consequently, each dc link is able to be controlled by slightly shifting the switching pattern. Moreover, the magnitude of this shift $\Delta\alpha_i$ is usually much smaller than α_i.

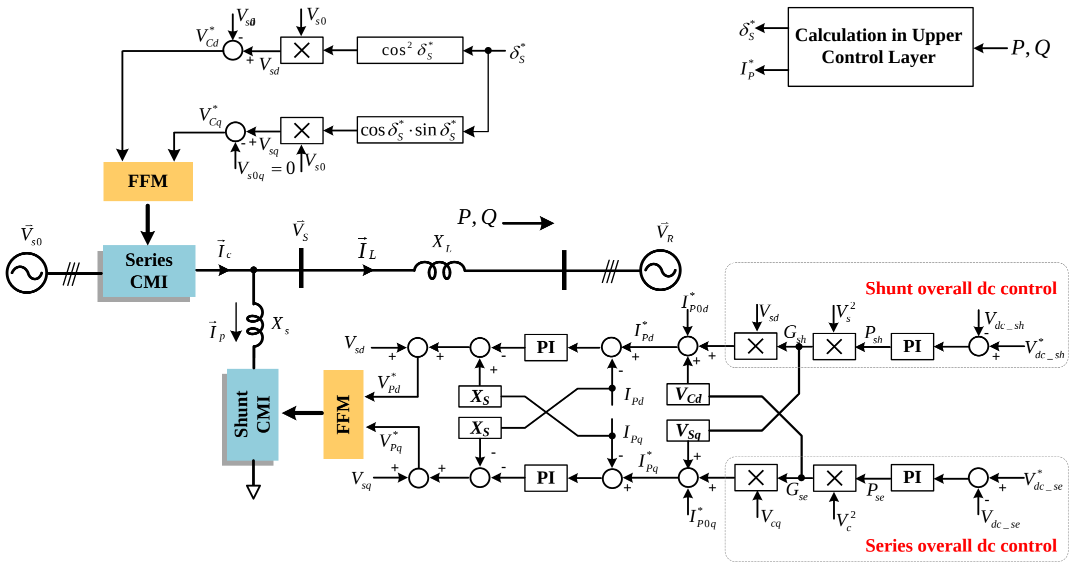

Figure 5-7. Overall control diagram for transformer-less UPFC for both power flow and dc capacitor voltage control.

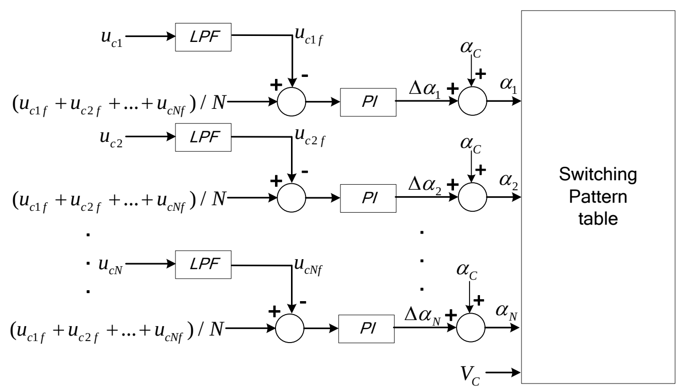

Figure 5-8. Individual dc voltage control for series/shunt CMI considering capacitor voltage unbalance between modules.

5.5 Experimental Results

5.5.1 Test system setup

A 13.8-kV/ 2-MVA transformer-less UPFC prototype has been developed to validate the UPFC to increase power flow between two grids with very limited phase difference. The test setup is the same as shown in Figure 5-5 and the main system parameter for the prototype is same as in Table 4.3. In Figure 5-5, the sending-end voltage $\vec{V}_{S0}$ and receiving-end voltage $\vec{V}_R$ are connected at same point, which means $0°$ phase difference. This is the worst case between generator and load center. The line current/power can be controlled to any desired value when a transformer-less UPFC is installed between two grids. Figure 5-9 shows the diagram for ± 1 MVA of the system compensated by UPFC. As will be discussed later, the new sending end bus voltage $\vec{V}_s$ will be varied due to the bidirectional power flow associated with transformer-less UPFC.

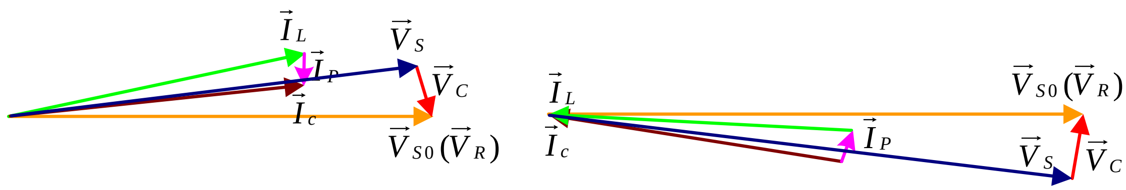

Figure 5-9. Phasor diagram for ±1 MVA power flow.

5.5.2 Bidirection power flow of transformer-less UPFC

The start-up sequence is same as shown in Figure 4-14. Initially, MVS1 in Figure 5-5 is closed while MVS2 is open. Dc link of each module is charge to about 300 V by variac. Then power supply board of each module and local DSP board will begin functioning, the communication between main DSP and local DSP is established. After that, a running signal will be given by the upper command, the system will run into inverter charge mode. In inverter charge mode, each of the dc link voltage of shunt and series CMIs will charge to 550V and 350 V, separately. After the inverter charge mode, the dc voltage maintains at its nominal value, the system is in standby status. Once the upper command of closing MVS2 is sent, the system will run into UPFC mode.

The experimental results of whole operation of UPFC for the ±1-MVA bidirectional power flow control are shown in Figure 5-10. As can be seen, very small amount of reactive power and I_{sh} is needed for the operation of transformer-less UPFC in this situation and power flow can be changed bidirectionally.

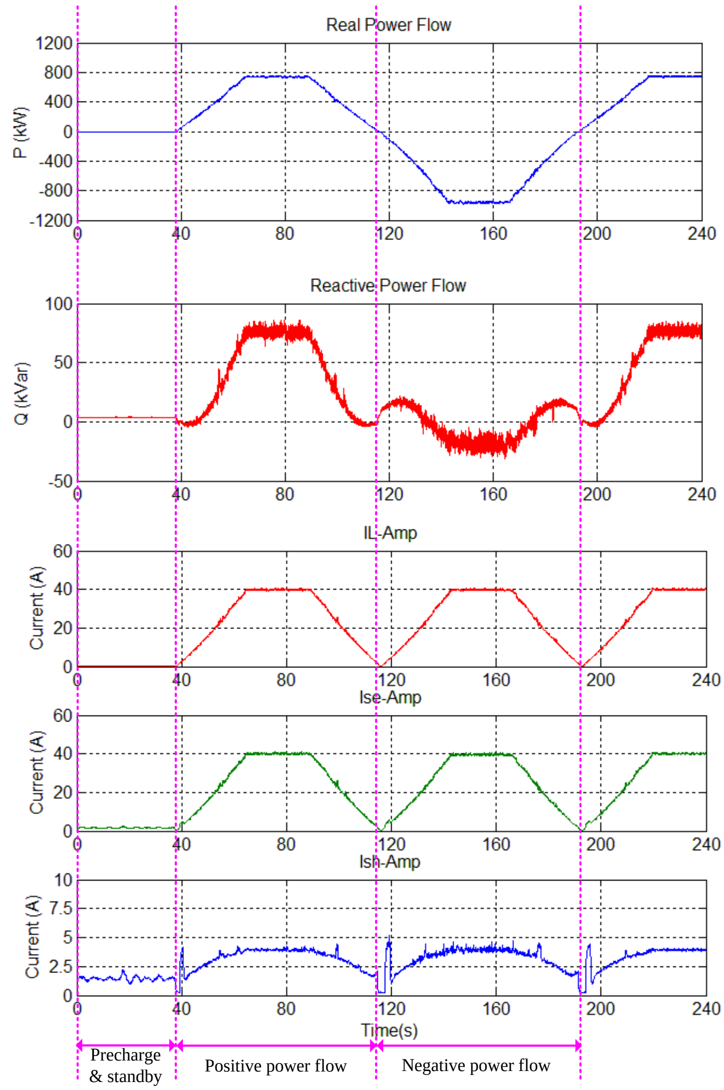

Figure 5-10. Bidirectional power flow control with transformer-less UPFC and corresponding current magnitude.

Figure 5-11 shows the steady-state experimental waveforms of UPFC running for ±1 MVA. Figure 5-11(a) shows line current I_{La} going to receiving-end, shunt CMI current I_P and inverter output voltage V_{sab}. For +1 MVA power flow, the transmitted line current I_L is 40 A and shunt current I_P is 4 A. The displayed line voltage V_{sab} is the voltage of series CMI V_{Cab} plus shunt CMI output voltage V_{Pab}. The shown voltage V_{sab} is fed into main DSP, measured at the secondary of the potential transformer (PT) with the turn ratio of 120*41: 1. The measured voltage is corresponding to the 13.8-kV line voltage. Similarly for the Figure 5-11(b), which demonstrated -1 MVA power flow.

Figure 5-12(a) to (d) are average dc link voltage for shunt and series CMIs for ±1 MVA power flow. The average series V_{dc} reference is 350 V for both cases and average shunt V_{dc} reference is 480 V and 580 V. This is due to when I_p is regulating the dc-link voltage for shunt and series CMI, the intermediate bus voltage V_s will decrease for positive power flow and rise for negative power flow. All of the changes are within ±5% of voltage variation which will meets the grid code requirement. An adaptive shunt voltage reference is utilized so that modulation index (MI) of the inverter is near unity and total harmonic distortion (THD) is lowest. As can be seen from Figure 5-12(a) and (c), the average dc link voltage of series CMI in each phase is controlled to track its reference value for both case and in Figure 5-12(b) and (d), the shunt CMI dc link voltage in each phase is tracking its adaptive voltage reference very well. From these test results, transformer-less UPFC can realize independent bidirectional power flow control along the transmission line as well as a balanced dc link voltage control.

Figure 5-13 shows a human machine interface (HMI) with the operating of transformer-less UPFC at 13.8 kV/±1 MVA. All of the parameters related to the system will be on-line demonstrated. Furthermore, phasor diagram and transmitted current will be shown dynamically and in real time.

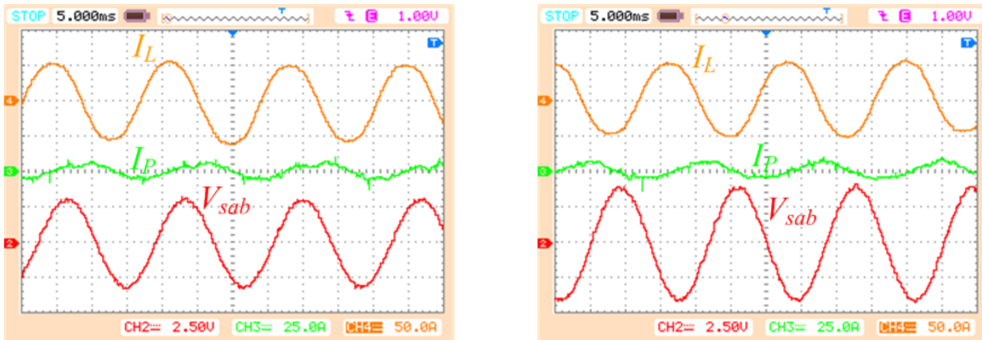

(a) (b)

Figure 5-11. Experimental waveforms of UPFC for ±1 MVA power flow (a).+ 1-MVA power flow (b).- 1-MVA power flow.

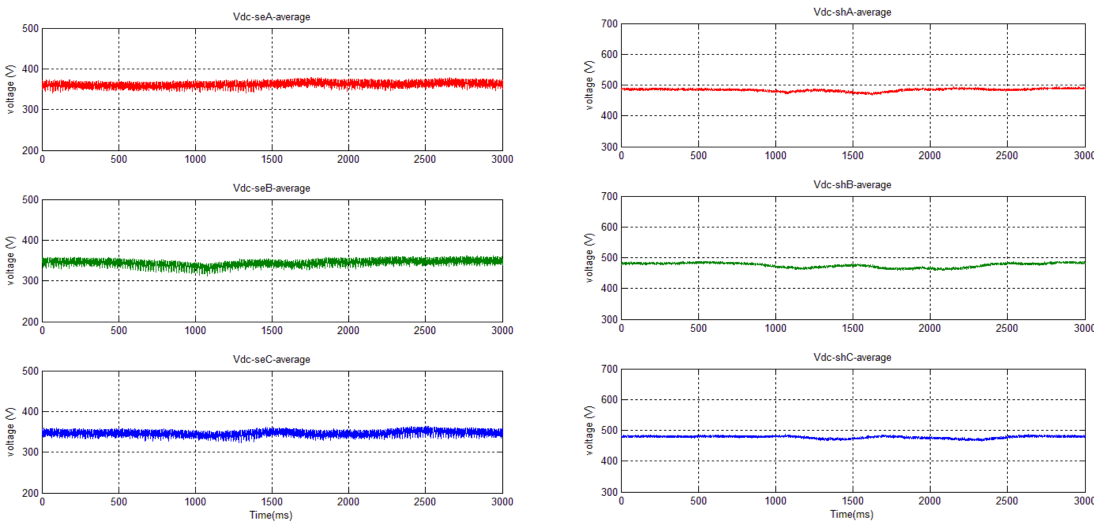

(a) (b)

Figure 5-12. Average dc link voltage for series and shunt CMI for ±1 MVA. (a) and (b) are average dc link voltage for series and shunt CMI during +1 MVA power flow (c) and (d) are average dc link voltage for series and shunt CMI during -1 MVA power flow.

Figure 5-12 (cont'd)

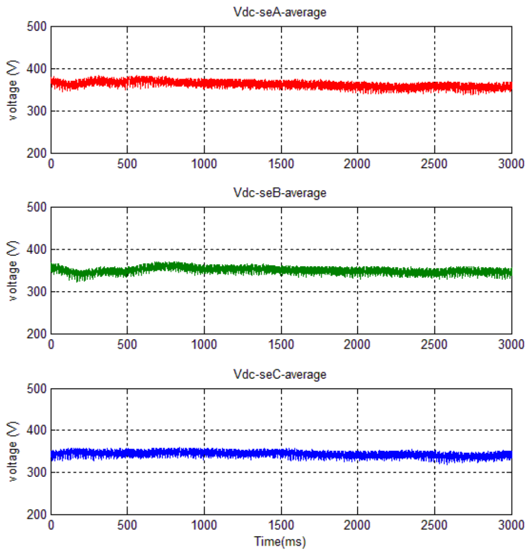

(c)

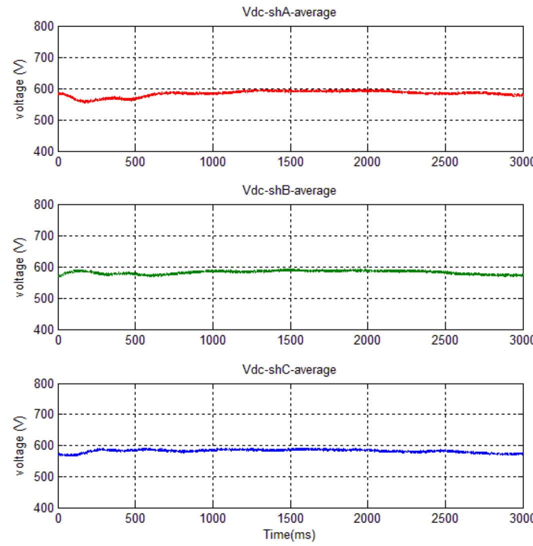

(d)

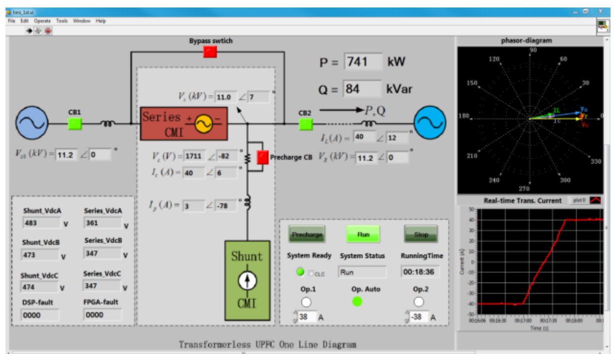

(a).

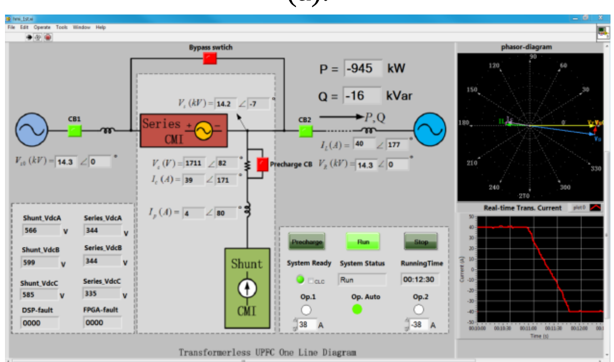

(b).

Figure 5-13. HMI for ±1 MVA positive and negative power flow with transformer-less UPFC.

Figure 5-14 shows the steady-state experimental waveforms of UPFC running for ±100 kVA. For +100 kVA power flow, the transmitted line current I_L is 5 A and shunt current I_P is still around 4 A. Similarly for Figure 5-14(b), which demonstrated -100 kVA power flow. Figure

5-15(a) to (d) are average dc link voltage for shunt and series CMIs for ±100 kVA power flow. The average series V_{dc} reference is 350 V for both cases and average shunt V_{dc} reference is 500 V and 600 V. The shunt dc link voltage reference is chosen so that MI is near unity too in this case, minimum THD can be achieved.

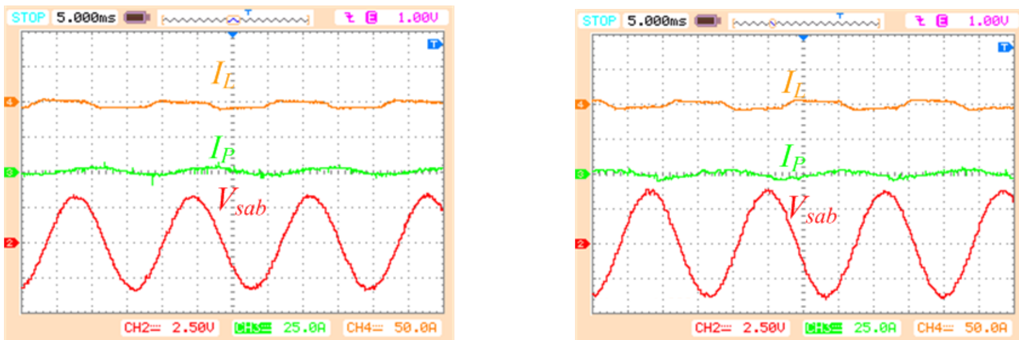

(a) (b)

Figure 5-14. Experimental waveforms of UPFC for ±100 kVA power flow (a). +100-kVA power flow (b).-100-kVA power flow.

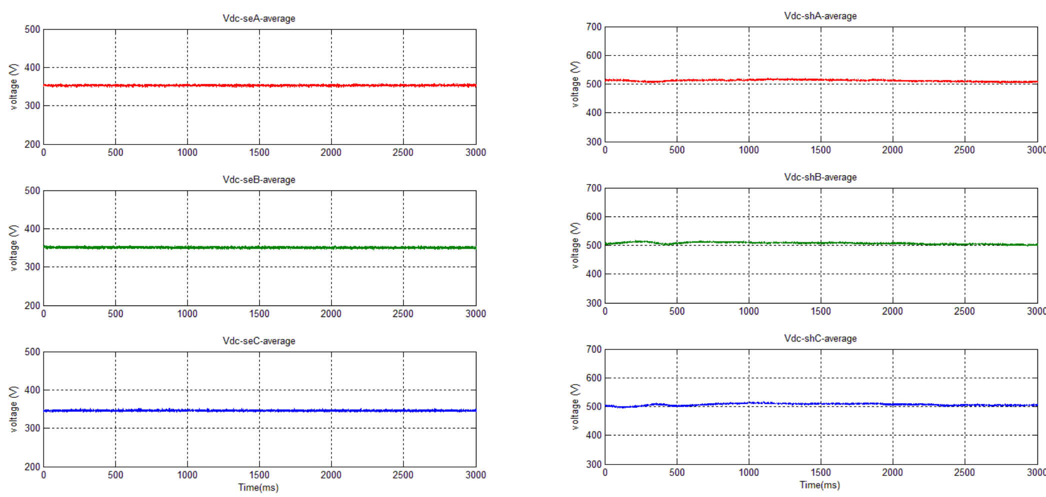

(a) (b)

Figure 5-15. Average dc link voltage for series and shunt CMI for ±100 kVA. (a) and (b) are average dc link voltage for series and shunt CMI during +100 kVA power flow (c) and (d) are average dc link voltage for series and shunt CMI during -100 kVA power flow.

Figure 5-15 (cont'd)

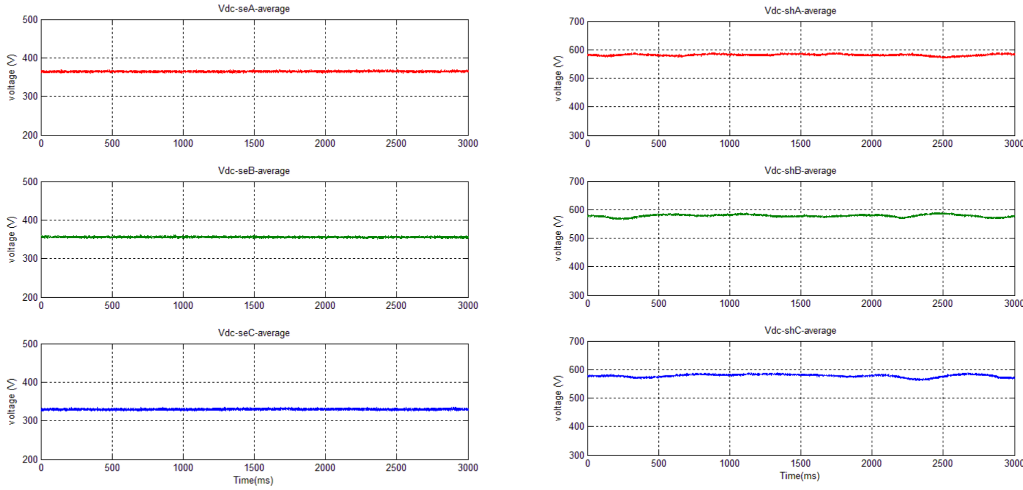

(c) (d)

In summary, the transformer-less UPFC is experimentally verified for bidirectional power flow with sending- and receiving-end bus with very limited phase angle difference (extreme case 0° phase difference). The congested and burdened transmission can be released and fully controllable with transformer-less UPFC. In the meanwhile, dc link voltage of each module can be well controlled and maintained at its reference value using the proposed control strategy. With the innovative transformer-less UPFC and its control strategy, the transmission line can carry power at its theoretical thermal limit at lowest cost and minimum transmission line construction.

5.6 CONCLUSION

The innovative transformer-less UPFC demonstrated in this chapter can increase the power flow when the phase between sending and receiving end is limited and the benefits have been discussed with underground cable power transmission. Compared with the other existing technology, transformer-less UPFC can provide more routine to the power flow at the minimum cost and smallest line construction. The demonstrated technology has enormous technological and economic impacts on controlling the routing of energy over the existing power. Furthermore, the enabling technology of modularity and scalability makes it easy installation anywhere in the existing grid. The transformer-less UPFC helps maximize/optimize energy transmission over the existing grids to minimize the need for new transmission lines. As a result, this will increase the transfer capability of the grid, combined with the controllability and speed of operation of the devices, thus will enable increased penetration of renewables and demand response programs. Finally, it will also help reduce transmission congestion and increase dynamic rating of transmission assets.

So far, detailed modeling, control, analysis and application of transformer-less UPFC have been presented. Next chapter will address an extended study of transformer-less UPFC with same hardware requirement but reduced converter rating.

CHAPTER 6 Extended Study of an Improved Transformer-less UPFC

In this chapter, an analytical analysis for an improved transformer-less unified power flow controller (UPFC) is presented. As is well known, the conventional UPFC that consists of two back-to-back inverters requires bulky and often complicated zigzag transformers for isolation and reaching high power rating with desired voltage waveforms. To overcome this problem, a completely transformer-less UPFC based on an innovative configuration of two cascade multilevel inverters (CMIs) has been proposed [35]. Although the new transformer-less UPFC offers several advantages over the traditional technology, such as transformer-less, light weight, high efficiency, low cost and fast dynamic response, its performance has been limited for some operation points and in some scenarios, the rating of the new transformer-less UPFC suffers a lot. In light of this, an improved transformer-less UPFC is proposed in this chapter. The benefits of the improved UPFC include, besides the advantages of transformer-less UPFC already possessed, same functionality of original structure, no more hardware needed, more flexible operation and less converter rating. This chapter focuses on rating analysis, modeling and control for this new transformer-less T-shape UPFC (TUPFC).

6.1 Introduction

The transformer-less UPFC has significant advantages over the traditional UPFC such as highly modular structure, light weight, high efficiency, high reliability, low cost, and a fast dynamic response. Its modeling, control and application issues have been detailed discussed in previous chapters.

However, as have been discussed in [35], the transformer-less UPFC exists some operation limits and in some scenarios, the shunt CMI will have huge injection current. One of the suggested solution, from control perspective, in [35] is releasing the reactive power restriction (allow $Q_c \neq 0$), or paraphrase, the intermediate bus voltage restriction along the transmission line. The introduced controllable reactive power (Q_c) will minimize the required shunt CMI current rating and series CMI voltage rating.

This chapter presents another solution from topology point of view and even less converter rating is required. This is known in this chapter as transformer-less T-shape UPFC (TUPFC). The circuit configuration and phasor diagram is shown in Figure 6-1. The improved transformer-less T-shape UPFC (TUPFC) consists of three CMIs. One is series CMI1, which is directly connected in series with transmission line near the sending-end bus; the shunt CMI is connected in parallel to the sending end after the series CMI1. Finally, the series CMI2 is series-connected with the transmission line near the receiving-end bus. Since the elimination of the common dc bus, the connection of the system is more flexible. If we assume series CMI's rating in transformer-less UPFC as shown in Figure 3-2 is equal to the sum of series CMI1 plus CMI2 in Figure 6-1, the total converter hardware requirement of the new transformer-less TUPFC is the same as the conventional one. Therefore, no more hardware is needed for the new configuration. Furthermore, the new improved transformer-less TUPFC offers more control freedom and can thus reduce the total converter rating of the system.

This chapter presents the analytical analysis and dynamic control for the new transformer-less UPFC. Future work involves verification of the new improved transformer-less TUPFC functionality with proposed control method at 13.8-kV/2-MVA setup, and both the steady-state and dynamic responses results is expected to demonstrate.

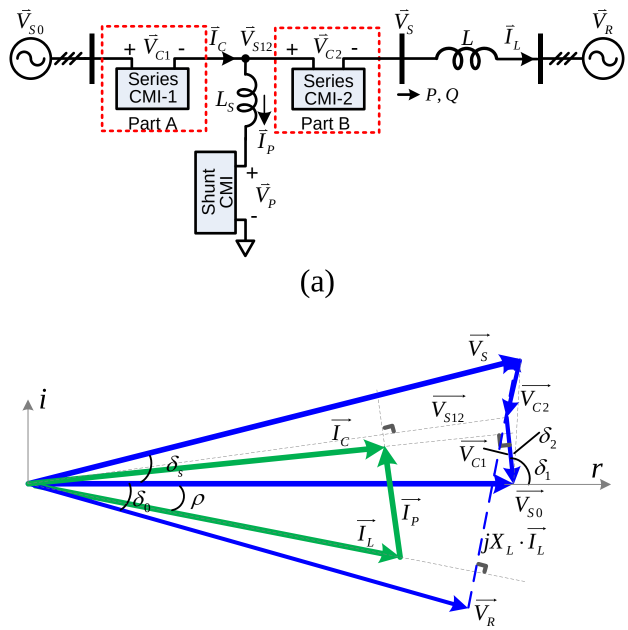

(a)

(b)

Figure 6-1 Improved transformer-less UFPC, (a) System Configuration of improved transformer-less UPFC , (b) Phasor diagram of the transformer-less UPFC.

Table 6.1 Main System Parameters for 13.8-kV T-shape UPFC Prototype.

Parameters	**Value**
System power rating	2 MVA
V_{s0} rms	13.8 kV
Max series CMI current, I_C *rms*	84 A
Max shunt CMI current, I_P *rms*	42 A
V_{dc} (Shunt)	600 V
V_{dc} (Series)	600 V
H-bridge capacitance	2350 μF
No. of H-bridges per phase (Shunt)	20
No. of H-bridges per phase (Series CMI-1)	4
No. of H-bridges per phase (Series CMI-2)	4

6.2 Operation Principle of the Improved Transformer-less TUPFC

With the unique configuration of the series and shunt CMIs, the transformer-less TUPFC has some new features:

1) Unlike the conventional back-to-back dc link coupling, the transformer-less TUPFC requires no transformer, thus it can achieve low cost, light weight, small size, high efficiency, high reliability, and fast dynamic response;

2) The shunt inverter is connected parallel in between the two series inverters CMI1 and CMI2, forms a configuration like a T-shape, which is distinctively different from the traditional UPFC. Each CMI has its own dc capacitor to support dc voltage;

3) There is no active power exchange between the three CMIs and all dc capacitors are floating;

4) The new TUPFC uses modular CMIs and their inherent redundancy provides greater flexibility and higher reliability.

6.2.1 Steady-State Models of TUPFC System

Due to the unique system configuration, the basic operation principle of the transformer-less TUPFC is quite different from conventional UPFC. Figure 6-1 shows the phasor diagram of the improved transformer-less TUPFC, where $\vec{V}_{S0}$ and $\vec{V}_R$ are the original sending-end and receiving-end voltage, respectively. Here, $\vec{V}_{S0}$ is aligned with real axis, which means phase angle of $\vec{V}_{S0}$ is zero. The series CMI1 and CMI2 is controlled to corporately generate a desired voltage

$\vec{V}_C$ for obtaining the new sending-end voltage $\vec{V}_S$, which in turn, controls active and reactive power flows over the transmission line. Meanwhile, the shunt CMI injects a current $\vec{I}_P$ to the new sending-end bus to make zero active power into three CMIs, i.e., to make the series CMI1 current $\vec{I}_C$, CMI2 current $\vec{I}_L$ and the shunt CMI current $\vec{I}_P$ be perpendicular to their voltages $\vec{V}_{C1}$, $\vec{V}_{C2}$ and $\vec{V}_{S12}$, respectively. As a result, both series and shunt CMIs only need to provide the reactive power. In such a way, it is possible to apply the CMIs to the transformer-less TUPFC with floating dc capacitors for H-bridge modules.

With the above mentioned restrictions, we have to make

$$\vec{V}_{S12} \cdot \vec{I}_P \equiv 0 \;\; \vec{V}_{C1} \cdot \vec{I}_C \equiv 0 \;\; \vec{V}_{C2} \cdot \vec{I}_L \equiv 0 \tag{6.1}$$

The transmitted active power *P* and reactive power *Q* over the line with the transformer-less UPFC can be expressed as

$$\begin{aligned} P + jQ &= \vec{V}_R \cdot \left(\frac{\vec{V}_{S0} - \vec{V}_{C1} - \vec{V}_{C2} - \vec{V}_R}{jX_L} \right)^* \\ &= \left(-\frac{V_{S0} V_R}{X_L} \sin\delta_0 + \frac{V_{Ceq} V_R}{X_L} \sin(\delta_0 - \delta^{'}) \right) \\ &\quad + j\left(\frac{V_{S0} V_R \cos\delta_0 - V_R^2}{X_L} - \frac{V_{Ceq} V_R}{X_L} \cos(\delta_0 - \delta^{'}) \right) \end{aligned} \tag{6.2}$$

where $V_{Ceq} = \sqrt{V_{C1}^2 + V_{C2}^2 - 2V_{C1}V_{C2}\cos\left(\frac{\pi}{2} - \rho - \delta_1\right)}$, $\delta^{'} = \delta_1 - \delta_2$, $\delta_2 = \arcsin\left(\frac{\sin\left(\frac{\pi}{2} - \rho - \delta_1\right) \cdot V_{C2}}{\sqrt{V_{C1}^2 + V_{C2}^2 - 2V_{C1}V_{C2}\cos\left(\frac{\pi}{2} - \rho - \delta_1\right)}} \right)$ symbol * represents the conjugate of a complex number; δ_0 is the phase angle of the receiving-end voltage $\vec{V}_R$; $\vec{V}_{Ceq}$ is the equivalent injected voltage of series CMI1 plus series CMI2; $\delta^{'}$ is the phase angle of the equivalent series CMI injected voltage $\vec{V}_{Ceq}$; X_L is the equivalent transmission line impedance. The original active and reactive powers, P_0 and Q_0 with the uncompensated system (without the UPFC, or V_{Ceq}=0) are

$$\begin{cases} P_0 = -\dfrac{V_{S0}V_R}{X_L}\sin\delta_0 \\ Q_0 = \dfrac{V_{S0}V_R\cos\delta_0 - V_R^2}{X_L} \ . \end{cases} \tag{6.3}$$

The net differences between the original (without the UPFC) powers expressed in equation (6.2) and the new (with the UPFC) powers in equation (6.1) are the controllable active and reactive powers, P_C and Q_C by the transformer-less UPFC, which can be expressed as

$$\begin{cases} P_C = \dfrac{V_{Ceq}V_R}{X_L}\sin(\delta_0 - \delta^{'}) \\ Q_C = -\dfrac{V_{Ceq}V_R}{X_L}\cos(\delta_0 - \delta^{'}) \ . \end{cases} \tag{6.4}$$

Because both amplitude V_{Ceq} and phase angle $\delta^{'}$ of the UPFC injected voltage $\vec{V}_{C1}$ and $\vec{V}_{C2}$ can be any values as commanded, the new UPFC provides a full controllable range of $\left(-V_{Ceq}V_R/X_L\right)$ to $\left(+V_{Ceq}V_R/X_L\right)$ for both active and reactive powers, P_C and Q_C, which are advantageously independent of the original sending-end voltage and phase angle δ_0. In summary, equations (6.2) to (6.4) indicate that the new transformer-less TUPFC has the same functionality as the conventional UPFC.

6.2.2 Dynamic Models of UPFC System

The models for the improved transformer-less UPFC are based on synchronous (dq) reference frame. The phase angle of original sending-end voltage V_{s0} is obtained from a digital phase-locked loop (PLL), which is used for abc to dq transformation.

The dynamic models for the whole system shown in Figure 6-1 (a) will be divided into several parts. Firstly, we can get the dynamic model from the new sending-end bus to sending-end bus

$$\begin{cases} V_{Sd} = V_{Rd} - X \cdot I_{Lq} + L\dfrac{d}{dt}I_{Ld} \\ V_{Sq} = V_{Rq} + X \cdot I_{Ld} + L\dfrac{d}{dt}I_{Lq} \end{cases} \tag{6.5}$$

Since the new sending-end voltage v_s is equal to original sending-end voltage v_{s0} minus series CMI1 and CMI2 injected voltage v_{c1} and v_{c2}, thus we have

$$\begin{cases} V_{C2d} = V_{Sd} - V_{S12d} \\ V_{C2q} = V_{Sq} - V_{S12q} \end{cases} \tag{6.6}$$

and

$$\begin{cases} V_{C1d} = V_{S12d} - V_{S0d} \\ V_{C1q} = V_{S12q} - V_{S0q} \end{cases} \tag{6.7}$$

Furthermore, the model from the new sending-end to shunt CMI is

$$\begin{cases} V_{Pd} = V_{S12d} - X_S \cdot I_{Pq} + L_S\dfrac{d}{dt}I_{Pd} \\ V_{Pq} = V_{S12q} + X_S \cdot I_{Pd} + L_S\dfrac{d}{dt}I_{Pq} \end{cases} \tag{6.8}$$

The current relationship for the three CMIs is

$$\begin{cases} I_{Ld} = I_{Cd} + I_{Pd} \\ I_{Lq} = I_{Cq} + I_{Pq} \end{cases} \tag{6.9}$$

The restriction for the reactive power for the three CMIs can be expressed in dq reference frame as

$$(V_{Sd}-V_{C2d})\cdot I_{Pd}+(V_{Sq}-V_{C2q})\cdot I_{Pq}=0 \quad (6.10).$$

$$k_1V_{C2d}(I_{Ld}-I_{Pd})+k_2V_{C2q}(I_{Lq}-I_{Pq})=0 \quad (6.11).$$

$$V_{C2d}I_{Ld}+V_{C2q}I_{Lq}=0 \quad (6.12).$$

where, $V_{c1d}=k_1*V_{c2d}$ and $V_{c1q}=k_2*V_{c2q}$.

$$k_1V_{C2d}I_{Ld}-k_2V_{C2d}I_{Lq}=\left[k_1V_{C2d}-\frac{k_2V_{C2q}(V_{Sd}-V_{C2d})}{V_{Sq}-V_{C2q}}\right]\cdot I_{pd} \quad (6.13).$$

$$I_{Pq}=-\frac{V_{Sd}-V_{C2d}}{V_{Sq}-V_{C2q}}\cdot I_{Pd} \quad (6.14).$$

From the above equations, all of the parameters in improved transformer-less UPFC can be obtained once the desired P^* and Q^* is given.

In summary, there are two critical steps for the operation of UPFC: a) calculation of injected voltage $\vec{V}_{C1}$ and $\vec{V}_{C2}$ for series CMIs according to active/reactive power command over the transmission line, and b) calculation of injected current $\vec{I}_P$ for shunt CMI to guarantee zero active power into both series and shunt CMIs.

6.3 Converter Rating Comparison Between Two Transformer-less UPFC

The operation of two transformer-less UPFC will be given in this section. The main purpose of a UPFC is to control active power flow, while maintaining reactive power flow minimal over long distance lines. Thus, reactive power flow is usually compensated locally near the receiving end. If we restrict the voltage rating along the transmission line (example. 1 pu) for all the bus, the current rating could be huge according to analytical analysis in [35]. An example of this operation range is shown in Figure 6-2.

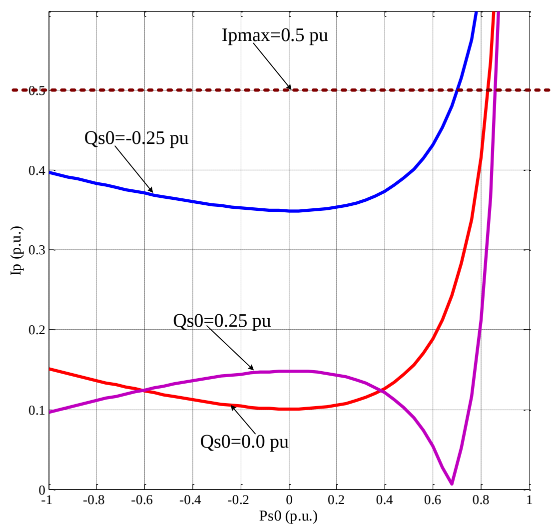

Figure 6-2 The relationship between shunt CMI Current I_p and the original power over the transmission line with equipment constraint (I_{pmax}=0.5 pu) and voltage constraint (Q_c=0).

As can be seen from Figure 6-2, the original transformer-less UPFC has limited operation especially the original active is already large (>0.6 pu). An effective way to get rid of this operation limitation is by changing the controllable reactive power operation range, in other words, make the intermediate voltage V_s and V_{s12} varied within a certain limitation. Figure 6-3 shows the operation of the original transformer-less UPFC if the intermediate bus has a changing magnitude with ±10%.

Whereas, if the new improved transformer-less UPFC is employed, an even lower shunt current can be obtained. Owing to the one more control freedom brings about by series CMI1 and CMI2. An objective function is utilized to achieve minimum shunt current thus can get minimum total converter ratings.

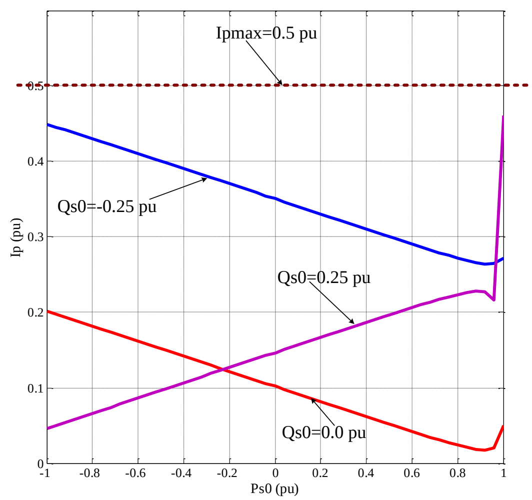

Figure 6-3 The relationship between shunt CMI Current I_p and the original power over the transmission line with equipment constraint (I_{pmax}=0.5 pu) and (Q_c=0.2 pu).

As can be seen from Figure 6-4, the current rating for the shunt CMI is significantly reduced. Figure 6-5-Figure 6-9 shows the comparison between original transformer-less UPFC and improved T-shape transformer-less UPFC. The series converter rating is almost the same while the total converter rating is reduced.

It should be noted that the new configuration will not influence the series CMI rating and it is advantageously small because it is mainly determined by the line impedance and original real power flow. For example, 0.1 pu impedance line requires only 0.1 pu series voltage even for a 1-pu net power change. So, even for the worse case, P_0 change from -1pu to 1pu, around 0.2 pu series voltage compensation is enough. However, in order to support the operation of the transformer-less UPFC, for the reactive power limitation, the shunt CMI in some scenario is huge value but this can be well solved with the help of new configuration of T-shape transformer-less UPFC.

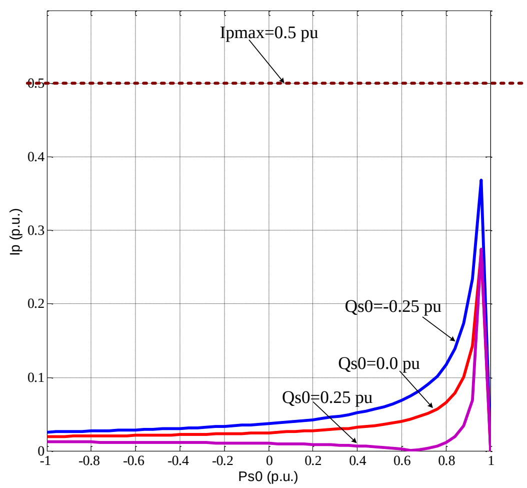

Figure 6-4 The relationship between shunt CMI Current I_p and the original power over the transmission line with T-shape transformer-less UPFC equipment constraint (I_{pmax}=0.5 pu) and (Q_c=0 pu).

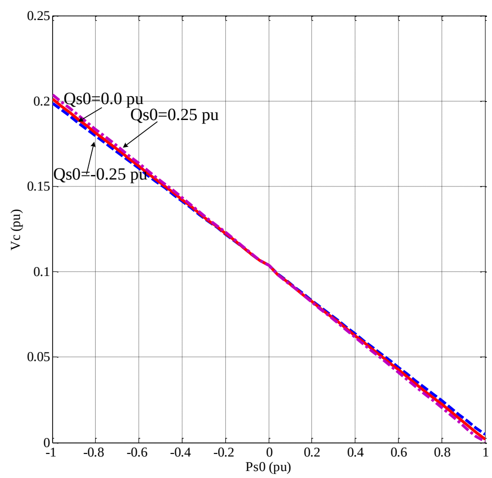

Figure 6-5 The relationship between series CMI Voltage V_C and the original power over the transmission line with equipment constraint (V_{Cmax}=0.5 pu).

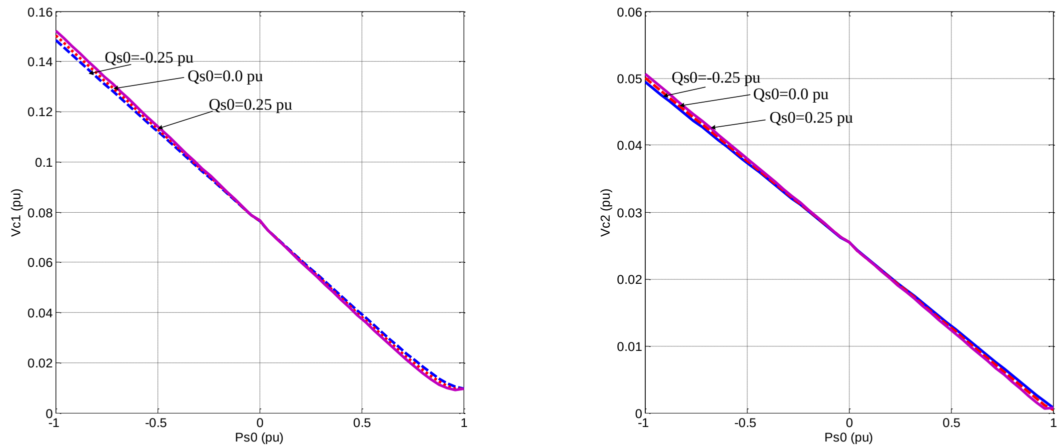

Figure 6-6 The relationship between series CMI Voltage V_{C1} and V_{C2} with the original power over the transmission line with equipment constraint (V_{Cmax}=0.5 pu).

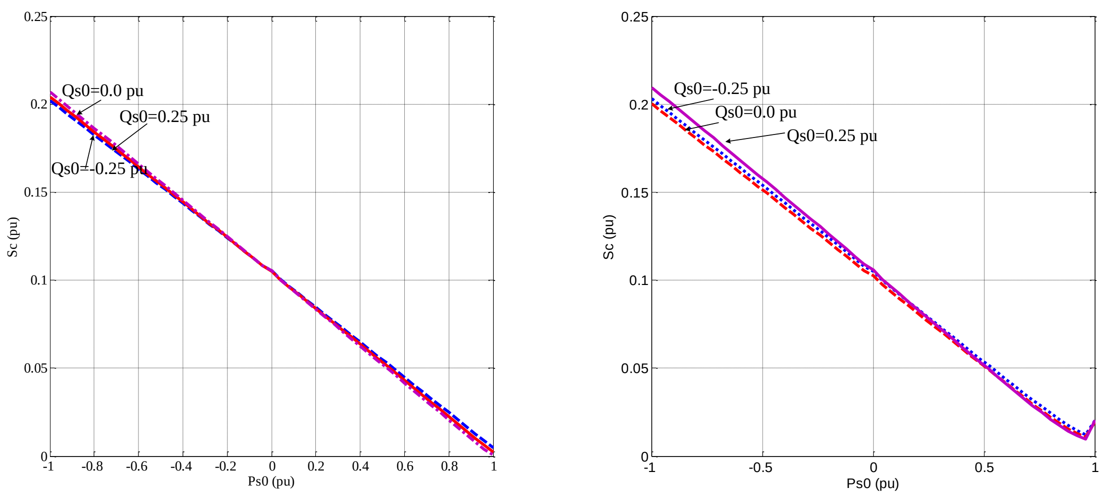

Figure 6-7 The relationship between series converter rating and the original power over the transmission line with equipment constraint (I_{Cmax}=2 pu and V_{Cmax}=0.5 pu).

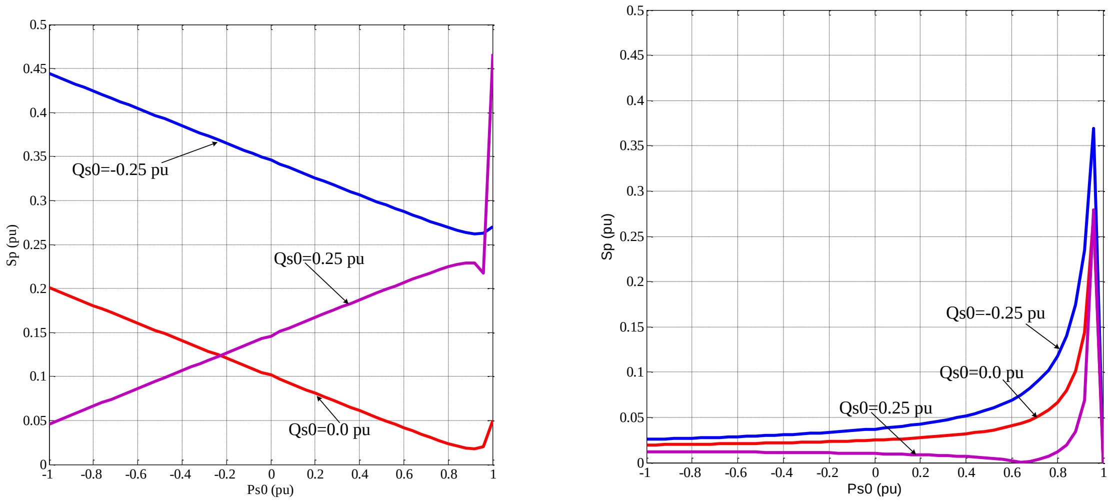

Figure 6-8 The relationship between shunt converter rating and the original power over the transmission line with equipment constraint (I_{pmax}=0.5 pu and V_{pmax}=1.2 pu).

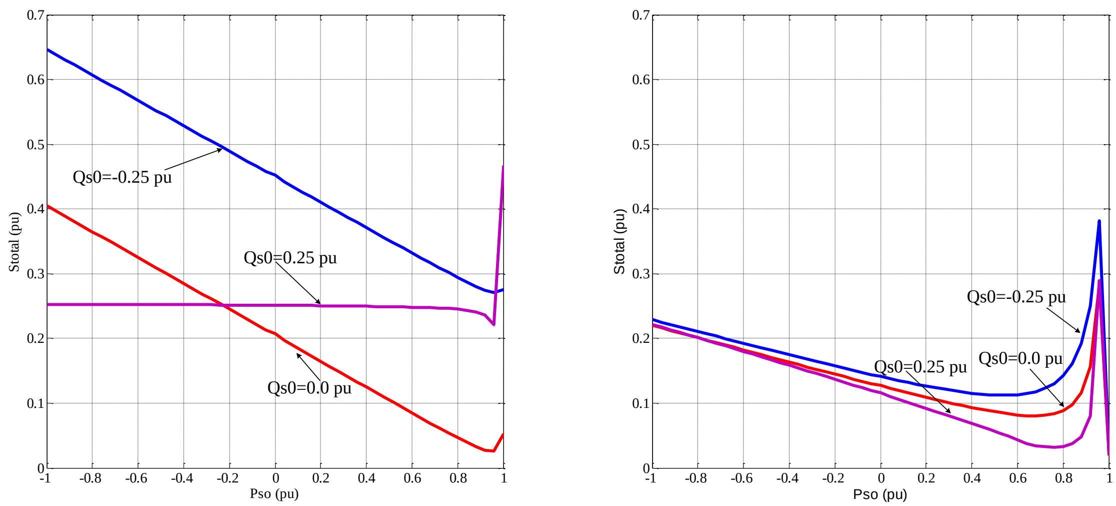

Figure 6-9 The relationship between series converter rating and the original power over the transmission line with equipment constraint (I_{Cmax}=2 pu, V_{Cmax}=0.5 pu, I_{pmax}=0.5 pu and V_{pmax}=1.2 pu).

6.4 Conclusion

This chapter present a modulation and control method for an improved T-shape transformer-less UPFC, which has the following features: 1) reduced shunt current rating and reduced total converter rating compared to original transformer-less UPFC 2) All UPFC functions, such as voltage regulation, line impedance compensation, phase shifting or simultaneous control of voltage, impedance, and phase angle, thus achieving independent active and reactive power flow control over the transmission line. The transformer-less UPFC with proposed modulation and control can be installed anywhere in the grid to maximize/optimize energy transmission over the existing grids, reduce transmission congestion and enable high penetration of renewable energy sources.

CHAPTER 7 Conclusion

Multilevel inverter is a promising next generation inverter especially for utility application. The proposed structure with its associated control strategy, can totally eliminate bulky transformer used in transmission level and distribution level systems. Power loss, size, and cost of the device will be tremendously reduced and efficiency, dynamic response will be improved. Furthermore, among the existing multilevel inverter topologies, cascaded multilevel inverter (CMI) is best suitable for power system application and easiest for large industry modularized design. All of the above mentioned benefits of CMI based structure will greatly increase the flexibility in the design, manufacture and maintenance.

The major contribution of this dissertation is to bring a novel structure of totally transformer-less UPFC and its application to solve real-world problems. Its modeling, digital control and converter rating analysis have been thoroughly checked and discussed.

7.1 Contributions

1. A virtual inertia control (VIC) of cascaded multilevel inverter (CMI) based STATACOM is introduced. The proposed method can provide competitive inertial energy response for frequency regulation. The provided energy is comparable to synchronous condenser (SC) in traditional synchronous generator (SG) application as well as synthetic inertia control (SIC) for renewable energy integration;
2. A modulation and control method for the transformer-less UPFC is introduced. The innovative transformer-less UPFC with its effective control strategy can realize power

flow control, dc link voltage balancing, low THD and fast dynamics. Owing to the benefits of the innovative topology of transformer-less UPFC, it is able to be installed anywhere in the grid to maximize/optimize energy transmission over the existing grids, reduce transmission congestion and enable high penetration of renewable energy sources;

3. Application of transformer-less UPFC to interconnect two synchronous grids is demonstrated. Theoretical analysis and its effective control strategy has been verified at 13.8 kV system. It is notable that UPFC can be used in the grid interconnection control and independent real and reactive power flow control, and compared with its counterpart, VSC based HVDC, it needs less converter rating. This will greatly help with reducing transmission congestion and increasing dynamic rating of the transmission assets.
4. Application of transformer-less UPFC to in congested grid and make parallel connection between two different feeders possible. The transformer-less UPFC can increase the power flow when the phase between sending and receiving end is limited and the benefits have been discussed with underground cable power transmission. Compared with the other existing technology, transformer-less UPFC can provide more routine to the power flow at the minimum cost and smallest line construction.
5. An innovative T-shape UPFC with even reduced converter rating is presented. The proposed T-shape transformer-less UPFC has more control freedom and smaller converter rating, thus makes it also attractive for system integration of transformer-less UPFC.

7.2 Recommendations for Future Work

1. Experimental verification for virtual inertia control of CMI based STATCOM. System level simulation has shown that CMI based STATCOM can be used for frequency regulation and it can provide competitive inertia response to the system. It is expected that STATCOM with the proposed VIC control can be tested in experimental setup for verification;
2. Experimental verification of T-shape transformer-less UPFC. It has been analyzed in the dissertation that T-shape transformer-less UPFC can reduce total converter rating of UPFC and provide more control freedom. Also, its installation will be more flexible along the transmission line. It is expected that field test of transformer-less T-shape UPFC can be carried out.
3. Operation of the transformer-less UPFC under power system abnormal conditions, such as sags, swells, power system oscillations, faults and etc. Since the potential application for the proposed transformer-less UPFC is for transmission level application, the system is usually three-phase balanced and pollution free. It will be an interesting topic to investigate control strategy of transformer-less UPFC against unbalanced system condition and carry out experimental verification.
4. Topology and control method for totally transformer-less UPQC for distribution level application. How to reduce converter rating, cost and size to compensate voltage dips without any phase jump. Two main factors influence converter rating for UPQC application is voltage sag depth and load power factor. It will also be an interesting topic to investigate total transformer-less, less energy storage requirements for distribution system application.

BIBLIOGRAPHY

BIBLIOGRAPHY

[1] Rodriguez, J., J.S. Lai, and F.Z. Peng, "Multilevel inverters: a survey of topologies, controls, and applications." *IEEE Transactions on Industrial Electronics*, 2002. **49**(4): p. 724-738.

[2] Rodriguez, J., et al., "Multilevel Voltage-Source-Converter Topologies for Industrial Medium-Voltage Drives." *IEEE Transactions on Industrial Electronics*, 2007. **54**(6): p. 2930-2945.

[3] Lai, J.S. and F.Z. Peng, "Multilevel converters-a new breed of power converters." *IEEE Transactions on Industry Applications*, 1996. **32**(3): p. 509-517.

[4] Teodorescu, R., et al., "Multilevel inverter by cascading industrial VSI." *IEEE Transactions on Industrial Electronics*, 2002. **49**(4): p. 832-838.

[5] Malinowski, M., et al., "A Survey on Cascaded Multilevel Inverters." *IEEE Transactions on Industrial Electronics*, 2010. **57**(7): p. 2197-2206.

[6] Peng, F.Z., W. Qian, and D. Cao. "Recent advances in multilevel converter/inverter topologies and applications." in *2010 International Power Electronics Conference (IPEC)*. 2010.

[7] Tolbert, L.M., F.Z. Peng, and T.G. Habetler, "Multilevel converters for large electric drives." *IEEE Transactions on Industry Applications*, 1999. **35**(1): p. 36-44.

[8] Mutale, J. and G. Strbac, "Transmission network reinforcement versus FACTS: an economic assessment." *IEEE Transactions on Power Systems*, 2000. **15**(3): p. 961-967.

[9] Paserba, J.J. "How FACTS controllers benefit AC transmission systems." in *2003 IEEE PES Transmission and Distribution Conference and Exposition*. 2003.

[10] Xiao, Y., et al., "Available transfer capability enhancement using FACTS devices." *IEEE Transactions on Power Systems*, 2003. **18**(1): p. 305-312.

[11] Hingorani, N.G. and L. Gyugyi, *Understanding facts*. 2000: IEEE press.

[12] Ghosh, A. and G.F. Ledwich, *Power quality enhancement using custom power devices*. 2002: Kluwer academic publishers.

[13] Nabae, A., I. Takahashi, and H. Akagi, "A New Neutral-Point-Clamped PWM Inverter." *IEEE Transactions on Industry Applications*, 1981. **IA-17**(5): p. 518-523.

[14] Peng, F.Z., et al., "A multilevel voltage-source inverter with separate DC sources for static VAr generation." *IEEE Transactions on Industry Applications*, 1996. **32**(5): p. 1130-1138.

[15] Gultekin, B., et al., "Design and Implementation of a 154-kV +-50-Mvar Transmission STATCOM Based on 21-Level Cascaded Multilevel Converter." *IEEE Transactions on Industry Applications*, 2012. **48**(3): p. 1030-1045.

[16] Wang, J. and F.Z. Peng, "Unified power flow controller using the cascade multilevel inverter." *IEEE Transactions on Power Electronics*, 2004. **19**(4): p. 1077-1084.

[17] Peng, F.Z. and J.S. Lai, "Dynamic performance and control of a static VAr generator using cascade multilevel inverters." *IEEE Transactions on Industry Applications*, 1997. **33**(3): p. 748-755.

[18] Liu, Z., et al., "A Novel DC Capacitor Voltage Balance Control Method for Cascade Multilevel STATCOM." *IEEE Transactions on Power Electronics*, 2012. **27**(1): p. 14-27.

[19] Akagi, H., S. Inoue, and T. Yoshii, "Control and Performance of a Transformerless Cascade PWM STATCOM With Star Configuration." *IEEE Transactions on Industry Applications*, 2007. **43**(4): p. 1041-1049.

[20] McGrath, B.P. and D.G. Holmes, "Multicarrier PWM strategies for multilevel inverters." *IEEE Transactions on Industrial Electronics*, 2002. **49**(4): p. 858-867.

[21] Naderi, R. and A. Rahmati, "Phase-Shifted Carrier PWM Technique for General Cascaded Inverters." *IEEE Transactions on Power Electronics*, 2008. **23**(3): p. 1257-1269.

[22] Yao, W.X., H.B. Hu, and Z.Y. Lu, "Comparisons of Space-Vector Modulation and Carrier-Based Modulation of Multilevel Inverter." *IEEE Transactions on Power Electronics*, 2008. **23**(1): p. 45-51.

[23] Rodriguez, J., et al., "A vector control technique for medium-voltage multilevel inverters." *IEEE Transactions on Industrial Electronics*, 2002. **49**(4): p. 882-888.

[24] Gupta, A.K. and A.M. Khambadkone, "A General Space Vector PWM Algorithm for Multilevel Inverters, Including Operation in Overmodulation Range." *IEEE Transactions on Power Electronics*, 2007. **22**(2): p. 517-526.

[25] Wei, S.M., et al. "A general space vector PWM control algorithm for multilevel inverters." in *Eighteenth Annual IEEE Applied Power Electronics Conference and Exposition*. 2003.

[26] Dahidah, M.S.A. and V.G. Agelidis, "Selective Harmonic Elimination PWM Control for Cascaded Multilevel Voltage Source Converters: A Generalized Formula." *IEEE Transactions on Power Electronics*, 2008. **23**(4): p. 1620-1630.

[27] Agelidis, V.G., A.I. Balouktsis, and M.S.A. Dahidah, "A Five-Level Symmetrically Defined Selective Harmonic Elimination PWM Strategy: Analysis and Experimental Validation." *IEEE Transactions on Power Electronics*, 2008. **23**(1): p. 19-26.

[28] Li, L., et al., "Multilevel selective harmonic elimination PWM technique in series-connected voltage inverters." *IEEE Transactions on Industry Applications*, 2000. **36**(1): p. 160-170.

[29] Wu, B., *High-power converters and AC drives*. 2006: John Wiley & Sons.

[30] Patel, H.S. and R.G. Hoft, "Generalized Techniques of Harmonic Elimination and Voltage Control in Thyristor Inverters: Part I--Harmonic Elimination." *IEEE Transactions on Industry Applications*, 1973. **IA-9**(3): p. 310-317.

[31] Peng, F.Z., J.W. McKeever, and D.J. Adams, "A power line conditioner using cascade multilevel inverters for distribution systems." *IEEE Transactions on Industry Applications*, 1998. **34**(6): p. 1293-1298.

[32] Gultekin, B. and M. Ermis, "Cascaded Multilevel Converter-Based Transmission STATCOM: System Design Methodology and Development of a 12 kV/12 MVAr Power Stage." *IEEE Transactions on Power Electronics*, 2013. **28**(11): p. 4930-4950.

[33] Atalik, T., et al., "Multi-DSP and -FPGA-Based Fully Digital Control System for Cascaded Multilevel Converters Used in FACTS Applications." *IEEE Transactions on Industrial Informatics*, 2012. **8**(3): p. 511-527.

[34] Joos, G., X.G. Huang, and B.T. Ooi, "Direct-coupled multilevel cascaded series VAr compensators." *IEEE Transactions on Industry Applications*, 1998. **34**(5): p. 1156-1163.

[35] Peng, F.Z., et al. "Transformer-less unified power flow controller using the cascade multilevel inverter." in *2014 International Power Electronics Conference (IPEC-Hiroshima 2014 - ECCE-ASIA)*. 2014.

[36] NERC, *NERC Frequency Response Initiative*. 2010.

[37] Muljadi, E., et al. "Understanding inertial and frequency response of wind power plants." in *2012 IEEE Power Electronics and Machines in Wind Applications (PEMWA)*. 2012.

[38] Kundur, P., N.J. Balu, and M.G. Lauby, *Power system stability and control*. Vol. 7. 1994: McGraw-hill New York.

[39] Corporation, W.E., *Electrical transmission and distribution reference book*. 1942: Westinghouse electric & manufacturing Company.

[40] Teleke, S., et al., "Dynamic Performance Comparison of Synchronous Condenser and SVC." *IEEE Transactions on Power Delivery*, 2008. **23**(3): p. 1606-1612.

[41] Knudsen, H. and J.N. Nielsen, "Introduction to the modeling of wind turbines." *Wind Power in Power Systems*, 2005: p. 525-585.

[42] Holdsworth, L., J.B. Ekanayake, and N. Jenkins, "Power system frequency response from fixed speed and doubly fed induction generator ‐ based wind turbines." *Wind Energy*, 2004. **7**(1): p. 21-35.

[43] Morren, J., et al., "Wind turbines emulating inertia and supporting primary frequency control." *IEEE Transactions on Power Systems*, 2006. **21**(1): p. 433-434.

[44] Attya, A.B.T. and T. Hartkopf, "Control and quantification of kinetic energy released by wind farms during power system frequency drops." *IET Renewable Power Generation*, 2013. **7**(3): p. 210-224.

[45] Liu, Y., et al. "Comparison of synchronous condenser and STATCOM for inertial response support." in *2014 IEEE Energy Conversion Congress and Exposition (ECCE)*. 2014.

[46] Sirisukprasert, S., A.Q. Huang, and J.S. Lai. "Modeling, analysis and control of cascaded-multilevel converter-based STATCOM." in *IEEE Power Engineering Society General Meeting*. 2003.

[47] Zhu, J.B., et al., "Inertia Emulation Control Strategy for VSC-HVDC Transmission Systems." *IEEE Transactions on Power Systems*, 2013. **28**(2): p. 1277-1287.

[48] Gyugyi, L., et al., "The unified power flow controller: a new approach to power transmission control." *IEEE Transactions on Power Delivery*, 1995. **10**(2): p. 1085-1097.

[49] Rajabi-Ghahnavieh, A., et al., "UPFC for Enhancing Power System Reliability." *IEEE Transactions on Power Delivery*, 2010. **25**(4): p. 2881-2890.

[50] Fujita, H., Y. Watanabe, and H. Akagi, "Control and analysis of a unified power flow controller." *IEEE Transactions on Power Electronics*, 1999. **14**(6): p. 1021-1027.

[51] Sayed, M.A. and T. Takeshita, "Line Loss Minimization in Isolated Substations and Multiple Loop Distribution Systems Using the UPFC." *IEEE Transactions on Power Electronics*, 2014. **29**(11): p. 5813-5822.

[52] Fujita, H., Y. Watanabe, and H. Akagi, "Transient analysis of a unified power flow controller and its application to design of the DC-link capacitor." *IEEE Transactions on Power Electronics*, 2001. **16**(5): p. 735-740.

[53] Fujita, H., H. Akagi, and Y. Watanabe, "Dynamic control and performance of a unified power flow controller for stabilizing an AC transmission system." *IEEE Transactions on Power Electronics*, 2006. **21**(4): p. 1013-1020.

[54] Liu, L.M., et al., "Power-Flow Control Performance Analysis of a Unified Power-Flow Controller in a Novel Control Scheme." *IEEE Transactions on Power Delivery*, 2007. **22**(3): p. 1613-1619.

[55] Kannan, S., S. Jayaram, and M.M.A. Salama, "Real and reactive power coordination for a unified power flow controller." *IEEE Transactions on Power Systems*, 2004. **19**(3): p. 1454-1461.

[56] Bebic, J.Z., P.W. Lehn, and M.R. Iravani, "P-δ characteristics for the unified power flow controller-analysis inclusive of equipment ratings and line limits." *IEEE Transactions on Power Delivery*, 2003. **18**(3): p. 1066-1072.

[57] Schauder, C.D., et al., "Operation of the unified power flow controller (UPFC) under practical constraints." *IEEE Transactions on Power Delivery*, 1998. **13**(2): p. 630-639.

[58] Kim, S.Y., et al. "The operation experience of KEPCO UPFC." in *Proceedings of the Eighth International Conference on Electrical Machines and Systems (ICEMS)* 2005.

[59] Schauder, C., et al., "AEP UPFC project: installation, commissioning and operation of the ±160 MVA STATCOM (phase I)." *IEEE Transactions on Power Delivery*, 1998. **13**(4): p. 1530-1535.

[60] Sano, K. and M. Takasaki, "A Transformerless D-STATCOM Based on a Multivoltage Cascade Converter Requiring No DC Sources." *IEEE Transactions on Power Electronics*, 2012. **27**(6): p. 2783-2795.

[61] Renz, B.A., et al., "AEP unified power flow controller performance." *IEEE Transactions on Power Delivery*, 1999. **14**(4): p. 1374-1381.

[62] Monteiro, J., et al., "Matrix Converter-Based Unified Power-Flow Controllers: Advanced Direct Power Control Method." *IEEE Transactions on Power Delivery*, 2011. **26**(1): p. 420-430.

[63] Monteiro, J., et al., "Linear and Sliding-Mode Control Design for Matrix Converter-Based Unified Power Flow Controllers." *IEEE Transactions on Power Electronics*, 2014. **29**(7): p. 3357-3367.

[64] Dasgupta, A., P. Tripathy, and P.S. Sensarma. "Matrix converter as UPFC for transmission line compensation." in *7th Internatonal Conference on Power Electronics (ICPE)*. 2007.

[65] Yuan, Z.H., et al., "A FACTS Device: Distributed Power-Flow Controller (DPFC)." *IEEE Transactions on Power Electronics*, 2010. **25**(10): p. 2564-2572.

[66] Peng, F.Z. and J. Wang. "A universal STATCOM with delta-connected cascade multilevel inverter." in *2004 IEEE 35th Annual Power Electronics Specialists Conference*. 2004.

[67] Gultekin, B., et al., "Design and Implementation of a 154-kV /50-Mvar Transmission STATCOM Based on 21-Level Cascaded Multilevel Converter." *IEEE Transactions on Industry Applications*, 2012. **48**(3): p. 1030-1045.

[68] Hanson, D.J., et al. "A STATCOM-based relocatable SVC project in the UK for National Grid." in *IEEE Power Engineering Society Winter Meeting*. 2002.

[69] Peng, F.Z., J.W. McKeever, and D.J. Adams. "Cascade multilevel inverters for utility applications." in *23rd International Conference on Industrial Electronics, Control and Instrumentation*. 1997.

[70] Maharjan, L., S. Inoue, and H. Akagi, "A Transformerless Energy Storage System Based on a Cascade Multilevel PWM Converter With Star Configuration." *IEEE Transactions on Industry Applications*, 2008. **44**(5): p. 1621-1630.

[71] Loh, P.C., D.G. Holmes, and T.A. Lipo, "Implementation and control of distributed PWM cascaded multilevel inverters with minimal harmonic distortion and common-mode voltage." *IEEE Transactions on Power Electronics*, 2005. **20**(1): p. 90-99.

[72] Park, Y.M., J.Y. Yoo, and S.B. Lee, "Practical Implementation of PWM Synchronization and Phase-Shift Method for Cascaded H-Bridge Multilevel Inverters Based on a Standard Serial Communication Protocol." *IEEE Transactions on Industry Applications*, 2008. **44**(2): p. 634-643.

[73] Xu, R., et al., "A Novel Control Method for Transformerless H-Bridge Cascaded STATCOM With Star Configuration." *IEEE Transactions on Power Electronics*, 2015. **30**(3): p. 1189-1202.

[74] Kaymaz, P., J. Valenzuela, and C.S. Park, "Transmission Congestion and Competition on Power Generation Expansion." *IEEE Transactions on Power Systems*, 2007. **22**(1): p. 156-163.

[75] M. Marz, et al. "Mackinac HVDC converter automatic runback utilizing locally measured quantities." in *CIGRÉ Canada Conference*. 2014. Toronto.

[76] Brumshagen, H. and J. Schwarz, "The European power systems on the threshold of a new East-West co-operation." *IEEE Transactions on Energy Conversion*, 1996. **11**(2): p. 462-474.

[77] Zhang, L.D., L. Harnefors, and H.P. Nee, "Interconnection of Two Very Weak AC Systems by VSC-HVDC Links Using Power-Synchronization Control." *IEEE Transactions on Power Systems*, 2011. **26**(1): p. 344-355.

[78] Abe, R., H. Taoka, and D. McQuilkin, "Digital Grid: Communicative Electrical Grids of the Future." *IEEE Transactions on Smart Grid*, 2011. **2**(2): p. 399-410.

[79] Johansson, N., L. Angquist, and H.P. Nee, "Preliminary Design of Power Controller Devices Using the Power-Flow Control and the Ideal Phase-Shifter Methods." *IEEE Transactions on Power Delivery*, 2012. **27**(3): p. 1268-1275.

[80] Vanajaa, V.R. and N.A. Vasanthi. "Conceptual study and operational overview on Variable Frequency Transformer used for grid interconnections." in *2012 Third International Conference on Computing Communication & Networking Technologies (ICCCNT)*. 2012.

[81] Verboomen, J., et al., "Analytical Approach to Grid Operation With Phase Shifting Transformers." *IEEE Transactions on Power Systems*, 2008. **23**(1): p. 41-46.

[82] Van Hertem, D., J. Rimez, and R. Belmans, "Power Flow Controlling Devices as a Smart and Independent Grid Investment for Flexible Grid Operations: Belgian Case Study." *IEEE Transactions on Smart Grid*, 2013. **4**(3): p. 1656-1664.

[83] Merkhouf, A., P. Doyon, and S. Upadhyay, "Variable Frequency Transformer-Concept and Electromagnetic Design Evaluation." *IEEE Transactions on Energy Conversion*, 2008. **23**(4): p. 989-996.

[84] Mitra, P., L.D. Zhang, and L. Harnefors, "Offshore Wind Integration to a Weak Grid by VSC-HVDC Links Using Power-Synchronization Control: A Case Study." *IEEE Transactions on Power Delivery*, 2014. **29**(1): p. 453-461.

[85] Zhang, L.D., L. Harnefors, and H.P. Nee, "Power-Synchronization Control of Grid-Connected Voltage-Source Converters." *IEEE Transactions on Power Systems*, 2010. **25**(2): p. 809-820.

[86] Zhang, L.D., H.P. Nee, and L. Harnefors, "Analysis of Stability Limitations of a VSC-HVDC Link Using Power-Synchronization Control." *IEEE Transactions on Power Systems*, 2011. **26**(3): p. 1326-1337.

[87] Samet, H., T. Ghanbari, and J. Ghaisari, "Maximum Performance of Electric Arc Furnace by Optimal Setting of the Series Reactor and Transformer Taps Using a Nonlinear Model." *IEEE Transactions on Power Delivery*, 2015. **PP**(99): p. 1-9.

[88] Sen, K.K. and M.L. Sen, "Introducing the family of "Sen" transformers: a set of power flow controlling transformers." *IEEE Transactions on Power Delivery*, 2003. **18**(1): p. 149-157.

[89] Mihalic, R. and P. Zunko, "Phase-shifting transformer with fixed phase between terminal voltage and voltage boost: tool for transient stability margin enhancement." *IEE Proceedings-Generation, Transmission and Distribution*, 1995. **142**(3): p. 257-262.

[90] Flourentzou, N., V.G. Agelidis, and G.D. Demetriades, "VSC-Based HVDC Power Transmission Systems: An Overview." *IEEE Transactions on Power Electronics*, 2009. **24**(3): p. 592-602.

[91] Liu, Y. and Z. Chen, "A Flexible Power Control Method of VSC-HVDC Link for the Enhancement of Effective Short-Circuit Ratio in a Hybrid Multi-Infeed HVDC System." *IEEE Transactions on Power Systems*, 2013. **28**(2): p. 1568-1581.

[92] Gunasekaran, D., S.T. Yang, and F.Z. Peng. "Fractionally Rated Transformer-less Unified Power Flow Controllers for Interconnecting Synchronous AC Grids." in *ECCE*. 2014.

[93] Kouro, S., et al., "High-Performance Torque and Flux Control for Multilevel Inverter Fed Induction Motors." *IEEE Transactions on Power Electronics*, 2007. **22**(6): p. 2116-2123.

[94] Orawski, G., "Overhead lines-the state of the art." *Power engineering journal*, 1993. **7**(5): p. 221-231.

[95] Del Rosso, A.D. and S.W. Eckroad, "Energy storage for relief of transmission congestion." *IEEE Transactions on Smart Grid*, 2014. **5**(2): p. 1138-1146.

[96] Seppänen, J.M., P.O. Tammi, and L.C. Haarla, "Underground ground wires for transmission lines: electrical behavior and feasibility." *IEEE Transactions on Power Delivery*, 2013. **28**(1): p. 206-215.

[97] Morioka, Y., et al., "Implementation of unified power flow controller and verification for transmission capability improvement." *IEEE Transactions on Power Systems*, 1999. **14**(2): p. 575-581.

[98] Edris, A., "FACTS technology development: an update." *IEEE Power Engineering Review*, 2000. **20**(3): p. 4-9.

[99] Divan, D.M., et al., "A Distributed Static Series Compensator System for Realizing Active Power Flow Control on Existing Power Lines." *IEEE Transactions on Power Delivery*, 2007. **22**(1): p. 642-649.

[100] Yousefpoor, N., et al., "Modular Transformer Converter-Based Convertible Static Transmission Controller for Transmission Grid Management." *IEEE Transactions on Power Electronics*, 2014. **29**(12): p. 6293-6306.

[101] Asplund, G. "Application of HVDC Light to power system enhancement." in *IEEE Power Engineering Society Winter Meeting*. 2000. IEEE.

[102] Gemmell, B., et al. "Prospects of multilevel VSC technologies for power transmission." in *IEEE-PES Transmission and Distribution Conference and Exposition*. 2008. IEEE.

[103] Buijs, P., et al., "Transmission investment problems in Europe: Going beyond standard solutions." *Energy Policy*, 2011. **39**(3): p. 1794-1801.

[104] *Evaluation of Underground Electric Transmission Lines in Virginia*, 2006, http://jlarc.virginia.gov/reports/rpt343.pdf.

[105] Reddy, C.C., "Theoretical maximum limits on power-handling capacity of HVDC cables." *IEEE Transactions on Power Delivery*, 2009. **24**(3): p. 980-987.

[106] Terciyanli, A., et al., "Power quality solutions for light rail public transportation systems fed by medium-voltage underground cables." *IEEE Transactions on Industry Applications*, 2012. **48**(3): p. 1017-1029.

[107] Zhang, S., et al., "Resonance issues and damping techniques for grid-connected inverters with long transmission cable." *IEEE Transactions on Power Electronics*, 2014. **29**(1): p. 110-120.

[108] Gunasekaran, D., S.T. Yang, and F.Z. Peng. "Fractionally rated transformer-less unified power flow controllers for interconnecting synchronous AC grids." in *Applied Power Electronics Conference and Exposition (APEC), 2015 IEEE*. 2015.